Fatigue Assessment of a Wedge Connection for Offshore Wind Turbine Structures

by

Eleni Bakaloni

to obtain the degree of Master of Science
at the Delft University of Technology,
to be defended publicly on Thursday December 13, 2018.

Student number:	4521722	
Thesis committee:	Prof.dr.M.V.Veljkovic,	TU Delft-Chairman
	Dr.A. Jarquin Laguna,	TU Delft
	Dr.Haohui Xin,	TU Delft
	Ir.J.S Winkes,	Fistuca BV
	Ir.K. Creusen,	Fistuca BV

This thesis is confidential and cannot be made public until 13/12/2023

An electronic version of this thesis is available at `http://repository.tudelft.nl/`.

Abstract

Wind turbines constitute a sustainable and effective solution for the production of energy using wind power. Offshore wind turbines are becoming of special interest. However, their design poses great challenges, since an offshore structure is subjected to combined wind and wave dynamic loading that is characteristic of the installation site and play an important role on the fatigue failure of the wind turbine structure.

One part of specific interest for the fatigue assessment of a wind turbine is the way that the transition piece is connected to monopile. Since now, grouted and bolted connections are commonly used, but their many drawbacks regarding their performance inspired Fistuca BV to invent a new type of connection, the wedge connection, in order to increase the fatigue life of the wind turbine structures and decrease simultaneously their construction and installation cost. More specifically, a basic flange with inclined planes is attached on the top of the monopile and a more complex one (fork-shaped flange) is fitted to the bottom of the transition piece. Inclined dowels are used to connect the two flanges and secure the structure. The final positioning of the dowels is achieved by applying external pressure on the back side of them, which is converted to a vertical reaction force between the two flanges through the inclined planes, acting as preload.

The work that will be presented here deals with the fatigue assessment of the wedge connection, and how the presence of the preloading force may affect the fatigue life of it.

A reference wind turbine and a reference location have been selected first, in order to calculate all the fatigue loads resulted on the structure due to wind and wave at the level where the wedge connection has been selected to be located (+4m above the MSL). The concept of damage equivalent loads has been applied. Damage loads due to waves have been calculated in the frequency domain, while damage loads due to wind have been handled in the time domain due to strongest non-linearities in the rotor aerodynamics. The process of damage loads' calculation was carried out using MATLAB.

Once the loads have been calculated, the 3D CAD design software of SOLIDWORKS is used to design all the components of the wedge connection and assemble them to their final position. To facilitate the design process and reduce the computational time, the flange connection is reduced to a single wedge segment, on which the highest stresses are developed. Two load cases are examined for each one of the above resulted damage loads: one with preload and another one without preload. For the purpose of this thesis, xx MPa external pressure has been applied for the final positioning of dowels in case of preload. ANSYS Workbench has been used for the finite element analysis. Nominal stresses are calculated and based on selected S-N curves for both DNV-GL codes and Eurocode 3 and by making use of the Miner's rule, the damage and the fatigue life of the connection is calculated. The selection of the appropriate S-N curve for each load case and for each component of the connection, has been based on results from test specimens.

A parametric study has been carried out as well, in order to check several parameters that may affect both the accuracy of the finite element analysis and the stress development on the connection, and as a result the damage and the fatigue life of it.

Acknowledgements

I would like to express my gratitude to all the individuals that have helped me throughout the compilation of this thesis.

First, I would like to thank my supervisors from the company, Jasper Winkes and Koen Creusen, for proposing a such interesting and challenging topic and their support and guidance during this thesis project, and of course the entire team of FISTUCA.

Also, I would like to thank my university supervisors, Prof.Dr.M.Veljkovic, Dr.A.Laguna and Dr.H.Xin for their critical feedback and guidance along the way.

Finally, the unconditional support of my family and my friends, both from Greece and Netherlands, was crucial throughout the conduction of this thesis, from beginning to end, and I would like to express my sincere gratitude for everything they offered.

Eleni Bakaloni
Delft, December 2018

Contents

List of Figures ix

List of Tables xiii

Nomenclature xv

1 Introduction 1
- 1.1 Background . . . 1
- 1.2 The concept of Wedge Connection . . . 2
- 1.3 Research Objective . . . 5
- 1.4 Research Methodology. . . . 5
- 1.5 Thesis Outline . . . 6

2 Fatigue-Literature Study 7
- 2.1 Fatigue Definition . . . 7
- 2.2 Main parameters influencing the fatigue life. . . . 7
- 2.3 S-N Curve Method . . . 8
- 2.4 Fatigue Strength . . . 8
- 2.5 Cumulative Fatigue Damage Rule. . . . 9
- 2.6 Cyclic Counting Procedure for Random Stresses. . . . 10
  - 2.6.1 Rainflow Cycle Counting . . . 11

3 Environmental Loading 13
- 3.1 Reference Turbine . . . 13
- 3.2 Reference Location. . . . 14
- 3.3 Mathematical Model of the Wind Turbine . . . 17
  - 3.3.1 Soil parameters and p-y curves . . . 18
  - 3.3.2 Modal Analysis . . . 19
- 3.4 Wave Spectral Density . . . 21
- 3.5 Morison's Equation . . . 23
- 3.6 Wind Speed & Turbulence . . . 25
- 3.7 Wind Spectral Density . . . 25
- 3.8 Thrust Force . . . 27

4 Damage Equivalent Loads 29
- 4.1 Fatigue Assessment . . . 29
- 4.2 Method Summary. . . . 30
- 4.3 Time domain versus frequency domain approach . . . 30
- 4.4 Equivalent Loads . . . 31
- 4.5 Hydrodynamic Loading. . . . 31
- 4.6 Frequency domain analysis - Wave DEL . . . 31
- 4.7 Time domain analysis - Wind DEL. . . . 34
  - 4.7.1 Equivalent Stresses & Rainflow Counting Method . . . 35
- 4.8 Results of Damage Loads . . . 37

5 Modeling of Wedge Connection in ANSYS 39
- 5.1 Material Properties . . . 40
- 5.2 Meshing. . . . 40
- 5.3 Contact Elements. . . . 41
- 5.4 Boundary Conditions . . . 42
- 5.5 Loading . . . 43

6 Finite Element Analysis & Fatigue Assessment **45**
6.1 Load Sharing . . . 45
  6.1.1 Non-preloading case . . . 45
  6.1.2 Preloading case . . . 45
6.2 Loads developed on MP flange . . . 49
6.3 Determination of S-N curves . . . 49
6.4 Test results & Selection of S-N curve . . . 50
6.5 Fatigue assessment of the wedge connection . . . 51
  6.5.1 Fatigue assessment of the two flanges . . . 51
  6.5.2 Fatigue assessment of the dowel . . . 55
  6.5.3 Fatigue assessment of bushings . . . 57

7 Parametric Study **59**
7.1 Mesh size . . . 59
7.2 Friction coefficient . . . 60
  7.2.1 Friction coefficient between MP flange and wedges . . . 60
  7.2.2 Friction coefficient of bushings . . . 62
7.3 Stiffness of bushings . . . 62

8 Conclusions & Recommendations **65**
8.1 Conclusions . . . 65
8.2 Recommendations . . . 66

A Finite Differences Scheme **67**

B Wind Time Series Generation and Thrust Force **71**

C Force Applied on Dowel due to Hydraulic Pressure **73**

D Parametric study of preload **75**

E Stress development in critical parts **77**

F Wedge connection geometry **79**

Bibliography **81**

List of Figures

1.1 New concept of wedge connection. 2
1.2 Left: grouted connection [8], Right: bolted connection [34]. 3
1.3 Positioning of dowels by hydraulic actuators 3
1.4 Positioning of dowels manually 4
1.5 Load path of the wedge connection (left: reaction forces on dowel, right: transferred reaction forces on MP flange) 4
1.6 Gap growing for different levels of applied pressure on the dowel until the ULS load. 5
1.7 Gap opening for different levels of applied pressure on the dowel for the ULS load. 5
1.8 Development of contact pressure between MP-TP flanges. 5

2.1 Quantitative dependence between number of cycles which defines strength of a structural detail in fatigue [29]. 8
2.2 S-N curve Definition [29]. 9
2.3 Constant amplitude fatigue limit [29]. 9
2.4 Damage accumulation scheme [29]. 10
2.5 Constant amplitude stress history [16]. 11
2.6 Variable amplitude stress history [16]. 11
2.7 An example stress time history and the equivalent linear model[16]. 12
2.8 An example pagoda roof and corresponding rainflow cycle counting patterns. a The pagoda roof model of stress history b The rainflow patterns [16]. 12

3.1 North Sea [3]. 14
3.2 North Sea State Information 15
3.3 Left: Weibull wind speed distribution, Right: Weibull cumulative wind speed distribution. 16
3.4 Beam Model of the wind turbine. 17
3.5 Beam Model discretization. 17
3.6 Soil modeling by making use of spring elements. 18
3.7 Resulting p-y curve at 23m below the sea bed. 19
3.8 Three first mode shapes of beam model. 21
3.9 JONSWAP Spectrum for all Sea States. 22
3.10 Time series realization of water elevation derived from wave spectrum. 23
3.11 Morison Force for Sea State 8 with C_D=0.8. 24
3.12 MacCamy-Fuchs diffraction correction of the inertia coefficient C_M. 25
3.13 Kaimal Spectrum for mean wind speed equal to 11.06m/sec. 26
3.14 Wind Time Series for mean wind speed equal to 11.06m/sec. 26

4.1 Load sources for a monopile-based offshore wind turbine [40] 29
4.2 Procedure for damage loads calculation 30
4.3 Distribution Function for H_s=4m 32
4.4 Lay-out of Mechanical Transfer function 33
4.5 Transfer function at the level of wedge connection 33
4.6 Wind and corresponding thrust force time series for mean wind speed equal to 11.06 m/sec (SS 2) 35
4.7 Wind and corresponding thrust force time series for mean wind speed equal to 25.09 m/sec (SS 16) 35
4.8 Equivalent stress time series for mean wind speed equal to 6.30m/sec (SS 1) 36
4.9 Rainflow count histogram of equivalent stress time series (SS 1). 36

5.1 Wedge Connection model designed in SOLIDWORKS 39
5.2 Solid187 element on the left and SOLID186 element on the right [31]. 40
5.3 Meshed parts of wedge connection. 41
5.4 Load steps. 43

6.1 Load sharing (distribution) on wedge connection. 46
6.2 Equivalent spring system. 46
6.3 Model A: Stiffness calculation of MP flange. 47
6.4 Model B: Stiffness calculation of TP flange, dowel and bushings. 47
6.5 Left: Total deformation of Model A (MP flange), Right: Total deformation of Model B (TP flange, dowel and bushings). 47
6.6 Force sharing on the wedge connection 48
6.7 Preload MP flange (left) subjected to tensile load (right). 49
6.8 Tested segment of wedge connection under fatigue loading. 50
6.9 S-N curves. 51
6.10 S-N curves used for the flanges (wind damage load). 51
6.11 Selected detail category for the flanges [1]. 52
6.12 Damage for flanges. 53
6.13 Maximum principal stress developed on MP flange for the maximum wind damage load in case without preload. 53
6.14 Maximum principal stress developed on MP flange at the end of the preloading step (30 MPa applied pressure). 53
6.15 Maximum principal stress developed on MP flange for the maximum wind damage load in case with preload. 53
6.16 Maximum principal stress developed on TP flange for the maximum wind damage load in case without preload. 53
6.17 Maximum principal stress developed on TP flange at the end of the preloading step (30 MPa applied pressure). 53
6.18 Maximum principal stress developed on TP flange for the maximum wind damage load in case with preload. 53
6.19 S-N curves used for the flanges (wave damage load). 54
6.20 Stress development on dowel in case of preload until the ULS load. 55
6.21 Selected detail category for dowels [1]. 55
6.22 S-N curve used for dowels. 55
6.23 Maximum principal stress developed on dowel for the maximum wind damage load in case without preload. 56
6.24 Maximum principal stress developed on dowel at the end of the preloading step (30 MPa applied pressure). 56
6.25 Maximum principal stress developed on dowel for the maximum wind damage load in case with preload. 56
6.26 Maximum principal stress development at the bottom side of dowel. 57
6.27 Estimated model parameters [19]. 57
6.28 S-N curve used for the bushings in case without preload. 58
6.29 S-N curve used for the bushings in case with preload. 58
6.30 Minimum principal stress distribution on bushings in case where no preload takes place. 58
6.31 Minimum principal stress distribution on bushings at the end of preloading step. 58
6.32 Minimum principal stress distribution on bushings in case where preload takes place. 58

7.1 Total damage of each component for coarse and fine mesh. 59
7.2 Percentage of damage change for each component for coarse and fine mesh. . . 60
7.3 Maximum principal stresses for MP flange for coarse (left) and fine (right) mesh. 60
7.4 Maximum principal stresses for TP flange for coarse (left) and fine (right) mesh. 60
7.5 Maximum principal stresses for dowel for coarse (left) and fine (right) mesh. . . 60

7.6 Maximum principal stress of each component for different values of friction coefficient between MP flange and dowel. 61
7.7 Percentage of stress change for each component for different values of friction coefficient between MP flange and dowel. 61
7.8 Contact pressure between MP and TP flanges for different values of friction coefficient between MP flange and dowels. 61
7.9 Dowel: Free body diagram. 62
7.10 Maximum principal stresses developed on each component for different values of friction coefficient of bushings. 62
7.11 Percentage of stress change for each component for different values of friction coefficient of bushings. 63
7.12 Contact pressure between MP and TP flanges for different values of friction coefficient of bushings. 63
7.13 Maximum principal stresses developed on each component for increasing bushings' stiffness. 63
7.14 Percentage of stress change of each component for increasing bushings' stiffness. 63

8.1 Total Damage of the wedge connection (wind loading). 66

A.1 Discretization of a beam [18] 67

C.1 Geometry of the dowel. 73

D.1 Effect of friction coefficient of bushings' surface in the preloading ratio. 75
D.2 Effect of friction coefficient between MP and dowel in the preloading ratio. . . . 76
D.3 Effect of the angle of the inclined planes in the preloading ratio. 76

E.1 Maximum principal stress development around the hole of the MP flange . . . 77
E.2 Maximum principal stress development around the inner part of the hole of the TP flange 77

F.1 Detail geometry 79
F.2 Detail geometry 79

List of Tables

3.1 Relevant reference turbine parameters 13
3.2 North Sea Data: wave information. 14
3.3 North Sea Data: wind information. 15
3.4 Weibull Probability of occurrence for each mean wind speed. 16
3.5 Three first natural frequencies of beam model. 21

4.1 Damage Equivalent Moment for wave loading. 37
4.2 Damage Equivalent Moment for wind loading. 38

6.1 Data for damage calculation due to wind loading. 52
6.2 Allowable number of cycles and resulting damage foe both cases of wind loading for the flanges. 52
6.3 Allowable number of cycles and resulting damage foe both cases of wave loading for the flanges. 54
6.4 Data for damage calculation due to wind loading. 55
6.5 Allowable number of cycles and resulting damage foe both cases of wind loading for the flanges. 58

8.1 Damage of the wedge connection. 65

Nomenclature

Acronyms

API	American Petroleum Institute
DEL	Damage Equivalent Load
DEM	Damage Equivalent Moment
FBD	Free Body Diagram
FEA	Finite Element Analysis
FEM	Finite Element Modeling
FLS	Fatigue Limit State
FRP	Fiber Reinforced Polymer
MP	Monopile
MSL	Mean Sea Level
TP	Transition Piece
ULS	Ultimate Limit State

List of Symbols

α	Fluid acceleration	$[m/sec^2]$
$\Delta\sigma$	Stress range	$[MPa]$
δ	Interface friction angle between sand and steel	$[degrees]$
η_0	Distribution function	$[-]$
γ	Non dimensional peak shape parameter	$[-]$
λ	Wave length	$[m]$
ω	radial natural frequency	$[rad/sec]$
Φ	Mode shape	$[-]$
ϕ_{soil}	Interface friction angle	$[degrees]$
ρ	Density	$[kg/m^3]$
ρ_{sand}	Submerged unit weight of sand	$[kN/m^3]$

σ	Spectral width parameter	$[-]$
A	Area	$[m^2]$
A_γ	Normalizing factor	$[-]$
C_D	Drag coefficient	$[-]$
C_M	Mass coefficient	$[-]$
C_T	Thrust coefficient	$[-]$
D	Fatigue damage	$[-]$
D_{cyl}	Cylinder diameter	$[m]$
E	Young's modulus of Elasticity	$[GPa]$
E_{soil}	Soil stiffness	$[Pa]$
f	Frequency	$[Hz]$
f_u	Ultimate stress	$[MPa]$
f_y	Yield stress	$[MPa]$
h	Water depth	$[m]$
$H_{a,n}$	Hydrodynamic transfer function	$[kg/sec^2]$
H_n	Mechanical transfer function	$[1/Pa \cdot m^{-1}]$
H_s	Significant wave height	$[m]$
I	Second moment of inertia	$[m^4]$
K	Stiffness matrix	$[kg/sec^2]$
k	wave number	$[-]$
L_v	Integral length scale	$[-]$
M	Mass matrix	$[kg]$
m	S-N curve slope	$[-]$
N	Number of cycles	$[cycles]$
p	Soil pressure	$[N/m]$
P_i	Probability of occurrence	$[-]$
p_u	Soil pressure at failure	$[N/m]$
$S_{Jonswap}$	Jonswap spectrum	$[m^2 \cdot sec]$
T	Time period	$[sec]$
T_p	Wave peak period	$[sec]$
u	Fluid velocity	$[m/sec]$
U_w	Wind speed	$[m/sec]$
y	Lateral displacement	$[m]$
z	Elevation from the MSL	$[m]$
z_{soil}	Soil depth variation	$[m]$

1

Introduction

1.1. Background

Nowadays, the request in sustainable power sources expands to an ever increasing extent. Along with the growing interest for “green” energy, the wind sector has been developed tremendously the past decades. Both the number of the installed wind turbines and the sizes of the wind turbines are increasing. Wind turbines constitute the most cost-effective way of the exploitation of the available wind potential, thus investigation of such structures is of particular interest. They may be constructed either in land areas (on-shore) or in sea areas (off-shore). Offshore wind turbines are becoming of special interest in recent years. Although an offshore wind turbine usually starts with a higher initial cost, it can outweigh a similar onshore one during its service life in a number of aspects such as: higher productivity due to stronger winds over sea areas, larger available installation areas and lower (or even non-existent) public nuisance [37].

A wind turbine could be considered as a structure that lies between a civil engineering structure and a machine [36]. More specifically, a wind turbine consists of structural elements (tower, substructure etc.) and a number of electrical and machine components with a control system (gear box, drivetrain etc.). Under a civil engineering perspective, the main components of a wind turbine could be considered the tower and the substructure. The tower is the element on the top of which the mechanical parts of the wind turbines, such as the nacelle and the blades, are installed. The tower is made of steel, has a circular cross section and is usually tapered (the cross-section size decreases with height linearly). The tower is connected to the substructure, the part of the wind turbine that is submerged in the water. The substructure may be founded directly in the seabed or based on a floating platform. Thus, there are two types of the substructure foundation, namely floating, which is by wires anchored at the bottom of the seabed, and fixed. Fixed wind turbines are used especially in sites of low or medium depths, while the construction of floating wind turbines is cost-effective in the case of deep waters. The most common type of design for fixed wind turbines, which is used for depths of approximately 30 meters, is the monopile. The monopile support structure of an off-shore wind turbine consists of two parts: the monopile penetrating the seabed and the transition piece connecting the monopile and the tower. The advantages of a monopile support structure, when compared with the other bottom fixed support structures, include minimal seabed preparation requirements, most competitive manufacturing costs owing to the simple structure and the most experienced support structure with off-shore wind turbines. The disadvantages include structure flexibility at large water depths, time-consuming installation and manufacturing constraints for large diameters and thickness that makes it very difficult to go beyond 30 to 40m water depth.

Regardless of the type of an offshore wind turbine, both structure and substructure are subjected to dynamic combinations of wind and wave loads with a wide range of frequencies.

This fact may arise critical issues during the turbine' s service life in terms of fatigue and power efficiency. Because of severe corrosion and uncertain cyclic loading in the sea environment, fatigue becomes potentially one of the main problems causing degradation in the long-term structural integrity. Both wind and waves play a major role in fatigue failure due to their continuity in time in random sequences, which produce random fluctuating stress responses in structural components. Hence fatigue is an important design driver and is typically governing for the design with the stiffness of the structure. Thus, special focus should be devoted on the appropriate design and analysis of this kind of structures for a safer and more reliable operation, in order to withstand the complex extreme nonlinear loads of the harsh environmental conditions in the ocean.Because a turbine system's capital cost is determined by its target reliability, it is important to achieve a tradeoff among the failure consequences, material consumption and failure probability at the design stage [36].

One part of specific interest for the fatigue assessment of a wind turbine is the way that the transition piece is connected to monopile. A novel connection method for offshore wind foundations has been invented by Fistuca BV. This new type of connection uses inclined planes to achieve a preload on flanges fixed to the monopile and transition piece, similar to bolted connection. The inclined plane, or wedge, is applied to the underside of the monopile flange, and to a radially displaceable dowel (Figure 1.1).

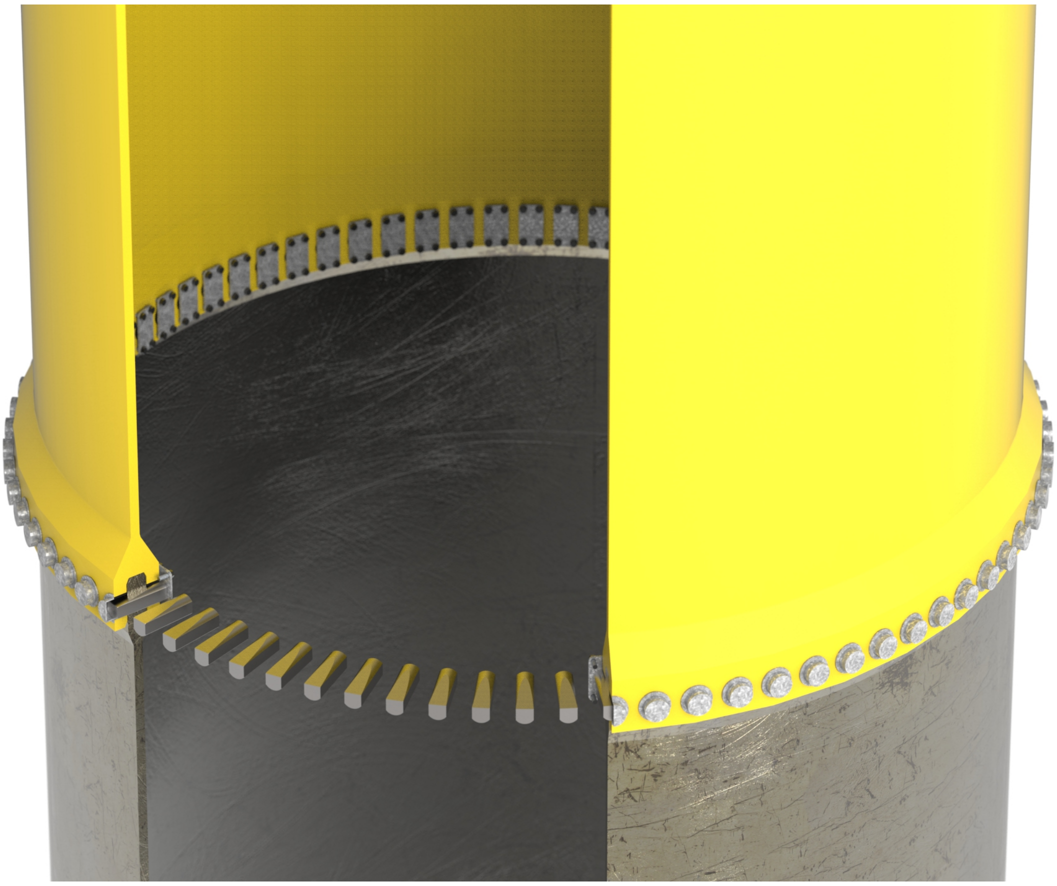

Figure 1.1: New concept of wedge connection.

1.2. The concept of Wedge Connection

Up until now, grouted and bolted connections were mostly used to seal and connect the transition piece to the monopile (Figure 1.2). However, it has been proven that both these types of connections have significant drawbacks and the cost of their construction is highly expensive. More specifically, the offshore wind industry experienced that the design of the grouted connections between the transition piece and the monopile did not result in an acceptable safety level [21]. Furthermore, bolted connections are really difficult to be installed and their installation is possible only above the waterline, they require regular torquing in order to prevent the loss of pretension and survive under fatigue loading, and they have limited scalability.

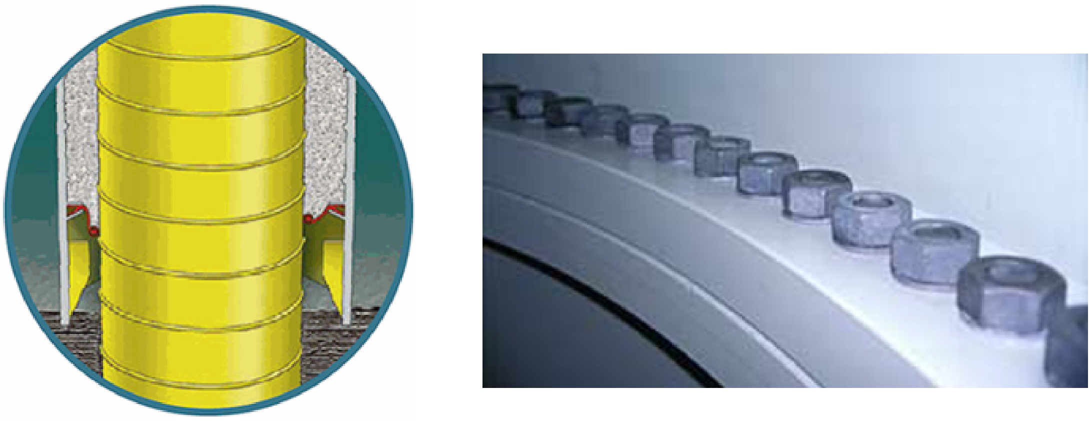

Figure 1.2: Left: grouted connection [8], Right: bolted connection [34].

Wedge connection is a new concept that Fistuca BV has developed and its main goal is to create a new type of connection that is economic, safe, fast, reliable and fail safe compared to the conventional bolted/grouted/slip connections that are used until now.

A basic flange is attached to the top of the monopile and a more complex flange is fitted to the bottom of the transition piece. More specifically, temporary sea fastening is done with remote control double acting wedges. Following the alignment, the double acting wedges are then used to position the transition piece on the monopile and the other wedges are then used to swiftly secure the structure.

One of the major advantages of this new concept of connection is the installation, which can be quicker, safer and cheaper as it has already been referred. The actuation can be done remotely with hydraulics actuators (Figure 1.3) or manually, using a light weight fastening tool (Figure 1.4). In both cases, these tools are installed in the internal side of the tower and are fitted at the bottom of the transition piece. The whole procedure of the tightening may last less than an hour.

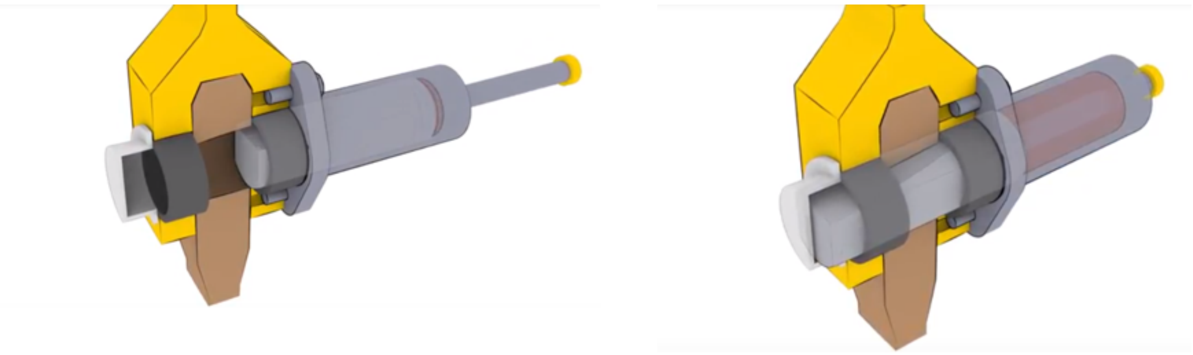

Figure 1.3: Positioning of dowels by hydraulic actuators

The pressure that is applied on the back side of the dowel during the final step of installation creates a vertical reaction force between the MP and TP flanges, as it is obvious in the Figure

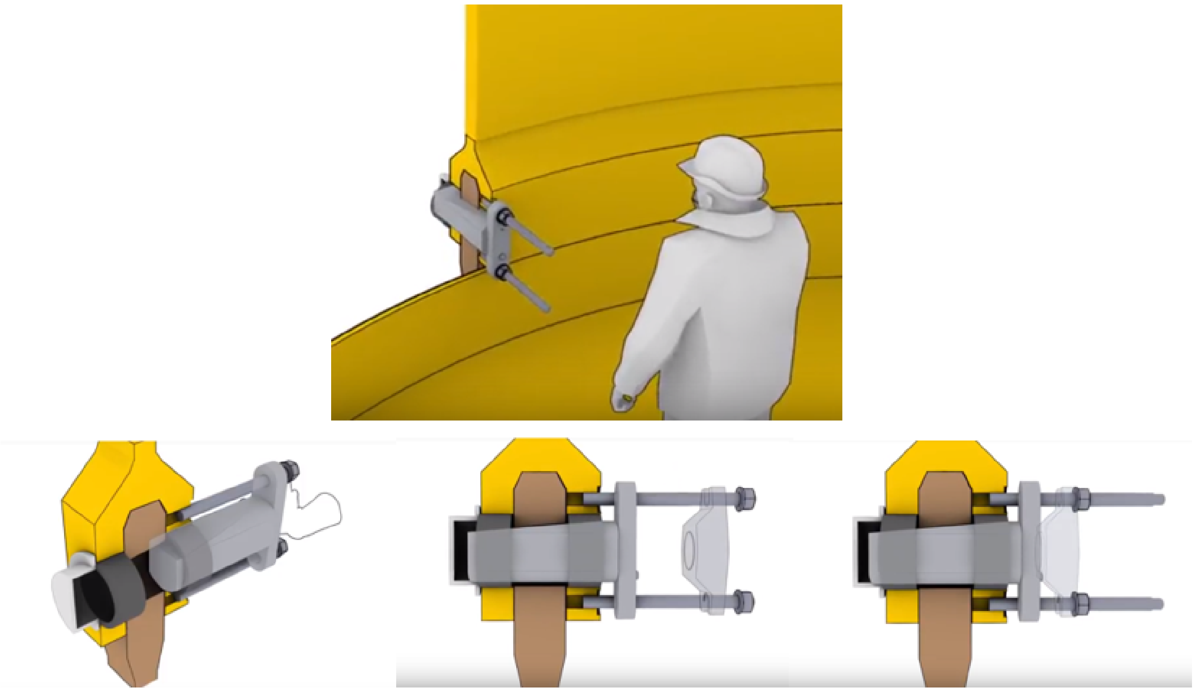

Figure 1.4: Positioning of dowels manually

1.5, which can be characterized and be referred as a preload force. This reaction force is necessary in order to keep in contact the two flanges and prevent or reduce any possible gap opening between them. The magnitude of the pressure that is applied is the one that determines whether and how much gap will be created (Figure 1.6 and 1.7).

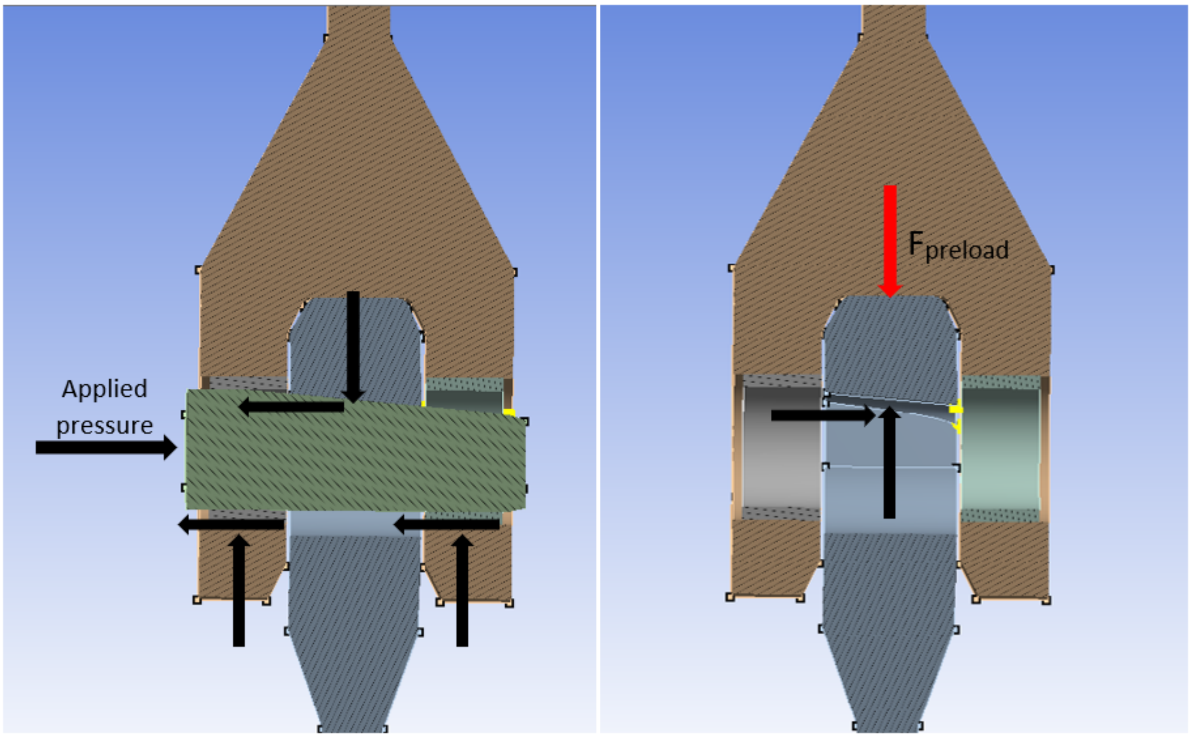

Figure 1.5: Load path of the wedge connection (left: reaction forces on dowel, right: transferred reaction forces on MP flange)

To be able to apply a known or a rather sufficient preload in the contact area between MP and TP flange, different levels of pressure have been applied on the dowel in order to measure both the developed preloading force and the gap that is occurred between the two flanges when the connection is loaded until the ULS load.

Figure 1.6: Gap growing for different levels of applied pressure on the dowel until the ULS load.

Figure 1.7: Gap opening for different levels of applied pressure on the dowel for the ULS load.

1.3. Research Objective

Calculation of the damage equivalent loads derived due to wind and wave loading, acting on the wind turbine structure at the level of the wedge connection, based on data of a specific site location and development of a Finite Element Model using the ANSYS WORKBENCH software to calculate the stress development on the different parts of the wedge connection and investigate the damage and the fatigue life of it.

As it has already been referred, tubular components are used in such types of structures, and this is due to their low drag coefficients and high strength-to-weight ratio characteristics. However, tubular members give rise to significantly high stress concentrations in the joints, and this is the reason for which fatigue life is a major concern.

An important parameter for the fatigue life of the connections is the effect of preload. Preload is used in order to clamp together two plates (MP and TP flanges in this case), create a frictional lock between the members and reduces the effect of fatigue loading on the members. Thus, it is very important for the design of the wedge connection to study how and if the presence of preload affect its fatigue performance.

Figure 1.8: Development of contact pressure between MP-TP flanges.

1.4. Research Methodology

In order to tackle the above-mentioned challenge a research methodology was established and followed:

1. Literature study.
2. Calculation of damage equivalent loads both due to wave and wind loading acting on the wind turbine structure at the level where the wedge connection is supposed to be located.
3. Modeling of the wedge connection using the 3D-CAD Solidworks for the design and ANSYS Workbench for the finite element analysis.
4. Modeling validation.
5. Apply the above damage equivalent loads for each case of damage loads with and without the presence of preload.
6. Selection of the most suitable S-N curve for each case and for each part of the wedge connection based on test specimens, in order to have an as better as possible estimation of the damage and the fatigue life of it.
7. How and if the presence of the preload influence the performance of the wedge connection in terms of fatigue.

1.5. Thesis Outline

The current thesis report is comprised by eight chapters and is organized as follows:

- Chapter 1 briefly gives a research background together with thesis problem description, objective and thesis outline.
- Chapter 2 contains theory about the phenomenon of fatigue in the structures and the way in which the damage is calculated.
- In Chapter 3, general information about the selection of the wind turbine and the reference site location are presented. Wave and wind loads acting in the structure are part of this chapter, as well.
- In Chapter 4, the damage equivalent loads due to wave in the frequency domain and due to wind in the time domain are calculated at the level of interest, where the wedge connection is located.
- In Chapter 5, details about how the FE model has been built, the assumptions that have been made, the materials that are used, the boundary conditions and the load cases/steps are discussed.
- In Chapter 6, FE analysis for the fatigue assessment is performed. Through the test specimens, the most suitable S-N curve is selected for the components of the connection and the damage calculation. Also, through the FEA, maximum principal stresses are plotted in order to calculate the damage and determine the most critical areas in terms of fatigue.
- In Chapter 7, a parametric study takes place in order to test how the change of several parameters may influence the results of the FEA and how significant this influence is or not for the fatigue assessment of the connection.
- Last, Chapter 8 summarizes the conclusions of this thesis and provides an outlook for possible future work.

2

Fatigue-Literature Study

To ensure that the structure will fulfill its intended function, a fatigue assessment, supported where is appropriate by a detail fatigue analysis, should be carried out for each individual member, which is subjected to fatigue loading.

2.1. Fatigue Definition

Structures subjected to repeated cyclic loadings can undergo progressive damage which shows itself by the propagation of cracks. This damage is called fatigue and is represented by a loss of resistance with time [9]. Fatigue damage occurs in the following stages:

- First appearance of a crack either detected visually or detected by means of physical measures, e.g. by the record of a chance in the local strain condition.
- Through-thickness crack: the fatigue crack starts from the front surface and grows through the thickness.
- Complete fracture or large displacement of the structural element such that the displacement becomes so important that the applied “jack load” cannot be maintained.

Fatigue has become increasingly important in design of offshore structures. The strength of the materials used in construction has been improved and the utilization of the materials is typically higher due to better methods for determining stresses. Both these factors have led to a general increased levels in constructions, which leads to higher risk of fatigue damage.

Moan and Naess [5] argue that fatigue is a challenging failure mode to deal with because:

- The fatigue process, especially initiation, is by nature unpredictable.
- It is difficult to translate laboratory tests to in-site conditions.
- It is difficult to model the load environment and the complex stress state.

2.2. Main parameters influencing the fatigue life

The fatigue life of a member or a structural detail subjected to repeated cyclic loadings is defined as the number of stress cycles that it can stand before failure [14].Depending on the member or structural detail geometry, its fabrication or the material used, the main parameters which can influence the fatigue strength/life are noted below:

- The stress difference, or most often called stress range.
- The structural detail category.
- The material characteristics.
- The environment.

2.3. S-N Curve Method

The nominal stress theory with S-N curves, or Wöhler lines, is the most commonly used method used by the engineers to determine the fatigue behavior of a structure. The S-N curve approach is based on experimental fatigue-test data which derived by fatigue tests on small specimens in laboratories until they fail [12].

DNV guidelines provide multiple S-N curves which should be chosen according to the nature of the fatigue problem. The choice of the S-N curve should be based on the following criteria:

- The geometrical arrangement of the detail.
- The direction of the fluctuating stress relative to the detail.
- The method of fabrication and inspection of the detail.

In this approach, the fatigue life N, which is the number of stress cycles to failure, is related to the stress range $\Delta\sigma$ with constant amplitude. More specifically, the S-N curve gives information regarding the number of cycles that a material can withstand under a cyclic load with constant mean value and amplitude. Specimens are subjected to a wide range of loads. The cycles, after which they fail for every different cyclic load, form the Wöhler curve. The relation between the number of cycles to failure N and the stress range $\Delta\sigma$ is given by:

$$N = A\Delta\sigma^{-m} \tag{2.1}$$

or

$$logN = logA - mlog\Delta\sigma \tag{2.2}$$

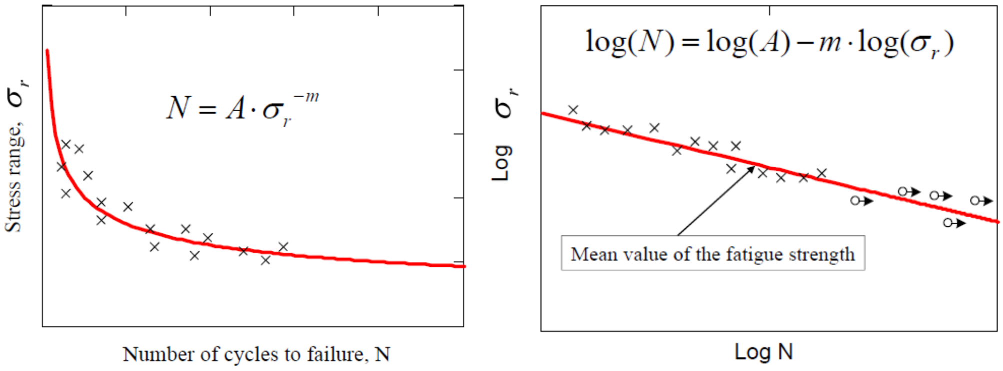

Figure 2.1: Quantitative dependence between number of cycles which defines strength of a structural detail in fatigue [29].

One significant limitation of the S-N curve is that the resulting plot is highly dependent on the test conditions (eg., the stress ratio $\sigma_{min}/\sigma_{max}$, sample geometry, sample surface condition and material). It is important to consider that, when using S-N curves, the applied reference stresses should correspond to the nominal stresses used in creating these curves. However, in an actual structure, it is rare that a match will be found with the geometry and loading of tested specimens. In most cases the actual details are more complex than the test specimens and the required nominal stresses are often not available or difficult to determine.

2.4. Fatigue Strength

The fatigue strength of the detail (fatigue category) is defined at a stress range $\Delta\sigma_C$ and N=2 million cycles. Change in slope occurs from 3 to 5 at 5 million cycles where the corresponding stress range is $\Delta\sigma_D$. A cut-off limit is defined at a stress range $\Delta\sigma_D$ and N=100 million cycles. Below this limit, no fatigue damages can take place.

Also, for constant amplitude loading, there is a limit (Constant Amplitude Fatigue Limit - CAFL) corresponding to stress ranges < $\Delta\sigma_D$, under which no damage occurs, which means that the fatigue life will be infinite (Figure 2.3). In variable amplitude loading, no CAFL exists.

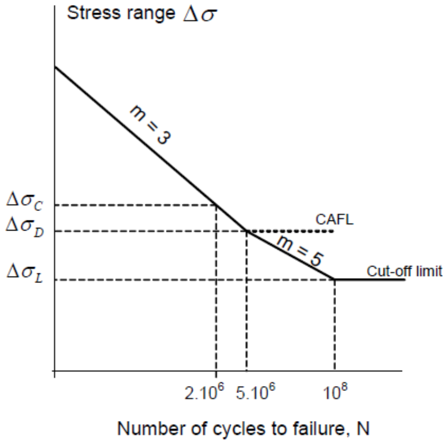

Figure 2.2: S-N curve Definition [29].

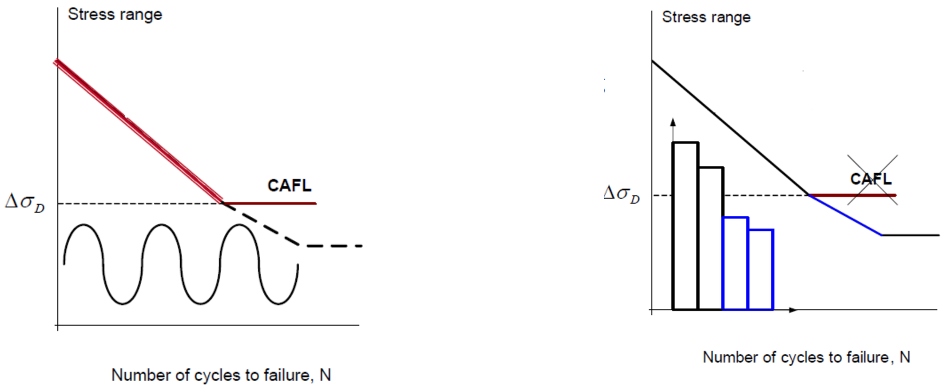

Figure 2.3: Constant amplitude fatigue limit [29].

2.5. Cumulative Fatigue Damage Rule

Having defined a relation between the stress range and the number of stress cycles failure as presented above, a damage accumulation rule is used to predict the cumulative damage under different stress ranges [13]. For this purpose, the Palmgren-Miner' s rule is commonly used in practice and it is implemented in design codes. This rule assumes a linear damage accumulation for different stress ranges. This linear damage accumulation scheme assumes that, for a loading with different stress ranges, each stress range $\Delta\sigma_i$ occurring n_i times results in a partial damage which can be represented by the ratio n_i/N_i. Here N_i represents the number of cycles to failure under the stress range $\Delta\sigma_i$. In case the stress range distribution function is known, the summation of the partial damages due to each stress range level can be replaced by an integral function. The failure is defined with the respect to the summation of partial damages and occurs when the theoretical value D=1.0 is reached (equation 2.3). This is represented graphically in Figure 2.4, where $\Delta\sigma_i$ is the applied stress range and N_R the number of loading cycles to fatigue failure at a certain stress range.

$$D = \frac{n1}{N1} + \frac{n2}{N2} + \frac{n3}{N3} + ... = \sum_{i=1}^{n_{tot}} \frac{n_i}{N_i} \leq \eta \tag{2.3}$$

According to DNV-RP-C203 [10] for the fatigue design of offshore steel structures, the fatigue damage D shall not exceed a certain value of the usage factor η. This factor depends on the accessibility of the structural member for inspection and is usually equal to 1.

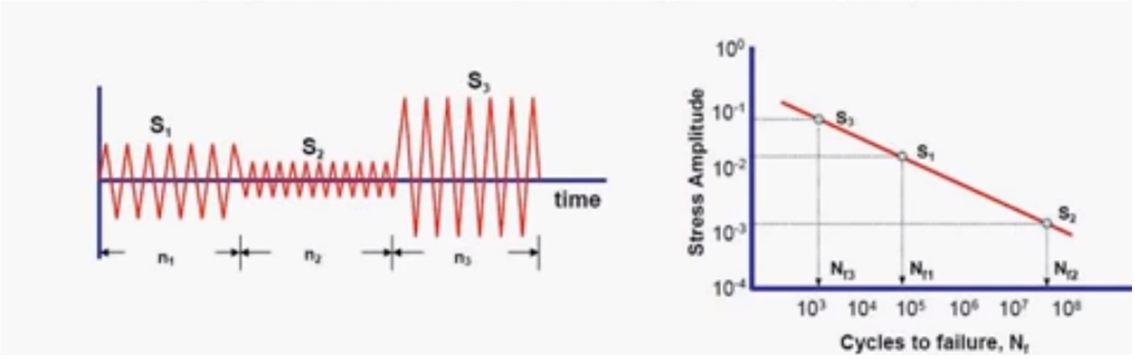

Figure 2.4: Damage accumulation scheme [29].

To find the total damage over the design life of the structure, the contribution to the total damage from each stress history during the design life needs to be summed up. This means that the total fatigue damage becomes:

$$D_{tot} = \sum_{i=1}^{N} D_i P_i \tag{2.4}$$

where D_i is the damage from a certain stress history, while P_i is the probability of occurrence for that stress history and N is the number of stress histories.

Applying a histogram to express the stress distribution, the number of stress blocks should be large enough to ensure reasonable numerical accuracy (not less than 20). Consideration should be given to selection of integration method as the position of the integration points may have a significant influence on the calculated fatigue life dependent on integration method.

Typically, the fatigue cycles imposed upon a structure are analyzed or measured over some fixed period of time. Thus, D, in equation 2.3, is usually expressed as the damage rate ΔD_t associated with the sample time t. If this damage rate is equal to average damage rate the service lifetime of the component T (i.e., $\Delta D_t = \Delta D_T$), then the service lifetime of the structure T is the reciprocal of ΔD_t, namely:

$$T = \frac{1}{\Delta D_T} = \frac{1}{\Delta D_t} \tag{2.5}$$

Again, Equation 2.5 is predicated on the assumption that failure will occur when the damage equals one, and that the damage rate computed over time t is representative of the average damage rate imposed upon the structure during its service lifetime. Namely, the number and distribution of fatigue cycles contained in the sample are essentially identical to the number and distribution over the structure’ s service lifetime.

2.6. Cyclic Counting Procedure for Random Stresses

A fluctuating stress to which a structural detail is subjected may have a stress history of constant amplitude or of variable amplitude (Figure 2.5 and 2.6).

In the case of variable amplitude stress variation, the stress range and cycle cannot be defined as simple as those for constant amplitude variation. In practice, stress time histories of offshore structures under wave and random loading sequences are random, and therefore, stress cycles and corresponding stresses can only be determined by counting algorithms. The main issue of counting procedure is that the stress history must be available in the time domain by recording, simulated numerically or obtained from a time domain dynamic analysis. In the stochastic analysis of offshore structures, stress spectra are calculated usually

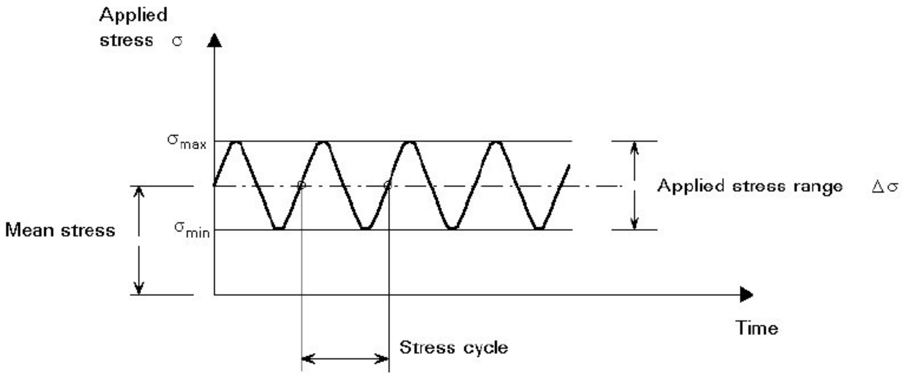

Figure 2.5: Constant amplitude stress history [16].

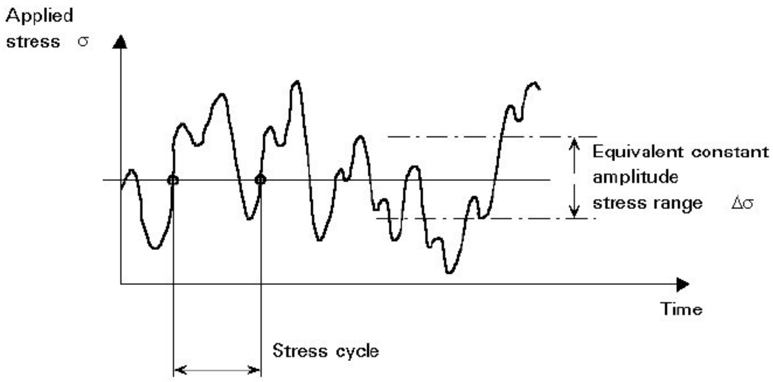

Figure 2.6: Variable amplitude stress history [16].

by applying a spectral analysis method. In order to apply a cycle counting algorithm the stress time history must be generated first from the corresponding spectrum. Then the cycle counting is processed. A number of methods have been proposed for stress cycle counting. The methods most commonly accepted for use in connection with Codes and Standards are the Reservoir and the Rainflow methods. The Reservoir cycle counting is employed for short stress histories while the Rainflow counting for longer and more complex stress histories.However, the Rainflow Method is generally regarded as the best estimator for the fatigue damage in actual lives, and therefore, it is used largely in practice [16].

2.6.1. Rainflow Cycle Counting

When the stress-time history is random, determination of the stress cycles and ranges are not possible analytically. In this case, a cycle counting algorithm is applied to determine stress cycles and ranges from time series of the stress process. For this reason, the Rainflow cycle counting method is widely used in practice and implemented in design codes. The rainflow method has obtained its name from an analogy of rain falling down a pagoda roof. It was developed by Matsuishi and Endo in 1968, and since then it has been studied and well documented in literature. Rychlik presented a mathematical definition for the rainflow cycle counting method, which enables closed-form computations from the statistical properties of the load signal. Since the cumulative damage is affected by the loading frequency, in random loading, the loading sequence is also random.

The rainflow cycle counting method is based on visualization of rainflow over a sequence of pagoda roofs. Essentially, it counts half cycles. To simulate a pagoda roof from a stress time series, the peaks and troughs of the stress time series are connected by linear lines as shown in Figure 2.7. Then the linearized model is rotated clock wise with 90° such that the time axis is in vertical direction with the origin at the top and positive downward, as shown in Figure 2.8a in which example stress values of peaks and troughs are written relative to mean values. In this figure, the odd numbers denote the troughs and even numbers denote the peaks. Rainflow is assumed to begin from a peak or a trough and keeps falling on the roof until it stops according to the following conditions:

1. A drop begins to flow right from a trough or left from a peak onto subsequent roofs.
2. When a drop stats from a trough, it stops if it meets an equal or deeper trough than that it is started from, e.g., path (1-2-2') in Figure 2.8 b. The drop falls on another roof until a stop condition arises, e.g., path (3-4-4'-6-6'-10-10') in Figure 2.8 b. The drop stops flowing when it meets a flow from an earlier path, e.g., path (5-4') in Figure 2.8 b.
3. When a drop starts from a peak, it stops if it meets an equal or larger peak than it is started from, e.g., path (2-3-3') in Figure 2.8 b. The drop falls on another roof until a stop condition arises, e.g., path (6-7-7'-9-9') in Figure 2.8 b. The drop stops flowing when it meets a flow from an earlier path, e.g., path (8-7) in Figure 2.8 b.'
4. A drop stops flowing flowing when it reaches the tip of the roof (end of stress history record).
5. The stress range of a half cycle, which is equivalent to that of a constant amplitude load, is defined as the projection of a rainflow path between the start and stop points.

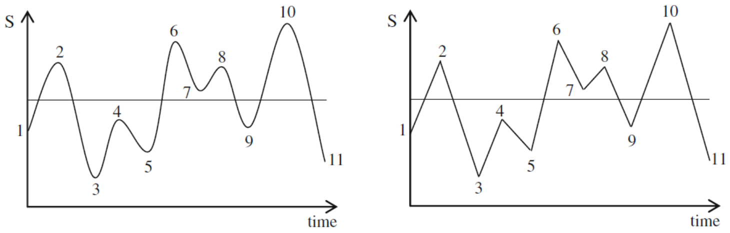

(a) (b)

Figure 2.7: An example stress time history and the equivalent linear model[16].

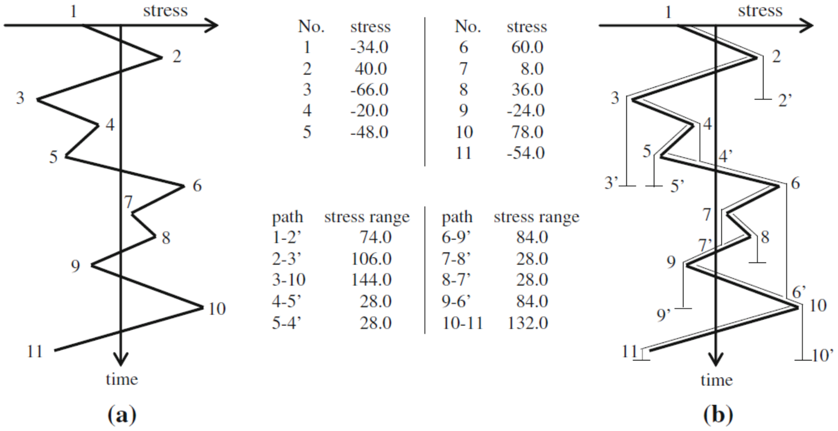

No.	stress	No.	stress
1	-34.0	6	60.0
2	40.0	7	8.0
3	-66.0	8	36.0
4	-20.0	9	-24.0
5	-48.0	10	78.0
		11	-54.0

path	stress range	path	stress range
1-2'	74.0	6-9'	84.0
2-3'	106.0	7-8'	28.0
3-10	144.0	8-7'	28.0
4-5'	28.0	9-6'	84.0
5-4'	28.0	10-11	132.0

(a) (b)

Figure 2.8: An example pagoda roof and corresponding rainflow cycle counting patterns. a The pagoda roof model of stress history b The rainflow patterns [16].

3

Environmental Loading

In order to perform analysis of a structure, the environmental data from the site is of high importance, as the environmental loads are estimated based on that.

3.1. Reference Turbine

The structure design is referred to a generic 8MW turbine, based on limited data available from the Vestas V164-8.0MW model. Turbine or tower parameters are not available from Vestas, but are approximated using Enersea in-house data and public papers [3]. Relevant parameters for the support structure design are listed in the following Table.

Turbine Parameters	Value	Unit
Rated power	8.0	MW
Rotor diameter	164	m
Mass of rotor and nacelle	460	tonnes
Tower mass	375	tonnes
Wedge mass	30	tonnes
Cut-in wind speed	4.0	m/sec
Cut-out wind speed	25.0	m/sec
Nominal wind speed	15	m/sec
Lower bound rotor speed	5.4	rpm
Upper bound rotor speed	11.5	rpm
Nominal rotor speed	10.6	rpm
1P Frequency range	0.09-0.192	Hz
3P Frequency range	0.270-0.575	Hz
Nominal operating frequency	0.177-0.530	Hz
Monopile diameter	6.5	m
Monopile thickness	70	mm
Hub height (above sea level)	108	m
Wedge connection elevation (above MSL)	4	m

Table 3.1: Relevant reference turbine parameters

For the purpose of this thesis, it is assumed that both the diameter and thickness of the tower vary along its length (tapered section: top diameter =4.5m, top thickness=0.030m, bottom diameter=6.5m, bottom thickness=0.070m), while the diameter and the thickness of the monopile structure are assumed to be constant along its entire length.

3.2. Reference Location

An offshore wind turbine support structure is designed based on the metocean conditions which highly depend on the choice of the project location. For this analysis, the North Sea state with water depth of 40m has been selected (Figure 3.1), as the key design objective is to produce a design that is suitable for a variety of projects sites. Information for this location are presented in Tables 3.2 and 3.3 and Figure 3.2 as well.

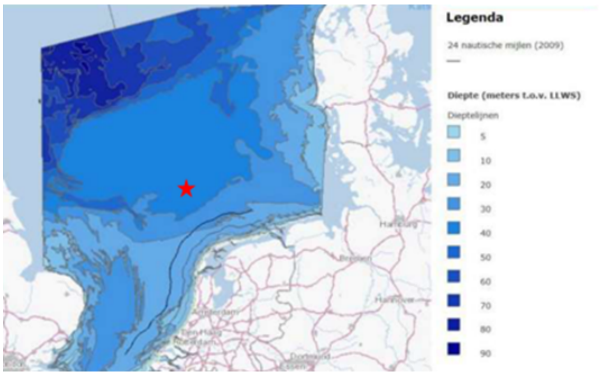

Figure 3.1: North Sea [3].

Case	Wave Height (m)	Peak Period (sec)	Number of Cycles (25 years)	Probability
1	0.5	3.2	10305098	0.09608
2	1	4.3	59092332	0.551
3	2	5.9	30269367	0.2822
4	3	6.9	5779211	0.05388
5	4	7.8	1326349	0.01237
6	5	8.6	345151	0.003218
7	6	9.2	96626	9.009E-04
8	7	9.8	28093	2.619E-04
9	8	10.3	8322	7.759E-05
10	9	10.8	2498	2.329E-05
11	10	11.2	762	7.105E-06
12	11	11.6	238	2.219E-06
13	12	12	76	7.086E-07
14	13	12.3	25	2.331E-07
15	14	12.6	8	7.459E-08
16	15	12.9	3	2.797E-08
17	16	13.2	1	9.324E-09
18	17	13.8	0.5	4.662E-09

Table 3.2: North Sea Data: wave information.

In Table 3.3, the wind speed refers to the mean wind speed at 10 meters above the MSL. In order to calculate the probability of the wind speed at the installation site, the Weibull distribution has been used. It has been proven that the Weibull function fits the distribution of the average wind speeds relatively well at most sites [17].

The Weibull is a two parameter distribution function and it can be described by its probability density function $f_{Weibull}(V)$ and cumulative distribution function $F_{Weibull}(V)$ as given below respectively [39]:

$$f_{Weibull}(V) = \frac{k}{c}\left(\frac{V}{c}\right)^{k-1} e^{-\left(\frac{V}{k}\right)^{k}} \tag{3.1}$$

$$F_{Weibull}(V) = 1 - e^{\left(-\left(\frac{V}{c}\right)^{k}\right)} \tag{3.2}$$

Case	Wind speed (m/sec)
1	4.48
2	5.94
3	7.87
4	9.28
5	10.44
6	11.43
7	12.31
8	13.10
9	13.83
10	14.51
11	15.15
12	15.74
13	16.31
14	16.85
15	17.37
16	17.86
17	18.33
18	18.79

Table 3.3: North Sea Data: wind information.

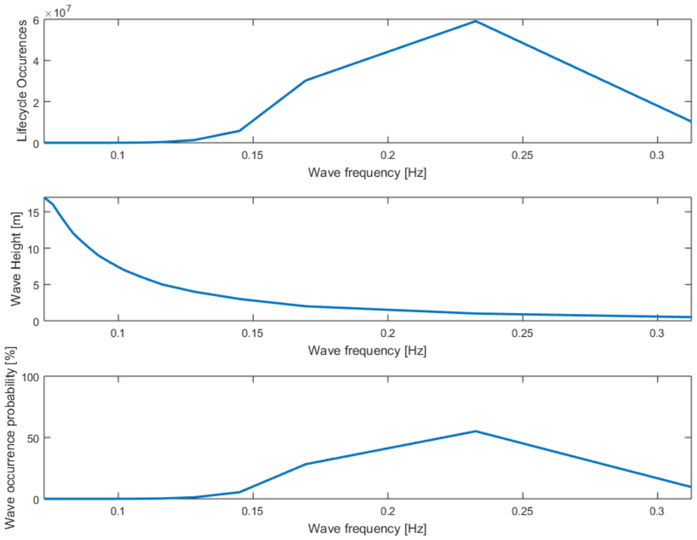

Figure 3.2: North Sea State Information

where,

k	is the shape factor. It specifies the shape of a Weibull distribution and takes a value between 1 and 3 (it is taken equal to 2.2 in this case).
c	is the scale factor,
V	is the mean wind speed at the hub level.

To calculate the scale factor of the Weibull distribution function, the empirical expression that has been derived for the North Europe coast has been used. According to this:

$$c = \frac{U_{average}}{\Gamma\left(1+\frac{1}{k}\right)} \tag{3.3}$$

$U_{average}$ is referred to the annual mean wind speed of the reference location ($= 11.4 m/sec$).

In the following figure, the resulting Weibull wind speed distribution and the cumulative wind speed distribution are presented.

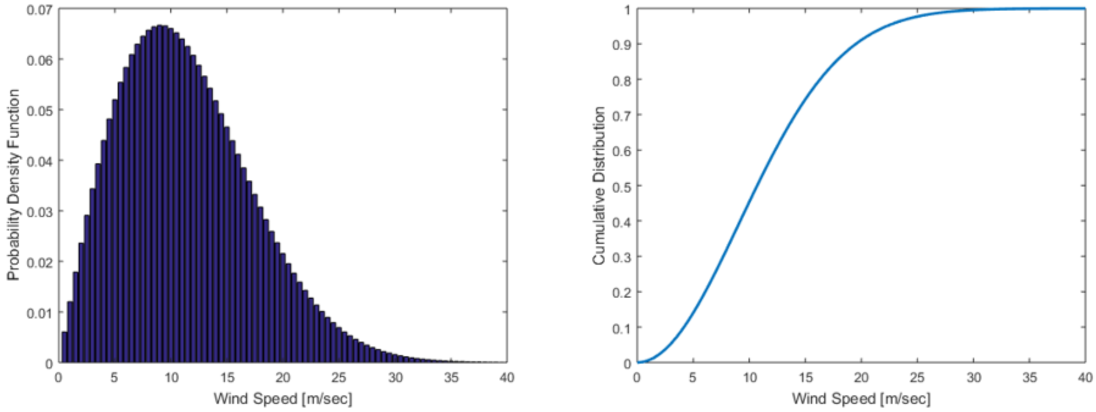

Figure 3.3: Left: Weibull wind speed distribution, Right: Weibull cumulative wind speed distribution.

From the Weibull distribution function the following results have been exported for the values of the mean wind that have been shown in Table 3.2:

Mean Wind Speed [m/sec]	**Weibull Probability**
4.48	0.0480
5.94	0.0580
7.87	0.0654
9.28	0.0667
10.44	0.0653
11.43	0.0627
12.31	0.0596
13.10	0.0561
13.83	0.0526
14.51	0.0491
15.15	0.0458
15.74	0.0425
16.31	0.0395
16.85	0.0366
17.37	0.0339
17.86	0.0314
18.33	0.0291
18.79	0.0269

Table 3.4: Weibull Probability of occurrence for each mean wind speed.

3.3. Mathematical Model of the Wind Turbine

For the mathematically dynamic analysis of a wind turbine, the wind turbine can be considered as a beam where the Euler-Bernoulli Beam Theory can be applied (bending beam) with flexural stiffness EI (Nm^2), a cross sectional area A (m^2) and a mass density ρ (kg/m^3).

$$EI\frac{\partial^4 w(x,t)}{\partial x^4} + \rho A\frac{\partial^2 w(x,t)}{\partial t^2} = f(x,t) \tag{3.4}$$

To simulate the beam model as better as possible in order to correspond to the real one, a concentrated mass is added on the free end of the beam model which represents the rotor-nacelle mass. Furthermore, in order to take into account any changes in the structural properties at the interface between the support structure and the turbine tower, where the wedge connection is assumed to be located, a local mass is added at the appropriate location in the beam model. The tapered cross section of the tower has been considered as well.

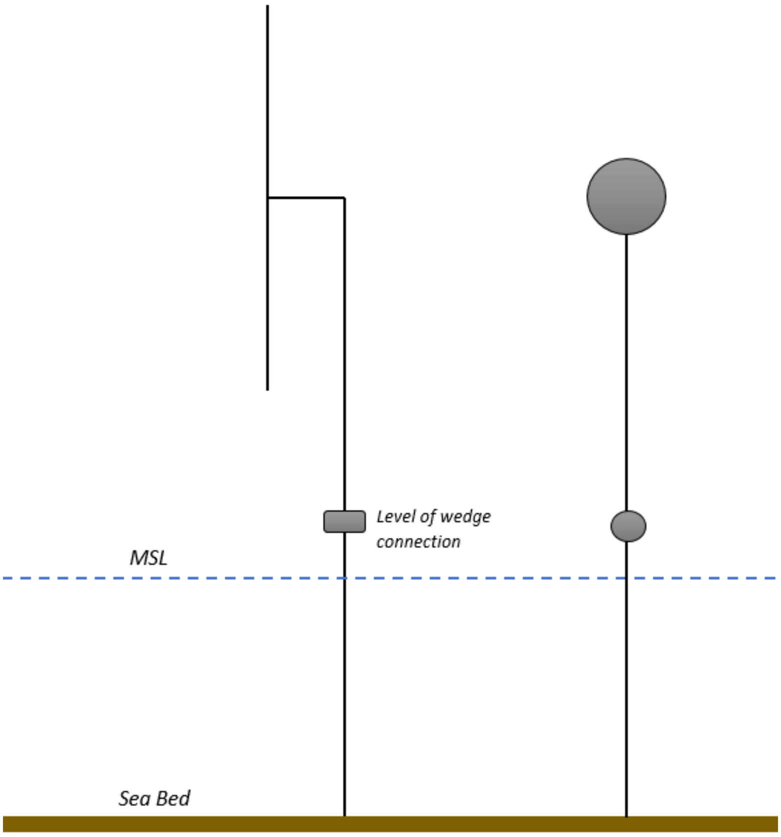

Figure 3.4: Beam Model of the wind turbine.

For better accuracy and in order to solve the problem numerically using Matlab, the beam needs to be discretized.

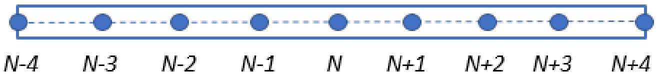

Figure 3.5: Beam Model discretization.

In addition, in order to have a beam model which will simulate the real one as better as possible, it would be necessary to take into account the interaction between the soil and the foundation; in other words, how the deformability of soil affects the response of the structure [35]. This can be achieved by adding several springs on the embedded length of the monopile, which will represent the soil stiffness at each unit of depth, as it is shown in Figure 3.6.

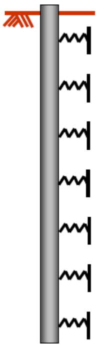

Figure 3.6: Soil modeling by making use of spring elements.

3.3.1. Soil parameters and p-y curves

Soils in the offshore environments are stratified and may be composed by different layers of sand, clay or a combination of both. However, for the purpose of this thesis, as it is really difficult to get information about the soil conditions at a wind farm site due to their significant variability, a simplified, homogeneous and single type soil profile of dense sand has been assumed, which is typical for the North Sea.

The lateral resistance of this profile is determined by using the API method with the following design parameters that have been taken by a previous thesis project [3]:

Interface friction angle (sand)	$\phi_{soil} = 35°$
Interface friction angle between sand and steel	$\delta = 30°$
Limiting shaft friction	$f = 67KPa$
Bearing factor	$N_q = 40$
Limiting end bearing	$q = 9.6MPa$
Submerged unit weight of sand	$\rho_{sand} = 10KN/m^3$

The stiffness of the soil varies with depth, so despite the fact that homogeneous soil conditions have been assumed, it must be discretized into several layers. The embedded length of the monopile is estimated as 3.5 times the monopile diameter according to the previous thesis project. Thus, this length is divided into elements of 1 meter length. The stiffness of each element is defined by making use of the p-y curves. According to API (RP2A), the deflection of a certain soil spring at position z below the seabed is denoted by y [2]. Based upon Winkler Foundation theory, the soil–pile resistance p (in units of force per length) for sands is defined by:

$$p = A \cdot p_u \cdot tanh\left(\frac{k_{py} \cdot z_{soil}}{A \cdot p_u} y\right) \tag{3.5}$$

where,	A	is a dimensional value equal to 0.9 for cyclic loading,
	p_u	is the soil pressure at failure,
	k_{py}	is the initial modulus of sub-grade reaction,
	z_{soil}	is the depth and
	y	is the lateral displacement.

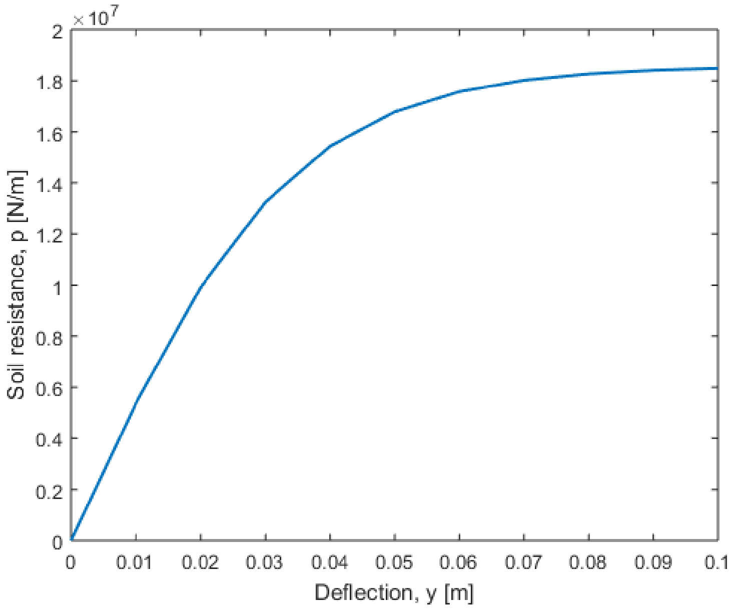

Figure 3.7: Resulting p-y curve at 23m below the sea bed.

The stiffness per unit of length E_{py} is calculated at each layer using the following simple relation, where y is a value of the lateral displacement of the embedded monopile.

$$E_{soil} = \frac{p}{y} \tag{3.6}$$

The p-y curve differentiates for each depth, therefore, each spring has a different p-y curve and as a result a different stiffness. More specifically, as the depth increases, the stiffness of the curve becomes higher. Due to non-linearity of the p-y curve, in order to calculate the stiffness of the soil, the lateral displacement of the monopile at each depth should be known. However, for the purpose of this thesis, the stiffness of the soil has been calculated by considering only the first linear part of the p-y curve.

For each one of the elements of the Euler Bernoulli beam that is located below the seabed, the above calculated value of stiffness E_{soil} is added to the stiffness matrix of the structure, derived in the following section.

At this point it should be referred that this method, which is used based on the current design codes (API and DNVGL), is a crude approximation and is not very accurate for large diameters piles, as it is based on slimmer and slender piles than those used in offshore industry [30]. More specifically, it has been proven that this method underestimates the stiffness of the soil. However for the purpose of this thesis, the assumption that this stiffness is acceptable has been made.

3.3.2. Modal Analysis

The central finite difference scheme is used to approximate the derivatives with respect to space, and after applying the boundary conditions for the two ends (free-free), the resulting equation of the beam is:

$$\rho \cdot A \cdot \begin{bmatrix} 1 & 0 & 0 & 0 & \ldots & 0 & 0 & 0 & 0 \\ 0 & 1 & 0 & 0 & \ldots & 0 & 0 & 0 & 0 \\ 0 & 0 & 1 & 0 & \ldots & 0 & 0 & 0 & 0 \\ 0 & 0 & 0 & 1 & \ldots & 0 & 0 & 0 & 0 \\ \ldots & \ldots & \ldots & \ldots & \ldots & \ldots & \ldots & \ldots & \ldots \\ 0 & 0 & 0 & 0 & \ldots & 1 & 0 & 0 & 0 \\ 0 & 0 & 0 & 0 & \ldots & 0 & 1 & 0 & 0 \\ 0 & 0 & 0 & 0 & \ldots & 0 & 0 & 1 & 0 \\ 0 & 0 & 0 & 0 & \ldots & 0 & 0 & 0 & 0 \end{bmatrix} \cdot \begin{bmatrix} \ddot{w}_1 \\ \ddot{w}_2 \\ \ddot{w}_3 \\ \ddot{w}_4 \\ \ldots \\ \ddot{w}_{169} \\ \ddot{w}_{170} \\ \ddot{w}_{171} \\ \ddot{w}_{172} \end{bmatrix} +$$

$$\frac{EI}{l^4} \cdot \begin{bmatrix} 2 & -4 & 2 & 0 & 0 & 0 & \ldots & 0 & 0 & 0 & 0 & 0 & 0 \\ -2 & 5 & -4 & 1 & 0 & 0 & \ldots & 0 & 0 & 0 & 0 & 0 & 0 \\ 1 & -4 & 6 & -4 & 1 & 0 & \ldots & 0 & 0 & 0 & 0 & 0 & 0 \\ 0 & 1 & -4 & 6 & -4 & 1 & \ldots & 0 & 0 & 0 & 0 & 0 & 0 \\ \ldots & \ldots & \ldots & \ldots & \ldots & \ldots & \ldots & \ldots & \ldots & \ldots & \ldots & \ldots & \ldots \\ 0 & 0 & 0 & 0 & 0 & 0 & \ldots & 1 & -4 & 6 & -4 & 1 & 0 \\ 0 & 0 & 0 & 0 & 0 & 0 & \ldots & 0 & 1 & -4 & 6 & -4 & 1 \\ 0 & 0 & 0 & 0 & 0 & 0 & \ldots & 0 & 0 & 1 & -4 & 5 & -2 \\ 0 & 0 & 0 & 0 & 0 & 0 & \ldots & 0 & 0 & 0 & 2 & -4 & 2 \end{bmatrix} \cdot \begin{bmatrix} w_1 \\ w_2 \\ w_3 \\ w_4 \\ \ldots \\ w_{169} \\ w_{170} \\ w_{171} \\ w_{172} \end{bmatrix} = \begin{bmatrix} F_1 \\ F_2 \\ F_3 \\ F_4 \\ \ldots \\ F_{169} \\ F_{170} \\ F_{171} \\ F_{172} \end{bmatrix} \tag{3.7}$$

where,

ρ	density of the material of the beam,
A	cross section area of the beam,
E	elastic modulus of the beam,
I	second moment of inertia,
l	length of each element,
w	deflection of each node,
F	force applied on each node.

Having obtained the mass and stiffness matrices, the natural frequencies can be calculated now, using the undamped equation of motion:

$$[M] \cdot \ddot{u} + [K] \cdot u = 0 \tag{3.8}$$

and assuming a solution in the following form (harmonic motion):

$$u(t) = \Phi \cdot sin(\omega \cdot t) \tag{3.9}$$

Substitution of the equation 3.9 to equation 3.8 results to:

$$\Phi\left(-\omega^2 + \frac{K}{M}\right) = 0 \tag{3.10}$$

or,

$$\omega = \sqrt{\frac{K}{M}} \tag{3.11}$$

In order to avoid the trivial solution, $\Phi = 0$ is disregarded [24].

In the Figure 3.8, the resulting shape modes for the first three natural frequencies are presented.

	Natural Frequency rad/sec	Frequency Hz
1st	1.4786	0.2353
2nd	8.6459	1.3760
3rd	25.4679	4.0533

Table 3.5: Three first natural frequencies of beam model.

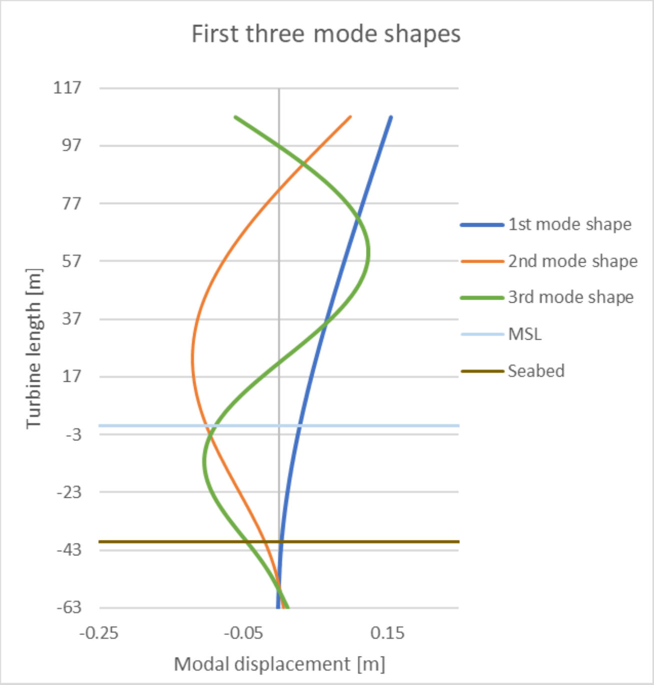

Figure 3.8: Three first mode shapes of beam model.

Thus, having a first clue on the Figure 3.8, one would say that 2nd and 3rd mode shapes will be important for the fatigue assessment of the beam at the level of the wedge connection, as well. However, as it will be seen in the following sections, only the 1st natural frequency (thus 1st mode shape) is of importance, as both 2nd and 3rd natural frequencies are higher than the 3P frequency of the turbine.

3.4. Wave Spectral Density

The random nature of a real state can be represented by the superposition of several individual components, with each of them having its own amplitude, peak frequency and direction of propagation. Neglecting the directional wave spectrum, there are two most frequently used formulations of spectra in the offshore sector: the Pierson-Moskowitz for a fully developed sea (or at infinite fetch)and the JONSWAP for a developing sea (or fetch-limited) spectrum [23].

The JONSWAP spectrum is an improved-extended version of the Pierson-Moskowitz based on further measurements of wave spectra in the North Sea, and incorporating a peak enhancement factor.

The equation for the JONSWAP spectrum according to DNV-RP-C205 [11] is:

$$S_{Jonswap}(\omega) = A_{\gamma}\frac{5}{16}H_s^2\omega_p^4\omega^{-5}exp\left(-\frac{5}{4}\left(\frac{\omega}{\omega_p}\right)^{-4}\right)\gamma^{exp\left(-0.5\left(\frac{\omega-\omega_p}{\sigma\omega_p}\right)^2\right)} \tag{3.12}$$

where,

ω	angular wave frequency, $\omega = \frac{2\pi}{T}$
T	wave period
ω_p	angular peak frequency, $\omega_p = \frac{2\pi}{T_p}$
T_p	peak period
σ	spectral width parameter
γ	non dimensional peak shape parameter
$A_\gamma = 1 - 0.287ln(\gamma)$	a normalizing factor

σ is given as:

$$\sigma = \begin{cases} 0.07 & for \quad \omega \leq \omega_p \\ 0.09 & for \quad \omega > \omega_p \end{cases} \tag{3.13}$$

and γ is given as:

$$\gamma = \begin{cases} 5 & for \quad \frac{T_p}{\sqrt{H_s}} \leq 3.6 \\ exp\left(5.75 - 1.15\frac{T_p}{\sqrt{H_s}}\right) & for \quad 3.6 < \frac{T_p}{\sqrt{H_s}} \leq 5 \\ 1 & for \quad 5 < \frac{T_p}{\sqrt{H_s}} \end{cases} \tag{3.14}$$

When the peak shape parameter is taken as $\gamma = 1.0$, the JONSWAP spectrum is equal to the Pierson-Moskowitz spectrum.

The presence of the normalizing factor A_γ is to ensure that the area under the Jonswap spectrum still represents the real energy density of the sea state.

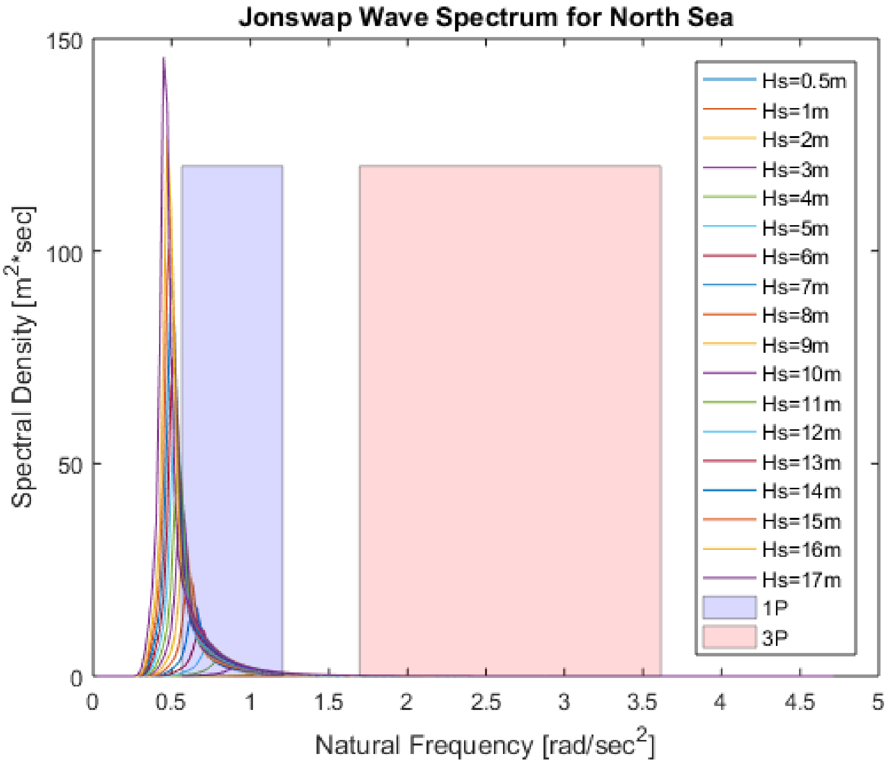

Figure 3.9: JONSWAP Spectrum for all Sea States.

Figure 3.9 shows the JONSWAP spectrum for each one of the Sea States. 1P and 3P represent the rotational frequency of the rotor and the blade passing frequency respectively. The rotational frequency is defined by the range starting at the minimum rotational speed at cut-in wind speed and ending at the maximum rotational speed [38]. The blade passing frequency accounts for the excitation generated when each blade passes by the rotor. Both frequencies shall be avoided in the design.

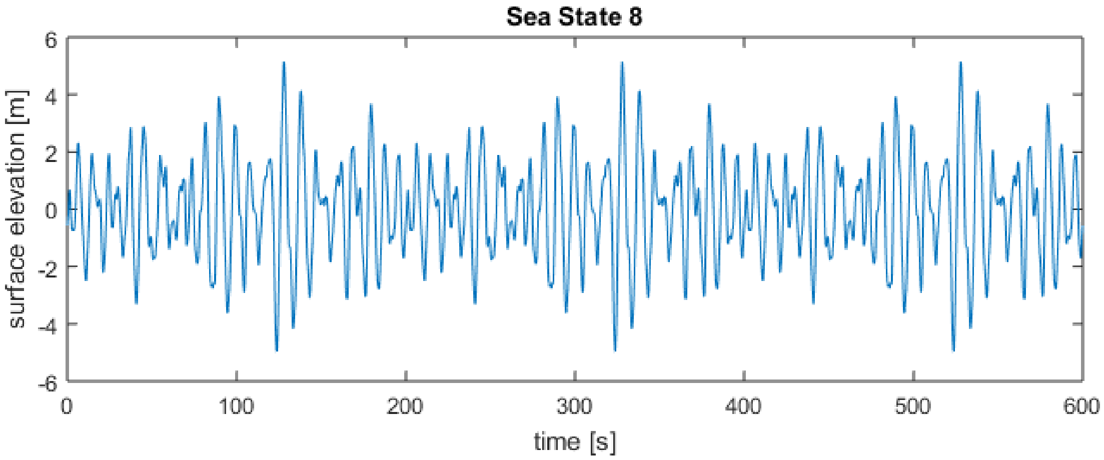

Figure 3.10: Time series realization of water elevation derived from wave spectrum.

The generated spectra can be used to calculate wave loads on the wind turbine structure directly in the frequency domain.In Figure 3.10, a 10-minute time history for a 7meter wave has been derived.

3.5. Morison's Equation

Morison's equation was originally formulated for calculating the wave loads on fixed vertical cylinders. It consists of two force components, one related to water particle acceleration, the inertia force, and one related to water particle velocity, the drag force [27] and is defined as:

$$F_{Morison} = \rho \frac{\pi D_{cyl}^2}{4} C_M a dz + \frac{\rho}{2} C_D D_{cyl} \left|u\right| u dz \tag{3.15}$$

where,

C_M	is the mass coefficient
C_D	is the drag coefficient
u	is the fluid velocity given by the following equation:

$$u(z,t) = \frac{\omega H}{2} \frac{cosh[k(z+h)]}{sinh(kh)} cos(\omega t) \tag{3.16}$$

where,

k	is the wave number,
h	is the water depth,
z	is the elevation from the MSL (+ is upward)

α is the fluid acceleration given by:

$$a(z,t) = -\frac{\omega^2 H}{2}\frac{cosh[k(z+h)]}{sinh(kh)}sin(\omega t) \tag{3.17}$$

D_{cyl} is the cylinder diameter
ρ is the water density

For large diameter cylinders, such as those used in the wind turbine support structures, the inertia loads are dominated, accounting for more than 90% of the resulting force (Figure 3.11). These inertia loads are quadratically proportional to the structure diameter, which contributes to the increased importance of wave loads in the assessment of large offshore support structures.

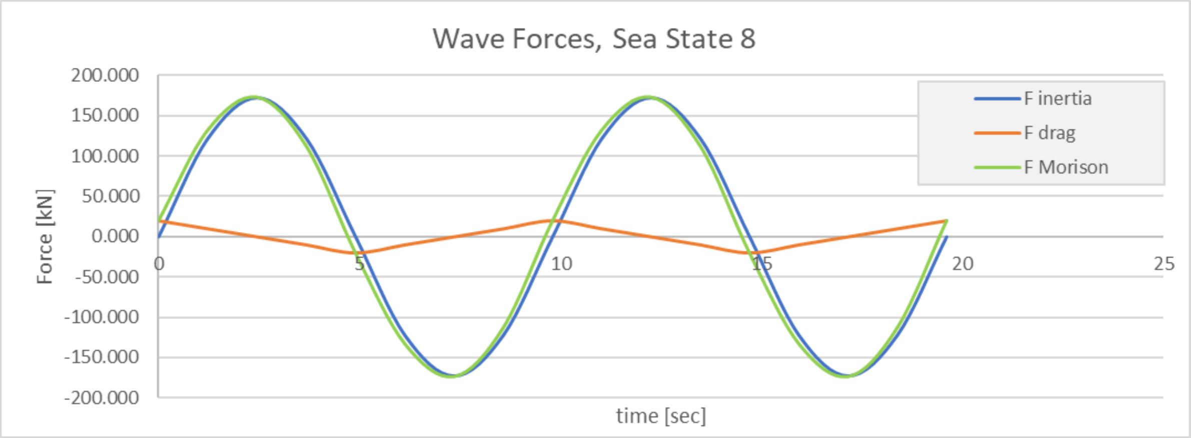

Figure 3.11: Morison Force for Sea State 8 with C_D=0.8.

The drag coefficient C_D may vary between 0.6 and 1.05 over the structure lifetime, based on the roughness of the cylinder, influenced by marine growth. The inertia coefficient C_M is generally taken equal to 2.0. However, for large diameter structures, like the monopile support structures for wind turbines, placed in relatively shallow water with consequently reduced wave length, the validity of Morison equation can be compromised due to diffraction of the waves.(The basic assumption of Morison's equation is that the submerged members for which the wave loads are calculated do not affect the waves, but this assumption is valid only when the cylinder diameter is relatively small compared to wave length.)

To incorporate the diffraction into the Morison equation, the MacCamy-Fuchs correction [22] is introduced. This correction reduces the magnitude of the inertia coefficient and, as it is obvious from the below expression, is dependent on the ratio of diameter to the wave length.

$$C_M(z) = -2.5\left(\frac{D}{\lambda_0}\right)^3 + 7.53\left(\frac{D}{\lambda_0}\right)^2 - 7.9\left(\frac{D}{\lambda_0}\right) + 3.2 \leq 2.0 \tag{3.18}$$

Figure 3.12 represents the reduction of the inertia coefficient for increasing ratio.

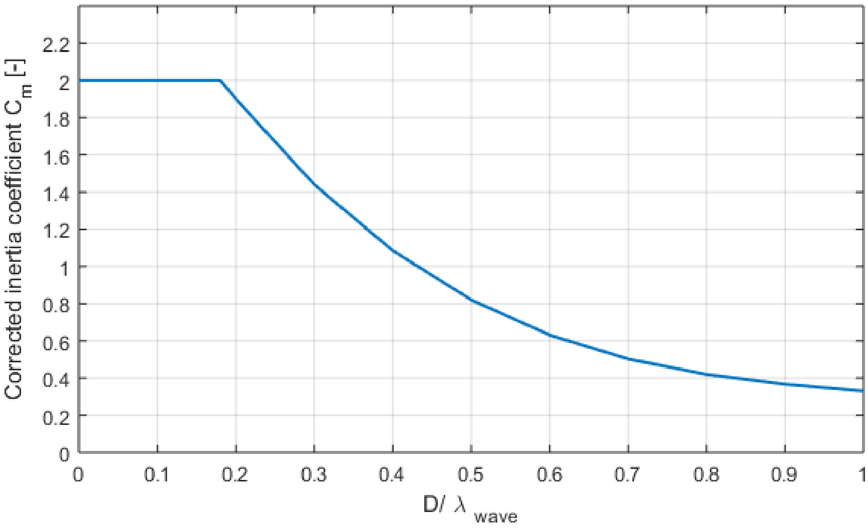

Figure 3.12: MacCamy-Fuchs diffraction correction of the inertia coefficient C_M.

3.6. Wind Speed & Turbulence

The normal wind conditions are specified in terms of air density, a long-term distribution of the 10-minute mean wind speed and turbulence. The 10-minute wind speed is considered to be constant over this short period. Wind speed data is height dependent with the mean wind speed at the hub height being used as reference. The wind speed at different heights can be calculated, while taking into account the mean wind speed at hub height and the wind speed profile above the still water level.

The typical wind spectra over a broad range of frequencies show that the mean wind speed over a period of about 10 minutes can be regarded as constant, forming a wind state: a state during which only the turbulence term fluctuates. Focusing on the wind direction i, a time-series of wind speed is characterized by a mean wind speed and a standard deviation. These define the turbulence intensity as follows:

$$TI_i = \frac{\sigma_i}{U_w} \tag{3.19}$$

where TI_i is the turbulence intensity in i direction and σ_i the standard deviation of wind speed in i direction [23].

Turbulence in the wind has an important anticipation on the fatigue behavior of the wind turbines, so it affects their lifetime. It has been proven that the turbulence affect the lifetime negatively, in a way that the larger the turbulence, the shorter the lifetime [41]. Actually, the turbulence in the wind cannot be controlled as it is an environmental factor, so for the purpose of this thesis a medium intensity of 15% corresponding to the IEC Class B winds is considered in order to generate the turbulent wind spectrum.

3.7. Wind Spectral Density

Turbulence can be also represented in the form of spectral density, which shows how the energy of the wind turbulence is distributed between different frequencies. The most commonly used spectra are the von Karman and Kaimal spectrum. In the context of this thesis and as it is suggested by the standards as well, the Kaimal spectrum is more suitable to model the atmospheric boundary layer and can be calculated by the following expression:

$$S_{Kaimal}(f) = \frac{\sigma_i^2 4L_v/U_w}{(1+6fL_v/U_w)^{5/3}} \tag{3.20}$$

where f is the frequency and L_v the integral length scale.

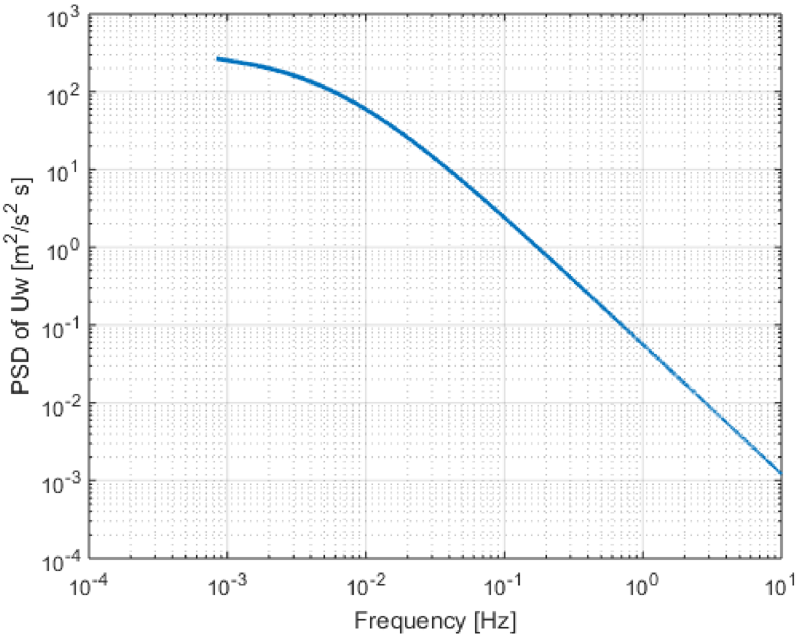

Figure 3.13: Kaimal Spectrum for mean wind speed equal to 11.06m/sec.

For each sea state, a realistic time series of turbulent wind speeds is generated from the theoretical spectrum. Figure 3.14 shows the times series for mean wind speed 11.06 m/s.

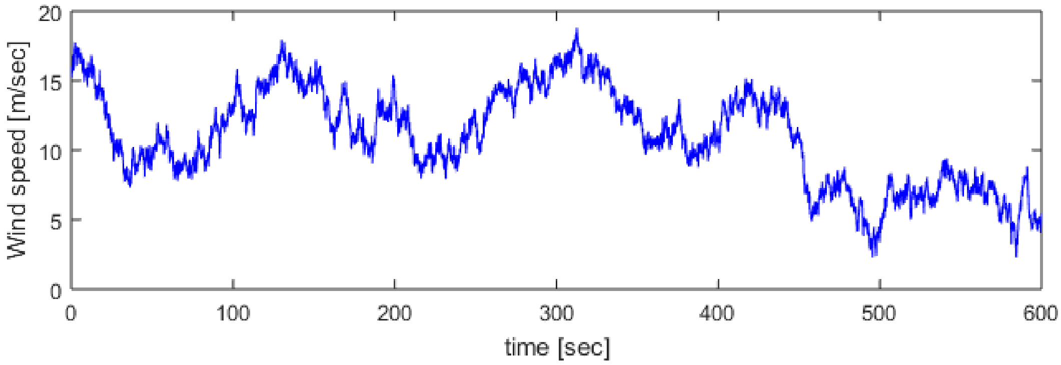

Figure 3.14: Wind Time Series for mean wind speed equal to 11.06m/sec.

For reasons of time economy, the wind speed history during the turbine's service life is reduced to 10 minute period for each mean wind speed, as it has already been referred. Moreover, in order to get a representative result for the wind speed time series, even for this short time period, many iterations are required. However, because this procedure is time consuming, here only one iteration has been considered for each one of the 18 cases of the mean wind speeds.

3.8. Thrust Force

The rotation of the wind turbine blades forms a circular area at the upper part of the tower and sudden decrease of air pressure at the top of the tower. Abrupt decline pressure causes the creation of a force in the direction of wind which is called thrust.

The thrust force on a wind turbine rotor due to wind can be estimated in a simplified manner by making use of the following expression:

$$F_{Thrust} = \frac{1}{2}\rho_{air} A_R C_T U_{rel}^2 \tag{3.21}$$

where ρ_{air} is the density of the air, A_R is the rotor swept area (πR^2) with R the radius of the rotor), C_T is the thrust coefficient and U is the wind speed which corresponds to specific Sea State at the level of rotor/nacelle.

Regarding the wind velocity, it is taken to be the relative velocity, $U_{rel} = U - \dot{x}$, thereby explicitly including the effect of the aerodynamic damping through the tower top velocity $\dot{x}$ [25]. This has been directly added in the wind speed time series generation in this case.

At this point it should be referred that the beam model presented in Section 3.3 has been used by adding an aerodynamic damping (4.0%).

4

Damage Equivalent Loads

In this chapter, detailed information about the calculation of damage equivalent loads, derived by MATLAB codes, due to wave and wind loading is displayed. Both step by step methodology used and the results are described in the following sections of this chapter.

4.1. Fatigue Assessment

As aforementioned, the fatigue damage is considered to be one of the design drivers for the wedge connection. As a result, extended information should be displayed concerning all relative data and basic theories that build up to that particular magnitude. More specifically, basically wind and wave are examined (current is not taken into account for the fatigue assessment) and further analyzed in order to formulate competent expressions for aerodynamic and hydrodynamic loading. Moreover, the concept of fatigue along with suitable S-N curves is presented and eventually result to the targeting Damage Equivalent Load and eventual fatigue damage.

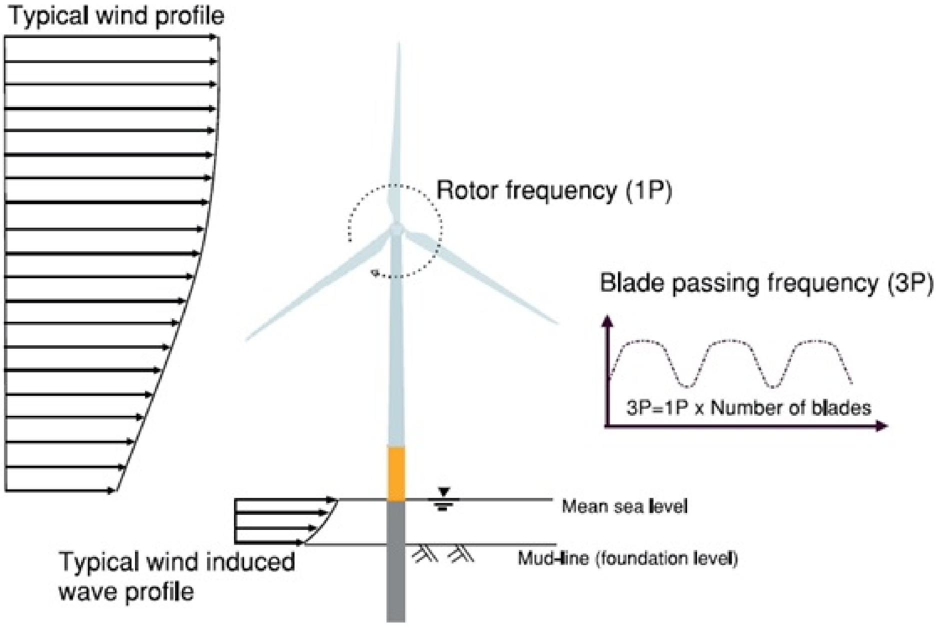
Typical wind profile
Rotor frequency (1P)
Blade passing frequency (3P)
3P=1P x Number of blades
Mean sea level
Mud-line (foundation level)
Typical wind induced wave profile

Figure 4.1: Load sources for a monopile-based offshore wind turbine [40]

4.2. Method Summary

To compute the expected fatigue life at the critical for our case location (level of wedge connection, +4m above MSL), the structure responses due to wind and wave loads are decoupled. Wave-induced fatigue is handled in the frequency domain, while the wind-induced fatigue is handled in the time-domain. Lifetime wind loading is approximately calculated by applying a rainflow counting algorithm to a time history of thrust loads and extrapolating the signal for the full structure life. The corresponding wave load response for each sea state is represented by a frequency-dependent structure response spectrum. In both cases, the lifetime response for each sea state may be expressed as a damage equivalent load (DEL).

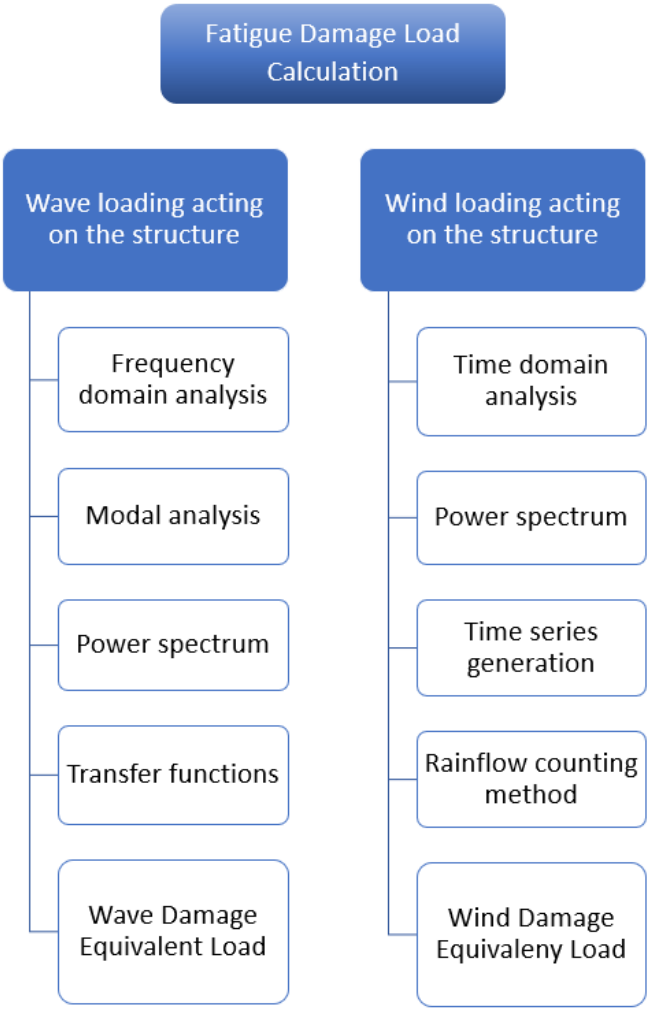
Fatigue Damage Load Calculation
Wave loading acting on the structure
Frequency domain analysis
Modal analysis
Power spectrum
Transfer functions
Wave Damage Equivalent Load
Wind loading acting on the structure
Time domain analysis
Power spectrum
Time series generation
Rainflow counting method
Wind Damage Equivaleny Load

Figure 4.2: Procedure for damage loads calculation

4.3. Time domain versus frequency domain approach

Time and frequency domain are the two most commonly used methods for the fatigue analysis [20].

- Time domain approach: generation of random time series from wind and wave spectra, non-linear, unsteady system simulation by time step integration techniques and Rainflow counting of stress ranges.

- Frequency domain approach: direct application of the environmental spectra, linear spectral analysis and determination of stress range distribution from spectral moments.

Actually, both air and water behave non-linearly with respect to the loading and response of the offshore wind energy converter. However the strongest non-linearity occurs in the rotor aerodynamics due to flow separation at higher wind speeds, while the non-linearity of hydrodynamic load is of lesser importance. For this reason, for the purpose of this thesis, frequency domain analysis has been selected for the wave loading, while time domain analysis has been used for the wind loading.

4.4. Equivalent Loads

The concept of equivalent loads has the ability to convert a long history of random fatigue loads to one number. As a consequence, an easier and more efficient comparison of numerous load cases is feasible. This concept introduces a fatigue damage equivalent load (or stress) which represents the load (or stress) with this constant amplitude that if applied to a material would cause the same damage as the random fatigue load cases [23]. The number of cycles that are used to derive the equivalent load are predefined: either explicitly (typically 10^7) or implicitly by considering a constant frequency (typically 1Hz) and a targeted lifetime as a time period.

4.5. Hydrodynamic Loading

Waves are efficiently described by the determination of amplitude and frequency. Wave amplitude is adequately expressed by the height of elevation in respect to mean sea level whereas the time intervals interceding between the passing of equal elevations from a reference point determine unique wave periods and therefore their respective frequencies. The latter is mainly defined by two terms in the respective literature, zero-crossing or peak period [26].

4.6. Frequency domain analysis - Wave DEL

Calculations in the frequency domain are a very powerful tool to compute wave induced response of offshore structures. According to M.Seidel [32], for the frequency domain approach the procedure described below should be followed:

1. Once the Mass and Stiffness Matrices have been determined by making the assumption of beam model, the natural frequencies ω_n, as well as, the mode shapes $\Phi_n(z)$ are derived. Having determined them, the modal stiffness K_n and the modal mass M_n are calculated for each mode.

$$M_n = \Phi^T \cdot M \cdot \Phi \tag{4.1}$$

$$K_n = \Phi^T \cdot K \cdot \Phi \tag{4.2}$$

2. Modal damping ratios are assigned to the individual modes. In this particular case, only the modal damping ratio for the first mode is of importance. The damping is defined as damping ratio ξ (percentage of critical damping). Alternatively, this can be expressed with the logarithmic decrement δ which relates to the damping ratio as δ=$2\pi\xi$ for small damping ratios. The total damping ratio is taken to be constant at 5.0% of critical damping, as structural damping of 1.0% and aerodynamic damping of 4.0% have been considered, as it is suggested by [15].

3. The Wave JONSWAP Spectrum $S_{\zeta\zeta}(\omega)$ is established for all sea states of relevance, as it has already been presented in previous section.

4. Transfer functions are determined:

- The hydrodynamic transfer function $H_{a,n}(\omega)$ is needed to determine the generalized wave forces dependent on wave frequency ω and mode considered.

  The hydrodynamic transfer function closely resembles the Morison Equation:

$$H_{a,n}(\omega) = \frac{1}{2}\rho\omega \int_0^d C_d \cdot D(z) \cdot \eta_o \cdot \Phi_0(z)dz + \rho\omega_0^2 \int_0^d C_{M(z)} \cdot \left[\pi \frac{D(z)^2}{4}\right] \cdot \eta_o \cdot \Phi_0(z)dz \quad (4.3)$$

  For monopiles, only the inertia term of Morison' s equation is considered, thus the drag term is neglected. The hydrodynamic transfer function is needed only for the first mode shape and it is written as follows:

$$H_{a,0} = \rho\omega_0^2 \int_0^d C_{M(z)} \cdot \left[\pi \frac{D(z)^2}{4}\right] \cdot \eta_o \cdot \Phi_0(z)dz \quad (4.4)$$

  The distribution function η_0 represents the decay in water particle acceleration with respect to depth (Figure 4.3) and is defined as follows for the wave frequency being equal to the first natural frequency:

$$\eta_0(z) = \frac{cosh(k_0(z+d))}{sinh(k_0 d)} \quad (4.5)$$

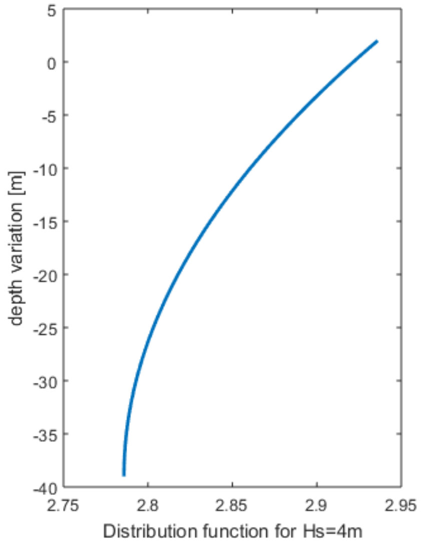

Figure 4.3: Distribution Function for H_s=4m

- The mechanical transfer function $H_n(\omega)$ is needed to determine structural displacements dependent on the mode considered.

  $H_n(\omega\ )$ computes the degree to which the applied loads may be amplified, as a function of wave forcing frequency ω , due to structure modal stiffness K_n and its natural frequency ω_n.

$$H_n(\omega) = \frac{1}{1-\left(\frac{\omega}{\omega_n}\right)^2 + 2 \cdot i \cdot \zeta_n \cdot \frac{\omega}{\omega_n}} K_n^{-1} \quad (4.6)$$

  As it is apparent in the formulation, $H_n(\omega)$ is maximized when the wave forcing frequency is either equal or very close to that of the structure modal frequency. This will result in a narrow-banded response spectrum, concentrated at the frequency where this amplification occurs (in this case $\omega = 1.4786 \frac{rad}{sec}$, see Figures 4.4 and 4.5).

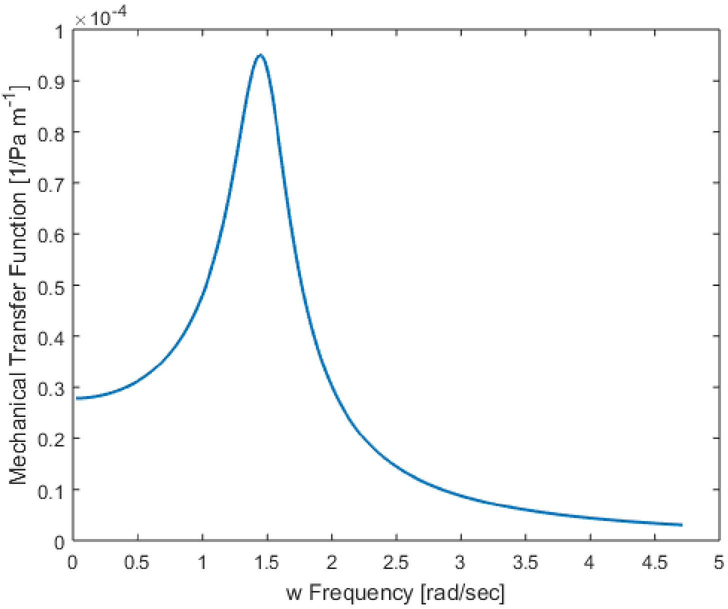

Figure 4.4: Lay-out of Mechanical Transfer function

The combined transfer function is defined as:

$$H(z,\omega) = \sum_{n=1}^{\infty} \Phi_n(z) \cdot H_n(\omega) \cdot H_{a,n}(\omega) \tag{4.7}$$

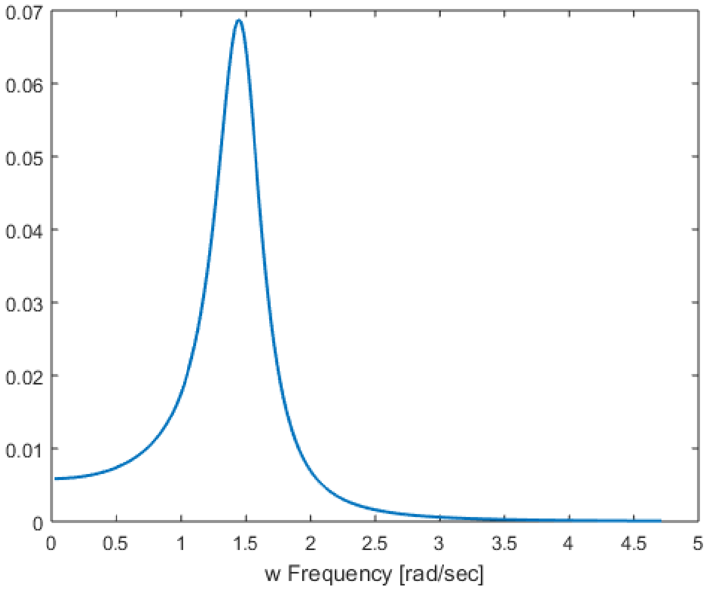

Figure 4.5: Transfer function at the level of wedge connection

Transfer functions can be generated to determine e.g. bending moments directly, rather than determining displacements first.

5. The response spectrum (e.g. displacements or bending moments at a specific elevation) is determined from the loading (wave) spectrum and the combined transfer function:

$$S_{uu}(z,\omega) = \left|H(z,\omega)\right|^2 \cdot S_{\zeta\zeta}(\omega) = \left|\sum_{n=1}^{\infty} \Phi_n(z) \cdot H_n(\omega) \cdot H_{a,n}(\omega)\right|^2 \cdot S_{\zeta\zeta}(\omega) \tag{4.8}$$

6. Extreme or fatigue loads are determined from the response spectrum by using the following formula:

$$\Delta M_{equiv} = 3.363\sigma_{M,wedge} \tag{4.9}$$

This is the damage equivalent moment ΔM_{eq} for the number of cycles given as:

$$N_{ref} = f_0 \cdot T \tag{4.10}$$

where $\sigma_{M,wedge}$ is the standard deviation of bending moments at the level of wedge connection and T is the time in seconds.

As it is obvious, the number of cycles depends on the natural frequency f_0 of the structure. The so called 1-Hz-DELs are usually used, where the number of reference cycles is defined as the number of seconds within the interval T:

$$N_{ref,1Hz} = T \tag{4.11}$$

The damage equivalent moment does need to be converted to take into account of the different number of cycles.Finally, the DEL can be converted considering the inverse slope of the S-N curve as follows:

$$\Delta M_{equiv,1Hz} = 3.363 \cdot \sigma_{M,wedge} \cdot \left(\frac{N_{ref}}{N_{ref\,1Hz}}\right)^{1/m} = 3.363 \cdot \sigma_{M,wedge}(f_0)^{1/m} \tag{4.12}$$

Thus $\Delta M_{equiv,1Hz}$ is independent of the intended service life.

4.7. Time domain analysis - Wind DEL

Wind-induced fatigue damage is obtained in the time domain due to the nonlinearities of the thrust loads on the rotor with respect to wind speed. This non-linearity can be presented in the figures below. In Figure 4.6 a time series of turbulent wind speeds produced by the Kaimal Spectrum for a mean wind speed equal to 11.06m/sec^2 and the corresponding thrust force are presented.

As it is obvious from Figure 4.6, for the thrust force time series, a ”plateau” appears at the points where the wind speed is higher than the nominal wind turbine speed (12.5 m/sec), as this is the speed at which the turbine operates at its optimum efficiency and the thrust of the rotor takes its maximum value.

When the rotor is operating in its rated condition, an increase in wind speed no longer corresponds to the increase in the thrust loads on the rotor. This non-linearity works in the opposite direction in this case. Thus, at speeds above the cut-out wind speed, the turbine will enter an idling condition and an increase in wind speed then results in a decrease in the thrust at the rotor. This phenomenon can be seen in the Figure 4.7.

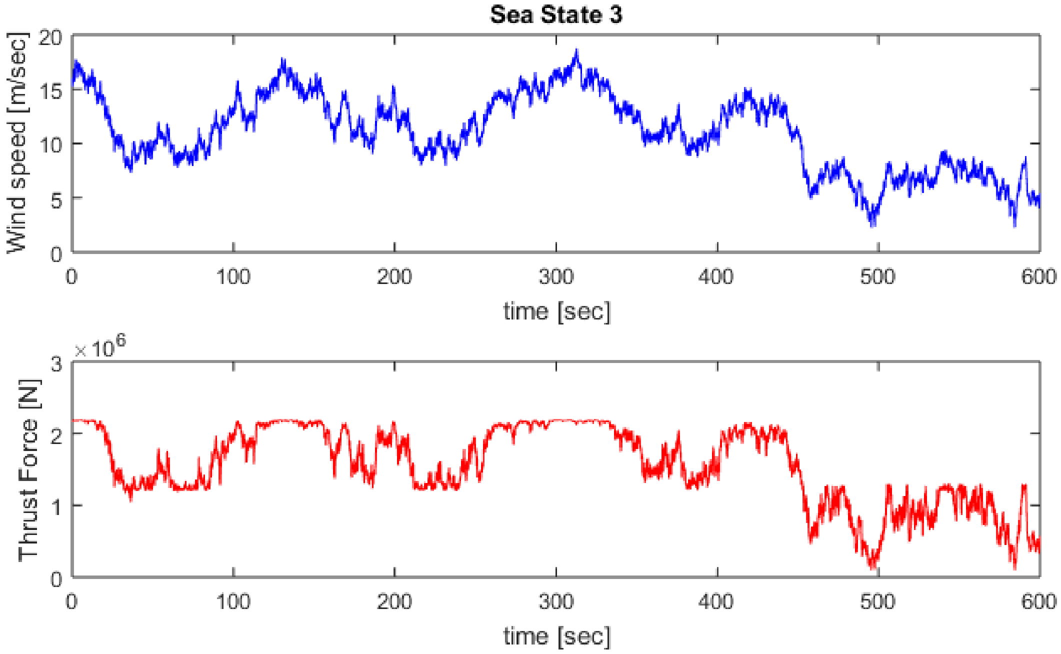

Figure 4.6: Wind and corresponding thrust force time series for mean wind speed equal to 11.06 m/sec (SS 2)

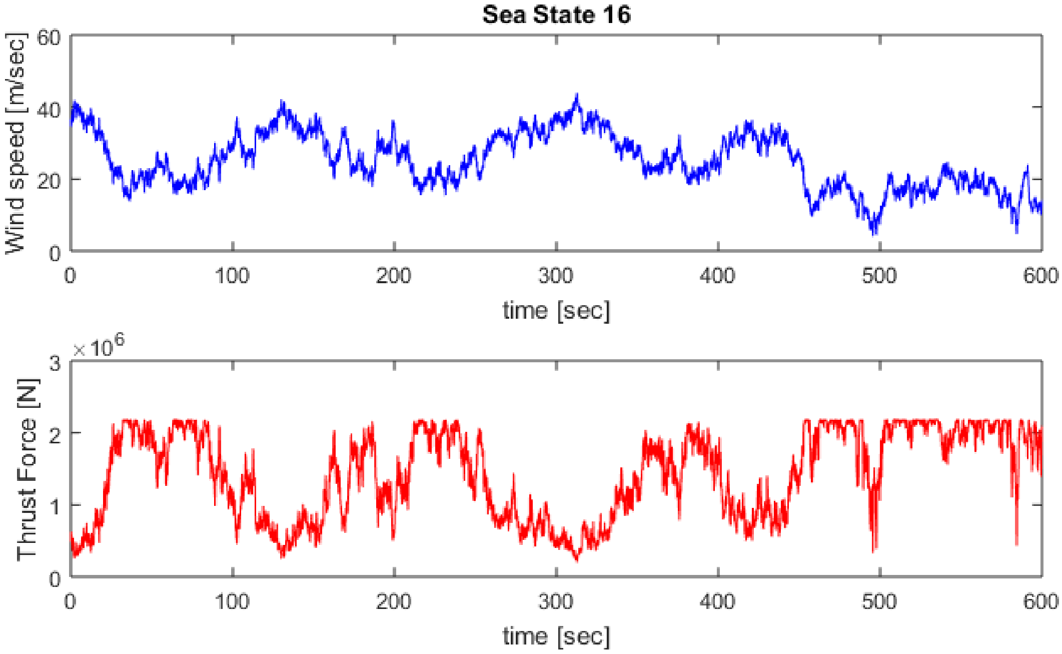

Figure 4.7: Wind and corresponding thrust force time series for mean wind speed equal to 25.09 m/sec (SS 16)

4.7.1. Equivalent Stresses & Rainflow Counting Method

To translate the above time histories of thrust loading to moment time series at the level of the wedge connection, the assumption that the structure is completely rigid has been made. Thus, in order to convert the thrust loading to moments, they are multiplied by the distance between the rotor level and the considered level of the wedge connection ($148 - 44 = 104m$). In their turn, the derived moments are converted to equivalent stresses.

$$\sigma = \frac{M \cdot D}{2 \cdot I} \tag{4.13}$$

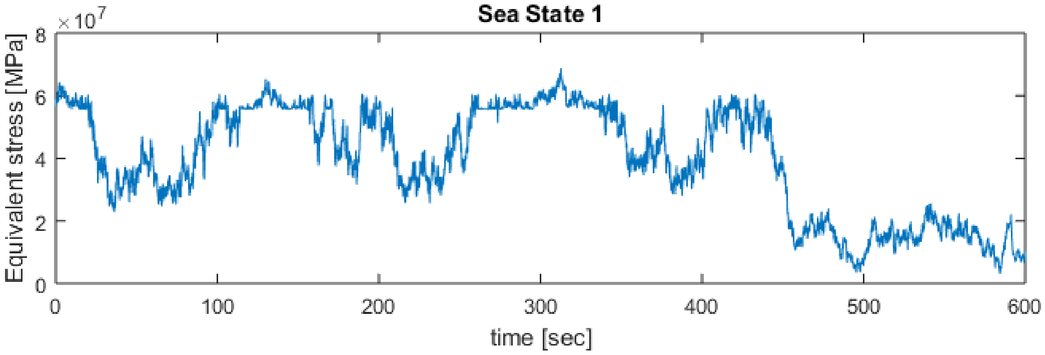

Figure 4.8: Equivalent stress time series for mean wind speed equal to 6.30m/sec (SS 1)

Once the equivalent stresses have been derived, the rainflow cycling method is applied for the period of 10 minutes for each one of the eighteen cases. To translate the static loads to dynamic stresses, the above stresses are multiplied by a dynamic amplification factor, in order to account for both the structural and the aerodynamic damping. Thus, after that, a rainflow counting MATLAB algorithm converts the given stress signal (equivalent stress time history) into turning points. Through these turning points, the algorithm extracts the number of cycles from each load case history, and by choosing a number of bins, several counting cycles with different amplitudes and mean values are obtained.

Figure 4.9 shows the resulting rainflow histogram derived by the stress signal given in Figure 4.8 and the 30-bin histogram representing the number of cycles of occurrence of each stress range obtained by the rainflow method.

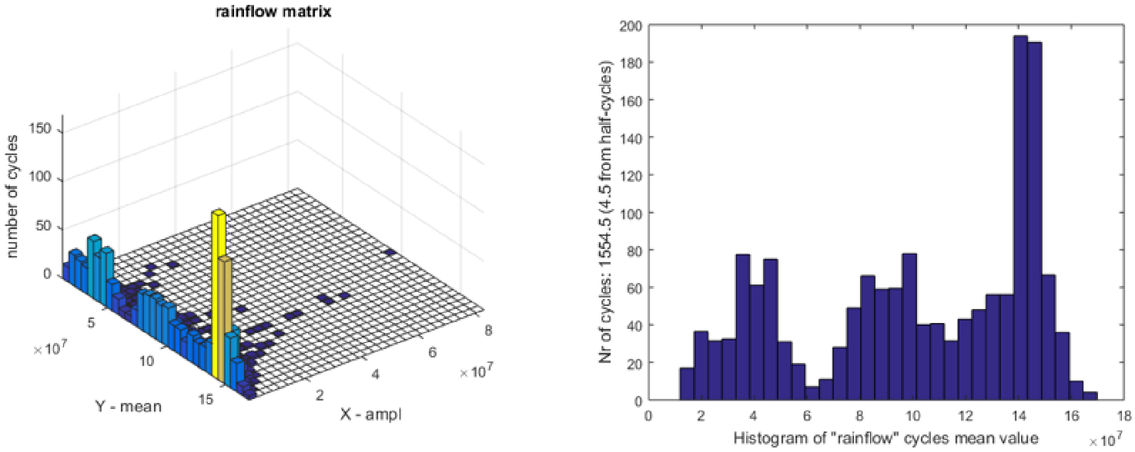

Figure 4.9: Rainflow count histogram of equivalent stress time series (SS 1).

To calculate the damage equivalent stresses for each case, a reference number of cycles should be determined (10^7 is selected in this case). The equation through which these stresses are derived is given by:

$$\Delta\sigma_{equiv} = \left(\frac{1}{N_{equiv}} \sum n_i \Delta\sigma_i^m \right)^{1/m} \tag{4.14}$$

where,

$\Delta\sigma_{equiv}$ is the equivalent stress,
N_{equiv} is the predefined equivalent number of cycles (10^7),
$\Delta\sigma_i^m$ is the stress range of each bin,
n_i is the number of cycles of each bin.

The above resulting damage equivalent stresses refer to the period of 10 minutes.To calculate the equivalent stress that corresponds to the whole life-time of the selected wind turbine, the above equivalent stresses should be multiplied by the ratio of the amount of seconds in the period of 25 years ($60_{seconds/minute} \cdot 60_{minutes/hour} \cdot 24_{hours/day} \cdot 365_{days/year} \cdot 25_{years}$) over the simulation period of 600 seconds (10 minutes).

$$\Delta\sigma_{equiv} = \left(\frac{1}{N_{equiv}} \sum n_i \Delta\sigma_i^m \cdot \frac{T_{TotalLife}}{T_{simulation}}\right)^{1/m} \tag{4.15}$$

4.8. Results of Damage Loads

In the next Tables, the results of equivalent damage loads for both waves and winds are shown for the eighteen different cases:

Case	Wave DEM (1% damping) [MNm]	Wave DEM (5% damping) [MNm]	Number of Cycles for waves
1	0	0	10305098
2	0	0	59092332
3	0	0	30269367
4	0	0	5779211
5	0	0	1326349
6	0	0	345151
7	0	0	96626
8	25.9221	11.5927	28093
9	26.4493	11.8285	8322
10	52.2405	23.3627	2498
11	54.0957	24.1924	762
12	81.2182	36.3219	238
13	82.9258	37.0855	76
14	111.2330	49.7449	25
15	114.2577	51.0976	8
16	142.4578	63.7091	3
17	145.2316	64.9495	1
18	165.4502	73.9916	0.5

Table 4.1: Damage Equivalent Moment for wave loading.

Having a look on both the tables, the contribution of wave loading is of less importance compared to wind loading; this results both from the magnitude of the resulting loads and the number of cycles of each one. However, both loading will be taken into account for the fatigue assessment of the wedge connection.

Furthermore, for the damage equivalent loads due to waves, results with and without including the aerodynamic damping have been exported, in order to understand its contribution to the magnitude of the loads. Despite the fact that the damage loads including only the structural damping are higher, for the damage estimation of the connection in the following sections, only the damage loads with damping 5.0% are taken into account, as this case responds better to the reality.

Case	**Wind DEM at 10^7 cycles and m=4 [MNm]**
1	72.6154
2	93.3811
3	160.1978
4	151.0488
5	169.9048
6	118.1763
7	120.2189
8	80.2209
9	128.2035
10	149.9772
11	72.6154
12	203.0044
13	196.7845
14	202.1068
15	212.5338
16	214.9922
17	219.7594
18	230.4379

Table 4.2: Damage Equivalent Moment for wind loading.

At this point it should be also referred that, due to limited amount of information for the environmental data, the fact that both the wind and wave come from different directions is not taken into account; instead, it is assumed that all the winds and waves are coming from the same direction (for example from the North). This procedure may result in over-prediction of tower loads.

Last, regarding the wind damage loads, the probability of occurrence resulted by the Weibull distribution function has not been taken into account for their calculation. The probability of occurrence of each wind speed (Sea State) is directly taken into account on the damage estimation, as it will be presented in Chapter 6, where the FE analysis and the fatigue assessment of the connection take place.

5

Modeling of Wedge Connection in ANSYS

An advanced Finite Element Analysis will be used in order to predict the performance of the wedge connection against fatigue and see how the presence of preload influences the fatigue life of each one of the components.

First, the 3D CAD design software of SOLIDWORKS is used to design each component of the wedge connection (MP flange, TP flange, dowels and bushings) and assemble them in their final position (Figure 5.1). Then, the software ANSYS WORKBENCH is used for the fatigue simulation.

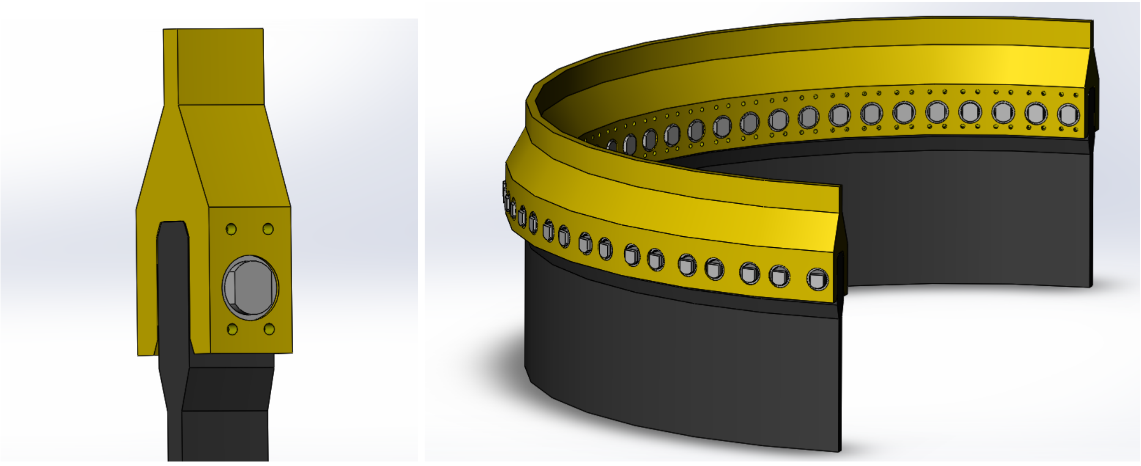

Figure 5.1: Wedge Connection model designed in SOLIDWORKS

At this point it should be noticed that, in order to analyze the behavior of a wedge connection in a real tower, a full scale tower connection model has been built, based on the characteristics of the given turbine (monopile diameter 6.5m).

In ANSYS WORKBENCH software, there are three steps for the finite element analysis of the connection :

1. Pre-processing: After modeling of the joint in SOLIDWORKS and importing to ANSYS WORKBENCH, meshing is carried out.
2. Processing: After pre-processing, loads and boundary conditions are applied.

3. Post-processing: After successfully completed the above process, the results can be viewed.

5.1. Material Properties

After inserting the geometry of the model, of great importance for the accuracy of the results of the analyses are the material properties of the members of the connection.

In this case the following material properties have been used for each component of the connection:

- For both MP and TP flange structural steel has been used (E=210GPa).
- For the dowels structural steel has been used as well, with yield stress and ultimate stress (E=210GPa).
- FRP material has been selected for the bushings with yield stress equal to and Young's Modulus of Elasticity equal to E=2.8GPa.

5.2. Meshing

Ansys Meshing is automatically integrated with each solver within Ansys Workbench environment. More specifically, Ansys Meshing chooses the most appropriate options based on the analysis type and the geometry model [28].

The default mesh, that the ANSYS uses, produces a mesh that is adequate for the analyzed model. Thus, the model is meshed by using SOLID187 element type for MP, TP flanges and dowels, while SOLID186 is used for the bushings [31].

SOLID187 element is a higher order 3D, 10-node element. It has a quadratic displacement behavior and is well suited to modeling irregular meshes. The element is defined by 10 nodes having three degrees of freedom at each node: translation in the nodal x, y and z directions. The element has plasticity, hyperplasticity, creep, stress stiffening, large deflection and large strain capabilities. It also has a mixed formulation capability of simulating deformations of nearly incompressible elastoplastic materials and fully incompressible hyperelastic materials [31].

SOLID186 element, whose shape presented in the figure below, has exactly the same characteristics with SOLID187 element. The only difference is that the element is defined by 20 nodes.

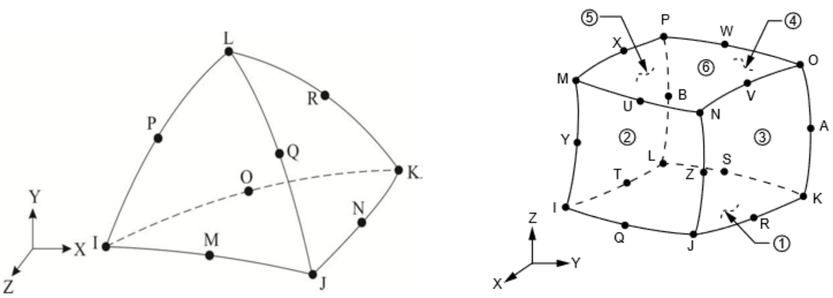

Figure 5.2: Solid187 element on the left and SOLID186 element on the right [31].

Figure 5.3 illustrates the mesh of the different parts of the wedge connection. The mesh of the MP flange, TP flange and dowel is made my SOLID187 elements, while for the mesh of bushings SOLID186 elements have been used.

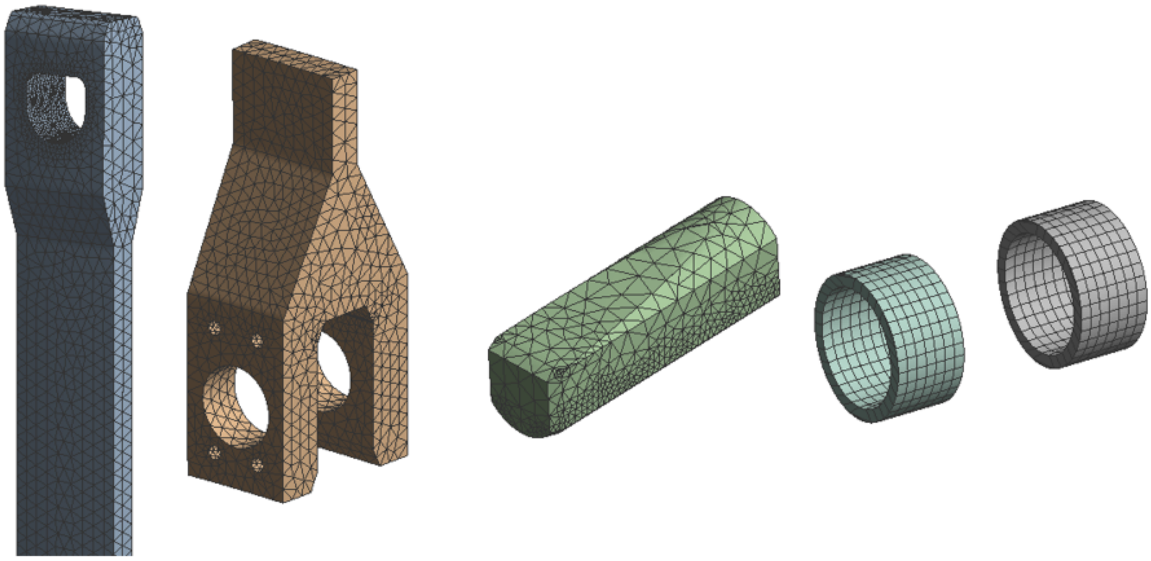

Figure 5.3: Meshed parts of wedge connection.

5.3. Contact Elements

When two separate surfaces touch each other such that they behave mutually tangent, they are said to be in contact [4].

In order to apply contact elements, it is necessary to choose among one of the following types of contact:

1. Bonded: If contact regions are bonded, then no sliding or separation between faces or edges is allowed. Think of the region as glued. This type of contact allows for a linear solution since the contact length/area will not change during the application of the load.
2. No separation: This contact setting is similar to the bonded case. It only applies to regions of faces or edges. Separation of the geometries in contact is not allowed.
3. Frictionless: This setting models standard unilateral contact; normal pressure equals to zero if separation occurs. This solution is nonlinear because the contact area may change as the load is applied. A zero friction coefficient is assumed, to allow free sliding.
4. Rough: Similar to the frictionless setting, it models perfectly rough frictional contact where there is no sliding and corresponds to an infinite friction coefficient between the contacting bodies.
5. Frictional: The two contacting geometries can carry shear stresses up to a certain magnitude across their interface before they start sliding relative to each other. The model defines an equivalent shear stress at which sliding on the geometry begins as a fraction of the contact pressure. Once the shear stress is exceeded, the two geometries will slide relative to each other. The coefficient of friction can be any nonnegative value.

Thus according to the above classification, the most appropriate contact type, for the current model of the segment connection, is the frictional contact between the MP and TP flanges, and between the MP flange and the dowel, while bonded contact is applied between the bushings and TP flanges.

The values of friction coefficient that have been used between the contact areas are:

- μ= 0.2 between the MP and TP flanges.
- μ=0.1 between the MP flange and the dowels.
- μ=0.05 between the dowels and the bushings.

One more important step in the contact analysis is the determination of contact and target surfaces. Contact elements are constraint against penetrating the target surface, while target elements can penetrate through the contact surface. For rigid-to-flexible contact,the target surface is always the rigid surface and the contact surface is the deformable. For flexible-to-flexible contact, the choice of which surface is designed contact or target can cause a different amount of penetration and affect the solution accuracy. Generally, if one surface is stiffer than the other one, the softer should be the contact, while the stiffer should be the target.

There are four contact algorithms that are available in ANSYS:

1. Pure Penalty Method,
2. Augmented Lagrange,
3. Normal Lagrange,
4. Multi-point constraint (or MPC).

The Augmented Lagrange method is selected for this problem. This method is recommended for general frictionless or frictional contact in large-deformation problems. In the Augmented Lagrange method, the calculated force at the contact detection points is given by the following expression:

$$F_c = k_c D_p + \lambda \tag{5.1}$$

where,
k_c is the contact stiffness,
D_p is the penetration at the contact element,
λ is an internally calculated term that makes the method less sensitive to contact stiffness.

It should be referred that the higher the contact stiffness is, the lower the penetration.

5.4. Boundary Conditions

At the bottom of the MP flange, a fixed boundary condition has been applied in order to prevent free movement of the solid bodies. The other two parts of the connection's segment, the dowel and the TP flange, are constrained only by the contact areas.

ANSYS WORKBENCH Mechanical supports cyclic symmetry analysis, thus by inserting an appropriate cylindrical coordinate system and indicating a low and high boundary condition on opposite side faces on the body (left and right side of the segment in this case), the full ring stiffness can be simulated. With this type of symmetry, the results at the end of the analysis can be also represented in the whole section, which means that a full scale tower connection model is generated with 78 wedges.

5.5. Loading

For the fatigue assessment of the wedge connection, two load cases are examined:

1. In the first case only one load step is determined in which the Damage Equivalent Loads for each case, calculated in previous chapter, are applied. More specifically, having calculated the damage moment for each Sea State, the equivalent force for each segment, acting on the top of it, is calculated by:

$$F_{segment} = \frac{DEM}{W_{tower}} A_{segment} \tag{5.2}$$

2. In the second load case, two loading steps are defined for the analysis of the model:
    - The first step is to apply increasing pressure until a certain value at the back side of the dowel which actually creates a pretension that is necessary to clamp together the two flanges, create a frictional lock between them and reduce the effects of cycling loading on the members.
    - The second step is to apply the external loading for the fatigue analysis, same as in the first load case.

   Summing up, the first step mimics the assembly of the model (for the final positioning of the dowel) and the second one the real behavior of the model under real loading.

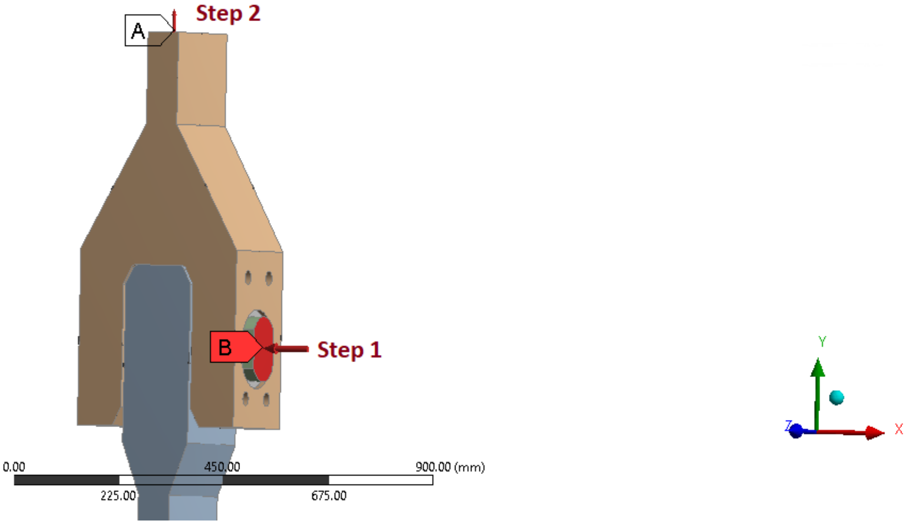

Figure 5.4: Load steps.

6

Finite Element Analysis & Fatigue Assessment

To facilitate the design process, the three dimensional flange connection is reduced to a single wedge connection and width equivalent to the arc length between the dowels' holes, by dividing it into n_w segments (n_w =the number of wedges/dowels, 78 in this case). For the FEA, the segment where the highest stresses are developed is taken into account, in which only the tensile axial loads on TP flange resulting from the damage equivalent moments of the tower at the level where the wedge connection is located are assumed to act on it (Equation 5.2).

Thus, once the damage equivalent loads have been calculated and the finite element model has been properly built, the procedure of simulations is taking place. Each one of the load cases (18 loads for each case for both wind and wave loading –> 36 load cases) is studied for the following two different cases:

- with preloading,
- without preloading.

The selection of the ”most” suitable S-N curves for the fatigue assessment of the connection will be based on the results of the experiments that have been carried out for this geometry of the connection.

6.1. Load Sharing

Before starting to describe the procedure that will be followed for the fatigue assessment of the wedge connection and represent/discuss the results of it, some details related to the way that the acting axial tensile load is distributed on the different members/parts of the connection will be first represented.

6.1.1. Non-preloading case

The acting axial load on the top of the segment is transferred through the shell (top of the TP) to the bottom part of the TP flange, and through the bushings and the dowel this load in transferred on the MP flange. This procedure is illustrated in Figure 6.1.

6.1.2. Preloading case

In case where preload takes place, the wedge connection can be considered as a system with two parallel springs, each one having its own different stiffness.

- k_1 : relative stiff spring in compression which represents the stiffness of the MP flange (top part above the hole).

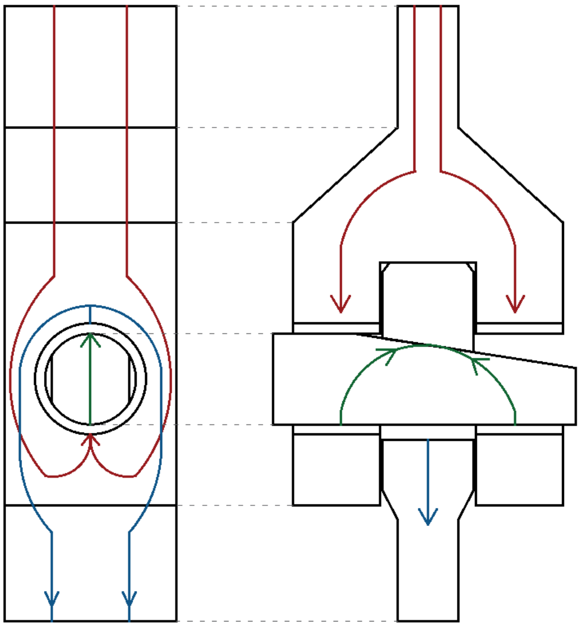

Figure 6.1: Load sharing (distribution) on wedge connection.

- k_2 : more flexible spring that represents the stiffness of the other parts of the connection (TP flange, dowel, bushings). Only one stiffness is calculated for these parts because they have been represented as springs in series.

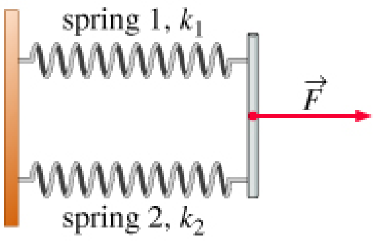

Figure 6.2: Equivalent spring system.

As it has already been described in the first chapter of this thesis report, the inclined plane of the wedge/dowel will transform the horizontal applied load (pressure) on it (load of step 1) into a vertical reaction/preload between the contact planes of the two flanges. The external load which is applied on the top of the segment (load of step 2) will either increase or decrease this contact load dependent on its direction.

To calculate the stiffness of each spring, two models presented in Figures 6.3 and 6.4 have been used. So, by using appropriate boundary conditions in both models and applying the same load (2MN) the displacement is measured. (The load is applied on faces, not on a specific point.)

Thus, for the stiffness of the MP flange, the displacement of the top part above the hole where the force is applied is equal $0.05762mm$, resulting to stiffness $k_1 = \frac{F_1}{x_1} = 34.713MN/mm$, while

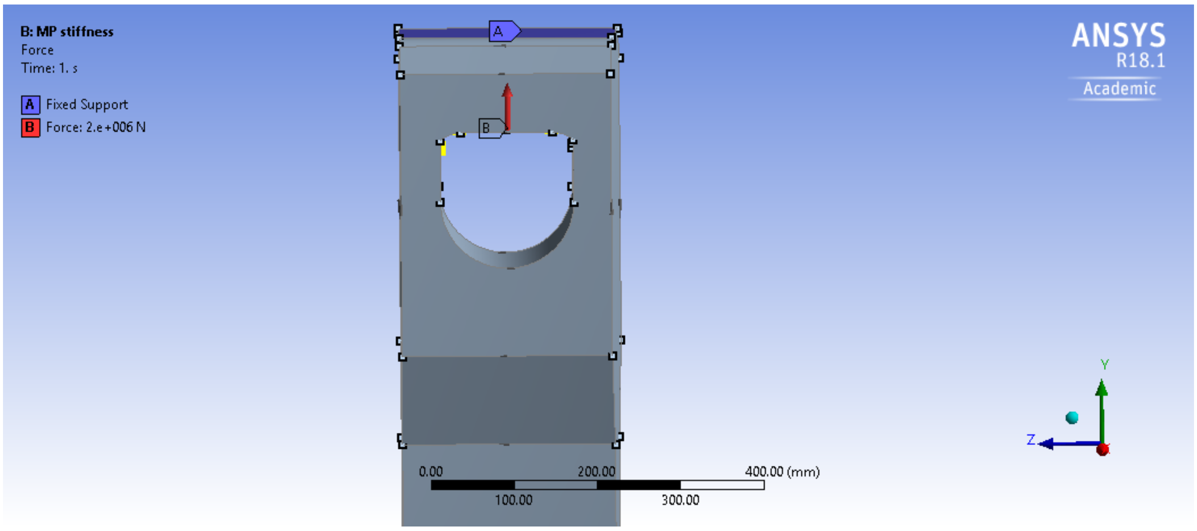
B: MP stiffness
Force
Time: 1. s
A Fixed Support
B Force: 2.e+006 N
A
B
ANSYS
R18.1
Academic
0.00
200.00
400.00 (mm)
100.00
300.00
Y
Z

Figure 6.3: Model A: Stiffness calculation of MP flange.

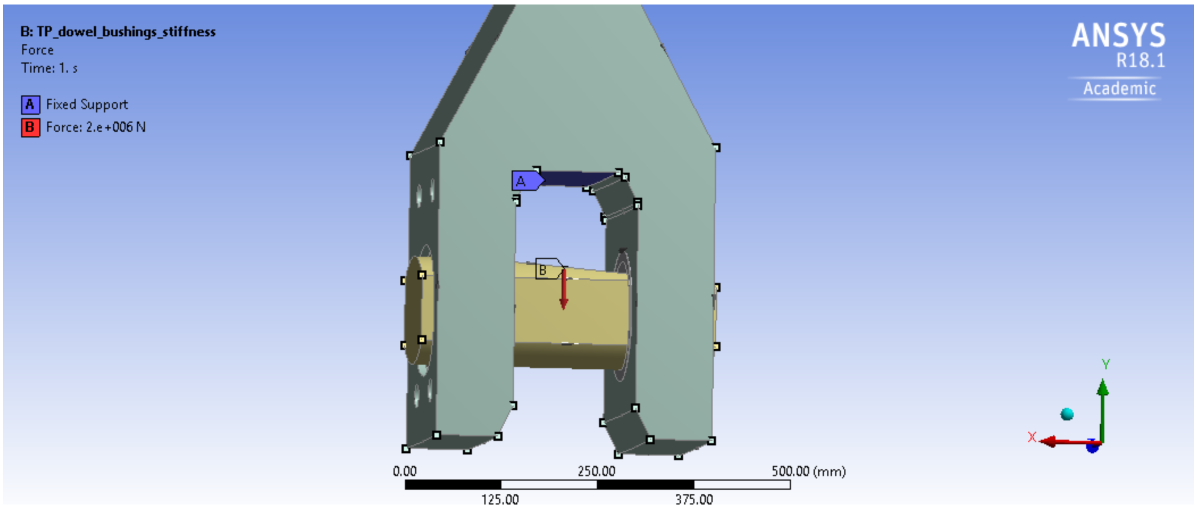
B: TP_dowel_bushings_stiffness
Force
Time: 1. s
A Fixed Support
B Force: 2.e+006 N
A
B
ANSYS
R18.1
Academic
0.00
250.00
500.00 (mm)
125.00
375.00
Y
X

Figure 6.4: Model B: Stiffness calculation of TP flange, dowel and bushings.

for the other parts of the connection the displacement at the middle of the inclined plane of the dowel is $1.4769 mm$ which results to stiffness $k_2 = 1.354 MN/mm$ (Figure 6.5).

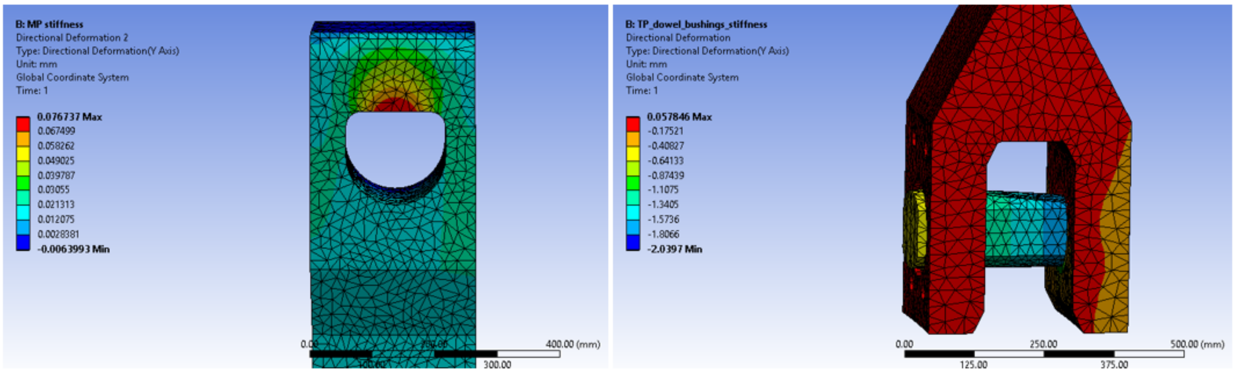
B: MP stiffness
Directional Deformation 2
Type: Directional Deformation(Y Axis)
Unit: mm
Global Coordinate System
Time: 1
0.076737 Max
0.067499
0.058262
0.049025
0.039787
0.03055
0.021313
0.012075
0.0028381
-0.0063993 Min
400.00 (mm)
300.00
B: TP_dowel_bushings_stiffness
Directional Deformation
Type: Directional Deformation(Y Axis)
Unit: mm
Global Coordinate System
Time: 1
0.057846 Max
-0.17521
-0.40827
-0.64133
-0.87439
-1.1075
-1.3405
-1.5736
-1.8066
-2.0397 Min
0.00
250.00
500.00 (mm)
125.00
375.00

Figure 6.5: Left: Total deformation of Model A (MP flange), Right: Total deformation of Model B (TP flange, dowel and bushings).

The load change/sharing of both the springs is proportional to their individual stiffness. So, from the above calculations, it results that the MP flange is the member of the connection which is actually carrying most of the external force due to its higher stiffness, assuming that there is no separation between the two flanges. This is also clear in the following expressions and in the graph presented in Figure 6.6, where:

- $F_{tensile}$: is the external load applied on the top of the segment,
- δ_{MP}: is the change on length on Model A due to $F_{tensile}$,
- δ_{dowel}: is the change on length on Model B due to $F_{tensile}$.

As long as there is no separation between the two flanges, the displacements (change on length) should be equal, $\delta_{MP} = \delta_{dowel} = \delta$. The change on the force for each part when the external load is applied is given by the following expressions:

$$\Delta F_{MP} = K_{MP} \cdot \delta_{MP} \tag{6.1}$$

$$\Delta F_{dowel} = K_{dowel} \cdot \delta_{dowel} \tag{6.2}$$

But the summation of these two forces should be equal to the applied tensile load:

$$F_{tensile} = \Delta F_{MP} + \Delta F_{dowel} = K_{MP} \cdot \delta_{MP} + K_{dowel} \cdot \delta_{dowel} = (K_{MP} + K_{dowel}) \cdot \delta \tag{6.3}$$

so,

$$\delta = \frac{F_{tensile}}{K_{MP} + K_{dowel}} \tag{6.4}$$

$$\Delta F_{MP} = F_{tensile} \frac{K_{MP}}{K_{MP} + K_{dowel}} \tag{6.5}$$

$$\Delta F_{dowel} = F_{tensile} \frac{K_{dowel}}{K_{MP} + K_{dowel}} \tag{6.6}$$

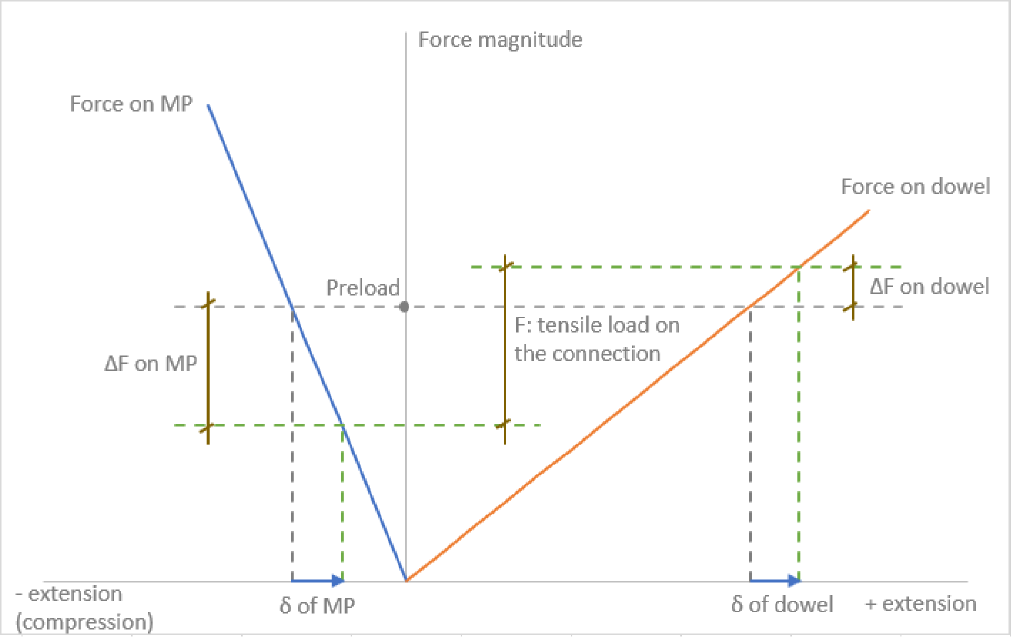
Force magnitude
Force on MP
Force on dowel
Preload
ΔF on dowel
F: tensile load on the connection
ΔF on MP
- extension (compression)
δ of MP
δ of dowel
+ extension

Figure 6.6: Force sharing on the wedge connection

So, similar to the bolted connection, the external load will be shared between the MP flange load path and the load path through the TP flange, bushings and dowel. Due to its greater stiffness, the MP load path will absorb most of the external load until the two flanges are separated. The external load is completely absorbed by the TP flange, bushings and dowel load path upon flange separation ("gaping").

6.2. Loads developed on MP flange

In the Figure 6.7, the loads/reaction forces developed on the MP flange after the preloading step (left) and when the tensile load is applied on the top of the segment (right) are presented. What is obviously illustrated is that while the tensile load is applied, the contact force that has been created between the two flanges during the preloading step is reduced. Thus, when the tensile load will exceed the preload, the contact between the two flanges will not exist any more.

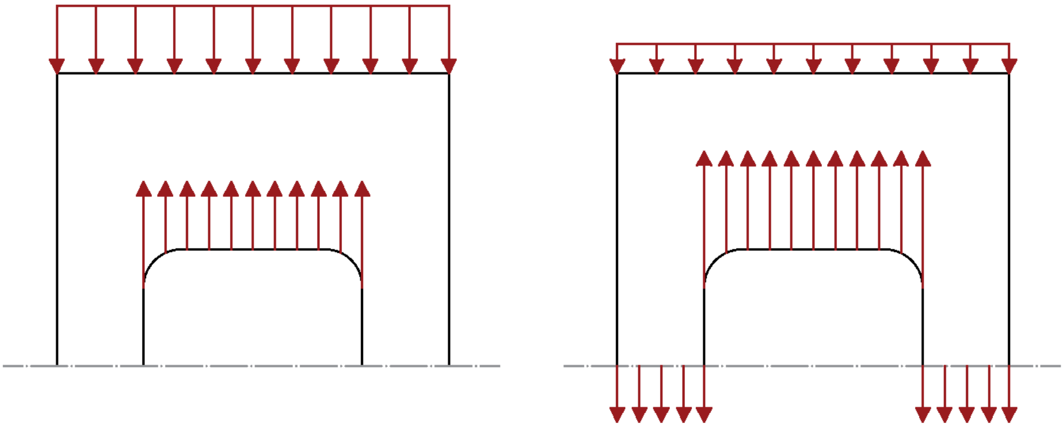

Figure 6.7: Preload MP flange (left) subjected to tensile load (right).

6.3. Determination of S-N curves

Fatigue tests are focused on the nominal stress required to cause a fatigue failure under a certain number of cycles. These tests results in data presented as a plot of stress ranges against the number of cycles until failure (S-N curve). The objective of a fatigue test is generally speaking to determine the fatigue life and/or the damage point (i.e. the location of failure of a test-piece subjected to a prescribed sequence of stress amplitude).

Generally, in order to find the S-N curve that corresponds/refers to a specific material (segment), a series of fatigue tests should be made on an adequate number of specimens of the material at different stress levels. The more the specimens that are used for the fatigue assessment of it, the better the accuracy of the resulting S-N curve.

In many applications, the behavior of a component in service is influenced by several other factors besides the properties of the material used in manufacture. This is particularly true for the cases where the component or structure is subjected to fatigue loading, since the fatigue resistance can be greatly influenced by the service environment, the surface conditions of the part, the method of fabrication, the design details, etc. Thus, as the fatigue properties of a material can be easily influenced by many factors, the S-N curve obtained by laboratory tests has to be related to the real life design conditions. This can be achieved by modifying it, and more specifically reduce it, in order to correspond as better as it is possible to the real model.

Up until now, several S-N curves have been plotted and used in Engineering Codes (Eurocode, DNV-GL, etc.), referred to specific construction details which are commonly used in civil engineering structures for the assessment of fatigue resistance of members, connections and joints subjected to fatigue loading. However, while the civil engineering domain is growing rapidly, the need of the evaluation of the available curves or the need to carry out new fatigue tests for the development of new S-N curves is created, as none of the existing construction details can fully represent the new ones. This is also happened in case of the wedge connection, which is an innovative connection and behaves in completely different way compared to the conventional ones that are used until now in the wind industry.

Thus, in order to have an approximate view of how the wedge connection behaves under fatigue loading, tests have been carried out in the Stevin II Laboratory of TU Delft. These tests have been performed for only one segment of the connection, which has been scaled down approximately three times compared to the real one and is not curved. According to DNV-GL-RP-C203 [10], for new types of connection it is recommended to perform testing of at least 15 specimens in order to establish a new S-N curve. At least three different stress ranges should be selected in the relevant S-N curve such that a representative slope of the S-N curve can be determined. However, for the current geometry of the wedge connection, due to the limited amount of fatigue tests (only one specimen), the goal of this test is not to establish a new S-N curve but based on this test result to select these existing S-N curves that better match to this connection.

6.4. Test results & Selection of S-N curve

In the Figure 6.8 below, the segment of the wedge connection that has been tested is represented.

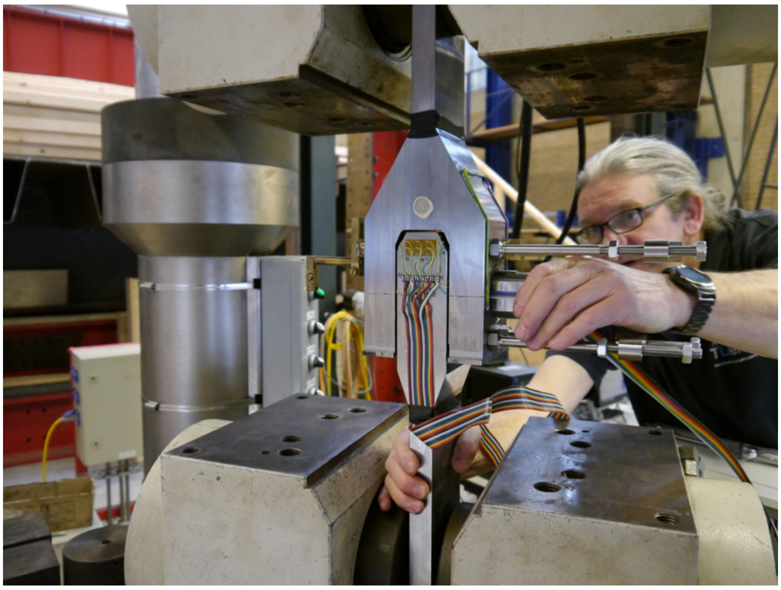

Figure 6.8: Tested segment of wedge connection under fatigue loading.

For this test, cyclic load with range has been applied on the segment. Nominal stresses of range $\Delta\sigma = 121MPa$ are appeared on the top of the flanges. However, due to an unrelated incident (fire exposure at the laboratory , test procedure), the test was interrupted at million cycles. So, as there was no accurate result for the selection of the S-N curve, an assumption that for this stress range the failure occurs at million cycles has been made.

In Appendix F.7 of DNV-GL-RP-C203 [10], a method is proposed for the qualification of new S-N curves based on fatigue test data. This method can be used to statistically compare test results to the reference curves. So, for this single point resulted from the test, it is assumed that a line/curve passes through it with slope equal to m=4, same as the slope of B1 curve (and most of the existing curves) from DNV-GL-RP-C203.

$$loga = log(N_{test}) + m \cdot log(\Delta\sigma_{test}) \tag{6.7}$$

So, according to DNV-GL standards [10], a design S-N curve should provide a 97.7% probability of survival where the mean curve is determined with 75% confidence. More specifically, the statistical uncertainty in fatigue test data shall be accounted for when a limited number of tests is performed to design S-N curves, and it is required that the design curve is estimated with at least 75% confidence.

So, to correct for statistical uncertainty due to limited number of tests, the following reduction is proposed for the curve resulted from the test:

$$log\bar{a} = loga - c \cdot S_{log(N)} \tag{6.8}$$

where, $S_{log(N)}$ is the standard deviation of the test data in logN axis and c is a factor that depends on the amount of the test data.

Of course, in our case the standard deviation is zero, but in order to be more ”conservative”, based on data resulted from experiments of three segments for a new different geometry of the wedge connection, the standard deviation has been taken equal to $S_{log(N)} = 0.172$ and $c = 3.78$ for the required confidence of 75% based on Table F.3 [10]. Thus, by substituting the standard deviation and the c factor, the mean intercept is now equal to:

$$log\bar{a} = \tag{6.9}$$

In Figure 6.9, the resulting curve from the experiment based on the assumptions that have been already referred above, and some of the S-N curves from both DNV-GL and Eurocode 3 which match better to this connection have been plotted.

Figure 6.9: S-N curves.

For the S-N curves that have been plotted, the B1 curve is suitable for simple plain steel specimens while the other three curves are based on test specimens for the fatigue assessment of double plate shear bolted connections which is the one that most closely resemble the wedge connection. More details about the selection of the S-N curves for each part and for each load case are given in the following section.

6.5. Fatigue assessment of the wedge connection

6.5.1. Fatigue assessment of the two flanges

First the damage and the fatigue life of the flanges are calculated based on the S-N curves presented in Figure 6.10. At this point, it should be referred that on the tested specimen of the connection, preload has been applied. So, for their fatigue assessment with and without preload the detail categories $\Delta\sigma_c = 112MPa$ and $\Delta\sigma_c = 90MPa$ have been used respectively, same as in case of double plated shear bolted connections according to Eurocode 3 Part 1-9 (Figure 6.11) [1]. At this point it should be referred that, if the test resulted point was below the selected S-N curves, the fatigue assessment of the connection should be based on other curves.

Figure 6.10: S-N curves used for the flanges (wind damage load).

Through the selected S-N curves, the allowable number of cycles and the damage based on Palmgren-Miner rule are calculated for each one of the 18 load cases. The total damage

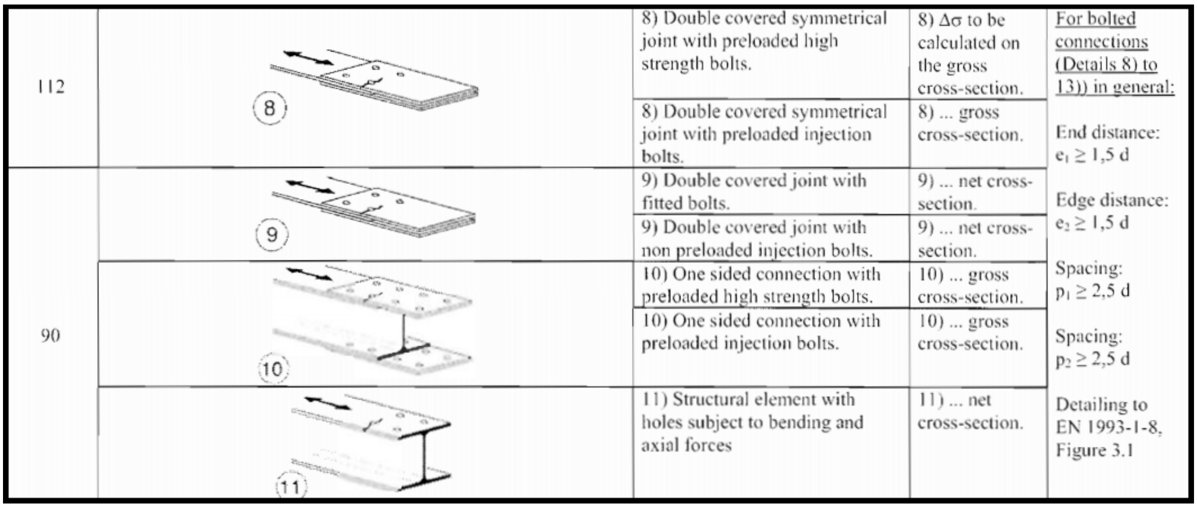

112	⑧	8) Double covered symmetrical joint with preloaded high strength bolts.	8) Δσ to be calculated on the gross cross-section.	For bolted connections (Details 8) to 13)) in general: End distance: $e_1 \geq 1{,}5\ d$ Edge distance: $e_2 \geq 1{,}5\ d$ Spacing: $p_1 \geq 2{,}5\ d$ Spacing: $p_2 \geq 2{,}5\ d$ Detailing to EN 1993-1-8, Figure 3.1
		8) Double covered symmetrical joint with preloaded injection bolts.	8) ... gross cross-section.	
90	⑨	9) Double covered joint with fitted bolts.	9) ... net cross-section.	
		9) Double covered joint with non preloaded injection bolts.	9) ... net cross-section.	
	⑩	10) One sided connection with preloaded high strength bolts.	10) ... gross cross-section.	
		10) One sided connection with preloaded injection bolts.	10) ... gross cross-section.	
	⑪	11) Structural element with holes subject to bending and axial forces	11) ... net cross-section.	

Figure 6.11: Selected detail category for the flanges [1].

Load case	Applied wind tensile load [MN]	Number of cycles including probability	Developed nominal stress [MPa]
1	0.592	4.798E+05	

Table 6.1: Data for damage calculation due to wind loading.

results from the summation of the individual fatigue ratios caused by each stress range. Both Table 6.2 and Figure 6.12 represent the results of the fatigue assessment. A decrease of approximately 59% is noticed in case where preload takes place on the connection, increasing the fatigue life of the flanges from to approximately years, more than the expected service life of the wind turbine structure.

$$N_{allowable} = \begin{cases} 10^7 \cdot \left(\frac{\Delta\sigma_{KneePoint}}{\Delta\sigma_{developed}}\right)^4 & \text{for } \Delta\sigma_{developed} \geq \Delta\sigma_{KneePoint} \\ 10^7 \cdot \left(\frac{\Delta\sigma_{KneePoint}}{\Delta\sigma_{developed}}\right)^5 & \text{for } \Delta\sigma_{developed} < \Delta\sigma_{KneePoint} \end{cases} \tag{6.10}$$

$$D_{total} = \frac{n_1}{N_1} + \frac{n_2}{N_2} + ... + \frac{n_{18}}{N_{18}} \tag{6.11}$$

The number of cycles of occurrence of each one of the 18 cases, presented on Table 6.4,are referred to the period of 25 years (service life of the wind turbine). Thus, to calculate the fatigue life of the connection, the service life is divided by the total damage:

$$\text{Fatigue Life} = \frac{\text{Service Life (25 years)}}{\text{Damage}} \tag{6.12}$$

	Allowable number of cycles without preload	Damage without preload	Allowable number of cycles with preload	Damage with preload
	Total Damage	**1.99791**		**0.81259**
	Fatigue Life [years]	**12.5**		**30.8**

Table 6.2: Allowable number of cycles and resulting damage foe both cases of wind loading for the flanges.

Figure 6.12: Damage for flanges.

For the damage calculation through the S-N curves, nominal stresses have been calculated at the top of the segment. However, from their definition, nominal stresses are calculated based on the elastic theory and they do not take into account any stress concentration effect. This means that notch stresses, which consist of the sum of the structural stress and the non-linear stress peak (stress concentration caused by the local notch, geometrical discontinuity/change of slop), have not been taken into account for the damage calculation.

Nevertheless, regarding the FE model, as it obvious from Figures 6.13 to 6.18, where the maximum principal stresses of both flanges have been plotted for the maximum wind load and for both the load cases (with & without preload), high stress concentration is noticed especially on the ”corners” around the hole of the MP flange due to high bending for both cases. This implies that cracks will initiate in these areas and may lead to an underestimation of the calculated fatigue life of the connection.

The fact that higher stresses are developed on the MP flange compare to TP flange can be also explained by the following aspects:

1. The stiffness of the MP flange is much higher than the stiffness of the TP flange (it has been proven in previous section), so most of the applied load is directly transferred to the MP.
2. The sharpness appeared around the hole of the MP flange (notches) favors the development of higher stress concentration.

In case where preload takes place on the connection, the stress range/difference between the two load steps is used for the damage and the fatigue life calculation of the connection, but through the ANSYS Workbench Software it is not able to have this stress contour plot.

Figure 6.13: Maximum principal stress developed on MP flange for the maximum wind damage load in case without preload.

Figure 6.14: Maximum principal stress developed on MP flange at the end of the preloading step (30 MPa applied pressure).

Figure 6.15: Maximum principal stress developed on MP flange for the maximum wind damage load in case with preload.

Figure 6.16: Maximum principal stress developed on TP flange for the maximum wind damage load in case without preload.

Figure 6.17: Maximum principal stress developed on TP flange at the end of the preloading step (30 MPa applied pressure).

Figure 6.18: Maximum principal stress developed on TP flange for the maximum wind damage load in case with preload.

At this point it should be noticed that for the above damage calculation and the fatigue life estimation only the wind damage loads have been considered for the fatigue assessment, as the damage ratio due to wave loading is much lower than 1. This can be verified in the Figure 6.19 as well, where the developed stress ranges and the number of cycles of occurrence have been plotted and compared with the selected S-N curves, and Table 6.3, where both the number of allowable cycles for each stress range and the fatigue damage have been calculated for both the load cases.

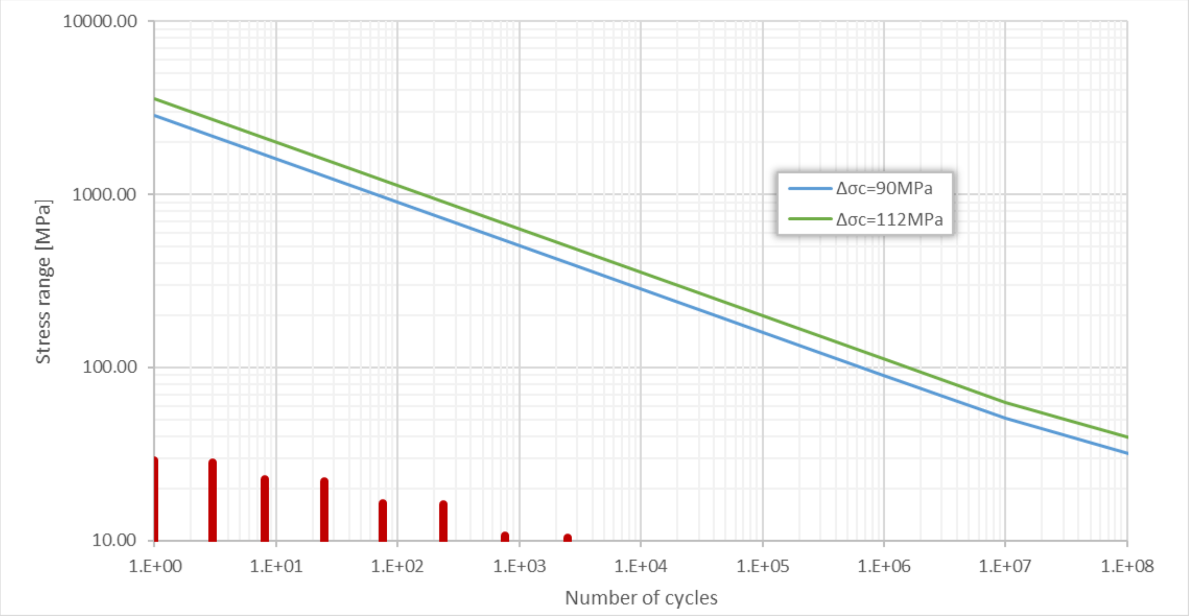

Figure 6.19: S-N curves used for the flanges (wave damage load).

	Allowable number of cycles without preload	Damage without preload	Allowable number of cycles with preload	Damage with preload
	Total Damage	**3.54E-07**		**1.19E-07**

Table 6.3: Allowable number of cycles and resulting damage foe both cases of wave loading for the flanges.

6.5.2. Fatigue assessment of the dowel

The next component that is tested for the fatigue life assessment of the wedge connection is the dowel/wedge. In this case the detail category $\Delta\sigma_c = 100MPa$ from Eurocode 3 Part 1-9 (see also Figures 6.21 and 6.22), which is suitable for bolts in single or double shear, has been selected. This detail category is only used for the case without preload.

In case where preload takes place, the variation of the dowel force is rather small, so dowel will not be critical in this case. More specifically, the vertical reaction force, which act as preload, when pressure is applied for the final installation of the dowels is approximately equal to higher than the maximum value of the damage equivalent load acting on the connection segment. This can be also verified from the graph in Figure 6.20, where the developed stresses on dowel have been plotted for both the cases with and without preload until the ULS load . Here these stresses have been exported through ANSYS at the point where maximum stresses are developed (at the middle of the bottom side of dowel). Same as in case of bolted connections a ”plateau” appears on the developed stresses on dowel until the level where the applied load in lower than the preload.

Figure 6.20: Stress development on dowel in case of preload until the ULS load.

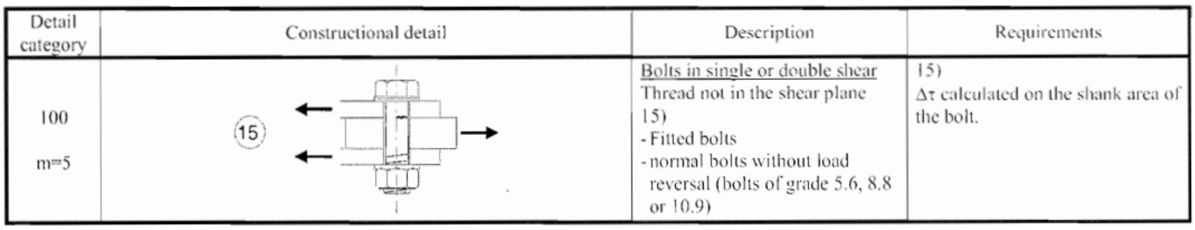

Detail category	Constructional detail	Description	Requirements
100 m=5	⑮	Bolts in single or double shear Thread not in the shear plane 15) - Fitted bolts - normal bolts without load reversal (bolts of grade 5.6, 8.8 or 10.9)	15) Δτ calculated on the shank area of the bolt.

Figure 6.21: Selected detail category for dowels [1].

Figure 6.22: S-N curve used for dowels.

Same as in case of the two flanges that has been presented in the previous section, the developed stresses on dowels and the allowable number of cycles are calculated for each one of the 18 load cases, based on the selected detail category. The final results regarding the damage and the fatigue life of the non preloading dowels are presented on Table 6.4 and Figure **??**.

	Stress developed on dowel [MPa]	Allowable number of cycles without preload	Damage without preload

Table 6.4: Data for damage calculation due to wind loading.

The fact that the variation of the dowel force has been assumed to be small in case of preloading and as a result does not cause any damage on it or on the wedge connection in general, can be also verified in Figures 6.23 to 6.25 exported from Ansys Workbench, where the maximum principal stresses developed on the dowel have been plotted for both cases (with and without preload), at the end of each load step, for the maximum wind damage load.

Figure 6.23: Maximum principal stress developed on dowel for the maximum wind damage load in case without preload.

Figure 6.24: Maximum principal stress developed on dowel at the end of the preloading step (30 MPa applied pressure).

Figure 6.25: Maximum principal stress developed on dowel for the maximum wind damage load in case with preload.

Having a look at the figures exported from FE software, it is clear that the critical area of the dowels (in case without preload), from where cracks will probably initiate, is approximately at the center of the bottom side of it. This is due to the fact that when the axial tensile load is applied on the top of the shell, the bottom side of the dowel is also in tension, and the highest bending moment occurs in the middle of the dowel’s length. This is also obvious in Figure 6.26, where several points have been selected along the length of the bottom side of the dowel and maximum principal stresses derived by the FEA have been plotted.

Figure 6.26: Maximum principal stress development at the bottom side of dowel.

6.5.3. Fatigue assessment of bushings

The last components of the connection that have not been studied yet for the fatigue damage are the bushings, which are located at the inner part of the TP' s main holes, where the dowel is inserted. Generally, bushings are used to allow constrained relative motions between two or more parts. In this case, as it has already been referred in the previous chapter, bushings are made by FRP material.

Composite materials are different from metals, as they indicate a distinct behavior under fatigue loading. The fatigue damage and failure mechanisms are more intricate in composite materials than in metals in which a crack initiates and propagates up to fracture. In composite materials, several micro-cracks initiate at the primary stage of the fatigue growth, resulting in the initiation of various types of fatigue damage and this is dependent on the characteristics of the FRP material that has been used (fiber volume fraction) [6]. Thus, in other words, damage mechanism in an FRP material is a complex process to describe and various tests should be carried out in order to develop fatigue curves (S-N curves).

However, for the purpose of this thesis, in order to have an approximate view of how these bushings may influence the fatigue life of the connection, based on a method suggested on [19], an S-N curve is considered by assuming R=-1 (stress ratio) and angle 90° (angle between the fiber direction and the applied load). Thus, once the maximum principal stresses are exported for both of the bushings, the allowable number of cycles is calculated by making use of the following expression:

$$\sigma_\alpha = \sigma_0 \cdot N^{-\frac{1}{k}} \tag{6.13}$$

The coefficients σ_0 and $\frac{1}{k}$ are given below, while σ_α refers to the developed stresses.

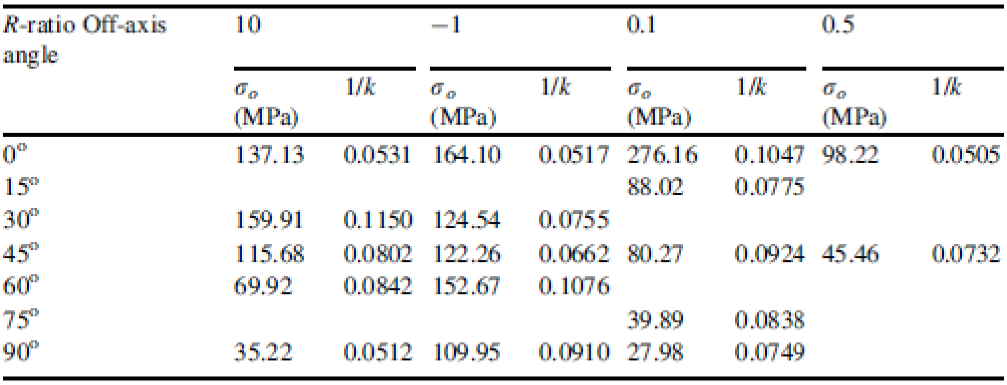

R-ratio Off-axis angle	10		−1		0.1		0.5	
	σ_o (MPa)	1/*k*	σ_o (MPa)	1/*k*	σ_o (MPa)	1/*k*	σ_o (MPa)	1/*k*
0°	137.13	0.0531	164.10	0.0517	276.16	0.1047	98.22	0.0505
15°					88.02	0.0775		
30°	159.91	0.1150	124.54	0.0755				
45°	115.68	0.0802	122.26	0.0662	80.27	0.0924	45.46	0.0732
60°	69.92	0.0842	152.67	0.1076				
75°					39.89	0.0838		
90°	35.22	0.0512	109.95	0.0910	27.98	0.0749		

Figure 6.27: Estimated model parameters [19].

Based on data provided by the above figure, the S-N curve that is used is plotted and presented in Figure 6.28. In the same figure, the stress developed in each load case when no preload takes place versus the number of cycles of occurrence have been plotted as well. As it is obvious, for all the wind damage load cases, the number of cycles of occurrence is much higher than the allowable ones based on this S-N curve, which means that bushings are not able to withstand the damage loads acting on the wind turbine structure, leading to failure of the connection.

Regarding now the case with preload, assuming the same S-N curve, the damage has been totally eliminated. However, due to the fact that bushings are always loaded in compression,

Figure 6.28: S-N curve used for the bushings in case without preload.

the assumption that the stress ratio is equal to R=-1 may not give representative results. For this reason, damage has been also calculated assuming stress ratio R=0.1 for the same angle (90°). Results for both curves in case with preload are presented in the Table 6.5.

Figure 6.29: S-N curve used for the bushings in case with preload.

	R=-1		**R=0.1**	
	Allowable number of cycles	**Damage**	**Allowable number of cycles**	**Damage**

Table 6.5: Allowable number of cycles and resulting damage foe both cases of wind loading for the flanges.

As it was expected, the damage based on characteristics of stress ratio R=0.1 is much higher than the one resulted for R=-1. However, in both cases the damage ratio of bushings is within the acceptable limits (D<1), so based on this assumption for the S-N curves, they do not cause any damage and as a result they do not affect the fatigue life of the wedge connection in case where preload takes place.

In the following figures, exported from ANSYS Workbench, the minimum principal stress distribution on the bushings due to the highest wind damage load (case 18) has been plotted at the end of each load step.

Figure 6.30: Minimum principal stress distribution on bushings in case where no preload takes place.

Figure 6.31: Minimum principal stress distribution on bushings at the end of preloading step.

Figure 6.32: Minimum principal stress distribution on bushings in case where preload takes place.

.

.

7

Parametric Study

Several parameters that may influence the fatigue life of the wedge connection or affect the FEA results are presented in this chapter.

7.1. Mesh size

In finite element analysis the size of mesh is a critical parameter. More specifically, the size of mesh is closely related to the accuracy of the analysis's results and the required computing time. Thus, in order to investigate the mesh size influence on the FEA of the wedge connection, the maximum principal stresses derived for both cases of loading (with and without preload) and as a result the final damage have been calculated for both coarse and fine mesh.

Generally, the use of a bad design mesh in a problem where stress concentration is present could imply an over or under prediction of the maximum stress within a structure, which results in an over cost in the design or a failure in service of the designed structure. Actually, according to FEA theory, the FE models with fine mesh yields highly accurate results but may take longer computing time. On the other hand, those FE models with coarse mesh may lead to less accurate results but less computing time.

Figure 7.1: Total damage of each component for coarse and fine mesh.

For the current analyses, the size of coarse mesh has been selected to be equal to 30mm, while the size of the fine mesh has been reduced to half, 15mm. In the Figures 7.1 and 7.2, the influence of mesh size on each component of the wedge connection is illustrated. As it is obvious, the difference is of great importance especially for the components which suffer from high stress concentration at specific areas.

At this point it should be noticed that in our case, the mesh size does not cause any influence on the nominal stresses used for the damage calculation, but through the finer mesh we have a better view for the critical areas of the wedge connection geometry from which cracks may initiate during the service life of the structure and may lead to its premature failure (failure before the estimated fatigue life).

In the following figures, the maximum principal stress contour plot for each component of the wedge connection for both coarse and fine mesh is illustrated.
Due to limitations in ANSYS software regarding the number of mesh nodes and elements, the refinement has been limited in specific areas, where high stress concentration has been noticed.

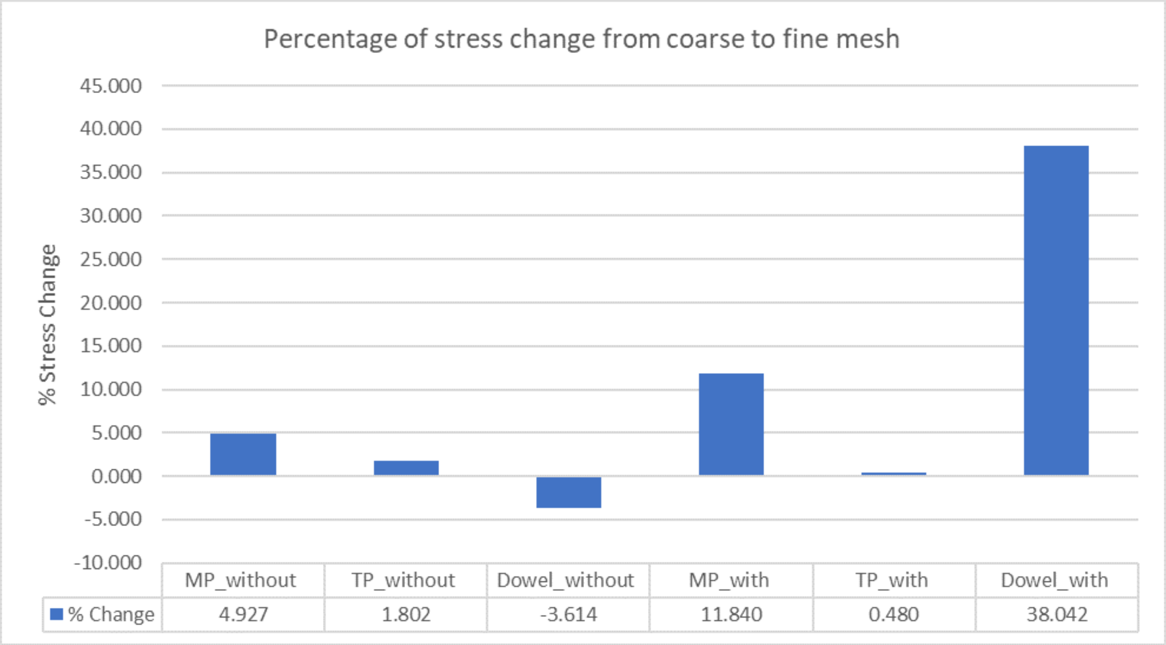

Figure 7.2: Percentage of damage change for each component for coarse and fine mesh.

Figure 7.3: Maximum principal stresses for MP flange for coarse (left) and fine (right) mesh.

Figure 7.4: Maximum principal stresses for TP flange for coarse (left) and fine (right) mesh.

Figure 7.5: Maximum principal stresses for dowel for coarse (left) and fine (right) mesh.

7.2. Friction coefficient

Generally, friction coefficient between different surfaces in all types of connections plays an important role in their performance, since it is one of the most contributing factor in transferring the applied external loads on the different parts of the connection. More specifically, the friction coefficient as a factor determines the proportion of the applied external force to be conveyed through two surfaces and from this factor the developed clamping force depends on.

In this section two cases have been examined:

- friction coefficient between MP flange and wedges,
- friction coefficient of bushings.

The friction coefficient between MP and TP flanges has not been tested, as it does not have any influence to the developed preload.

7.2.1. Friction coefficient between MP flange and wedges

In this subsection, the influence of the friction coefficient between MP flange and dowels is tested. The results of the maximum principal stresses, presented in the previous chapter, have been exported for friction coefficient $\mu = 0.10$ between these components. Here, the stresses have been exported for all components of the wedge connection (except bushings) by both decreasing and increasing the value of the friction coefficient to $\mu = 0.05$ and $\mu = 0.15$ respectively. The resulted percentage change of stresses for both of cases, presented in Figure

7.7, is compared to the stresses developed when $\mu = 0.10$ is used and for coarse mesh in order to reduce the required computing time.

Figure 7.6: Maximum principal stress of each component for different values of friction coefficient between MP flange and dowel.

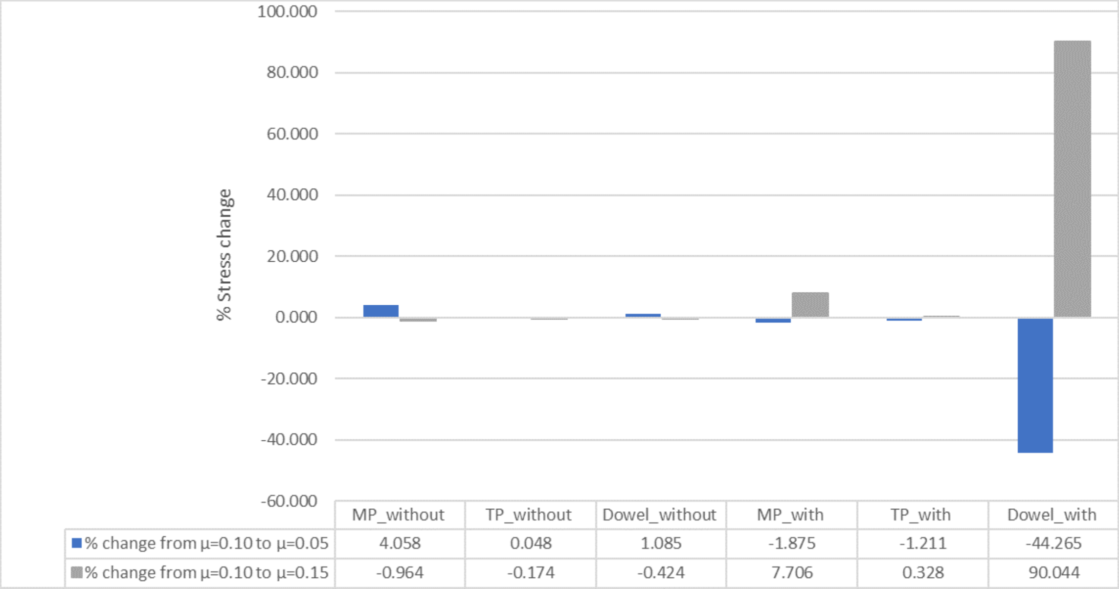

Figure 7.7: Percentage of stress change for each component for different values of friction coefficient between MP flange and dowel.

Having a first look on Figures 7.6 and 7.7, one can easily see that the reduction of the friction coefficient between MP flange and dowel has generally no significant influence on the maximum stresses developed on the connection in case without preload. However, in case where the preload appears, the increase of friction coefficient leads to an increase in the developed stress difference as well. To have a better understanding why this happens, the effect of friction coefficient change on the contact pressure developed between the MP and TP flanges (preload) is illustrated in Figure 7.8. Thus, as it was expected from the FBD, the increase of friction coefficient between dowels and MP flange leads to decrease of preload between the two flanges, as these values are inversely proportional. Decrease of preload means decrease of the stresses developed on the wedge connection at the end of the first load step, and as a result increase of the stress differences between the two load steps.

Figure 7.8: Contact pressure between MP and TP flanges for different values of friction coefficient between MP flange and dowels.

Dowel: FBD

In the figure below, the reaction forces developed on the dowel during the final installation step are presented. The vertical reaction force between the MP flange and the dowel (inclined plane) is the one that act as the preload.

$$\Sigma F_x = 0 \implies F_{external} = F_{TP} + F_{MP} \cdot cosa \tag{7.1}$$

but,

$$F_{TP} = \mu_{TP} \cdot N \tag{7.2}$$

$$F_{MP} = \mu_{MP} \cdot N \cdot cosa \tag{7.3}$$

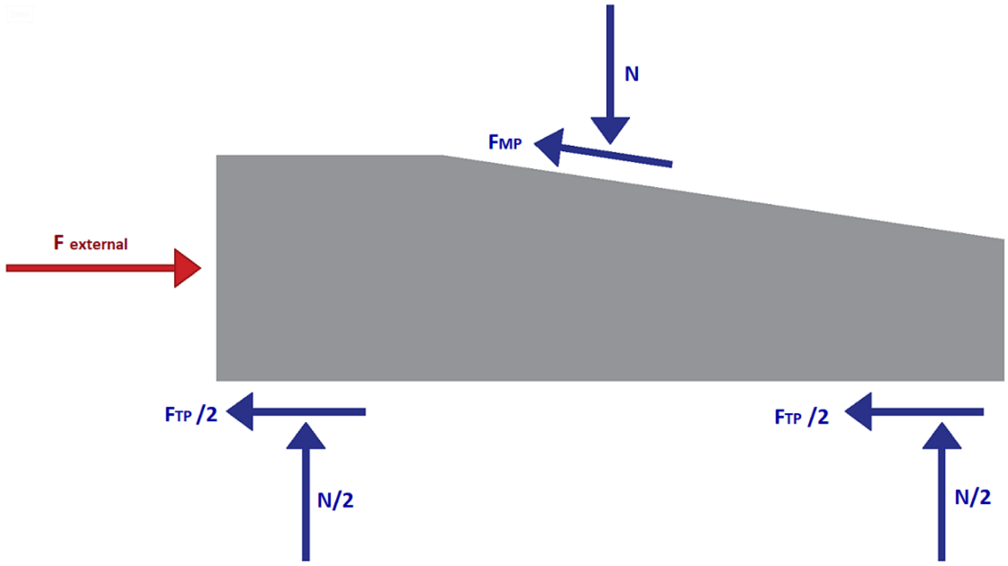

Figure 7.9: Dowel: Free body diagram.

$$\Rightarrow \ F_{external} = \mu_{TP} \cdot N + \mu_{MP} \cdot N \cdot cos^2 a = N \cdot \left(\mu_{TP} + \mu_{MP} \cdot cos^2 a\right) \ \Rightarrow \ N = \frac{F_{external}}{\mu_{TP} + \mu_{MP} \cdot cos^2 a} \tag{7.4}$$

7.2.2. Friction coefficient of bushings

The influence of friction coefficient of bushings is tested in this subsection. Maximum principal stresses have been exported again for each component by increasing their friction coefficient from $\mu = 0.05$ to $\mu = 0.1$. Same as before, coarse mesh has been used for the analysis.

In Figures 7.10 & 7.11, the maximum stresses and the percentage of stress change for each individual part of the connection are presented respectively.

Figure 7.10: Maximum principal stresses developed on each component for different values of friction coefficient of bushings.

Generally, the increase of friction coefficient of bushings does not lead to any important ”changes” in the stresses developed on the wedge connection’s components, except in case of dowels when preload takes place, where a significant increase on the stress range (stress difference between the 2 load steps) occurs. However, even in this case, the stress range still remain in low levels and it is not critical for the fatigue life of the connection. This increase on the stress range can be explained by plotting the influence of the bushings’ friction coefficient change on the developed contact pressure between MP an TP flanges (Figure). Same as in the previous case, these two these values are inversely proportional, so increase of friction coefficient of bushings leads to decrease of preload and as a result increase of the stress difference.(In expression 7.4, the friction coefficient μ_{TP} refers to friction coefficient between bushings and dowel, as there is no direct contact between TP flange and dowel.)

7.3. Stiffness of bushings

The last parameter that is tested and may affect the stress development in critical areas and as a result the damage ratio and the fatigue life of the whole connection is the E modulus of elasticity of bushings (stiffness), made by FRP material. For the maximum principal stresses that have been exported through FEA until now, the E modulus of bushings have been considered equal to 2.8 GPa. Thus, in order to understand their influence in the total life of each

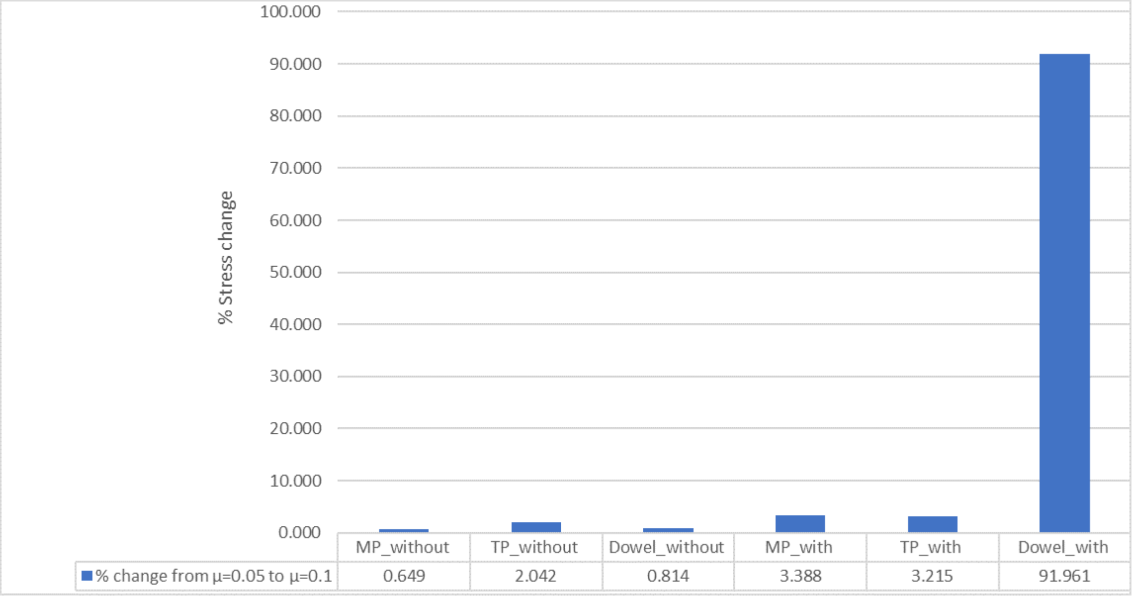

Figure 7.11: Percentage of stress change for each component for different values of friction coefficient of bushings.

Figure 7.12: Contact pressure between MP and TP flanges for different values of friction coefficient of bushings.

component, FEA of the connection has been performed by changing the bushings' material and increase their stiffness to 100 GPa. For better accuracy, the results presented in the following figures have been exported by performing the FEAs with fine mesh.

Figure 7.13: Maximum principal stresses developed on each component for increasing bushings' stiffness.

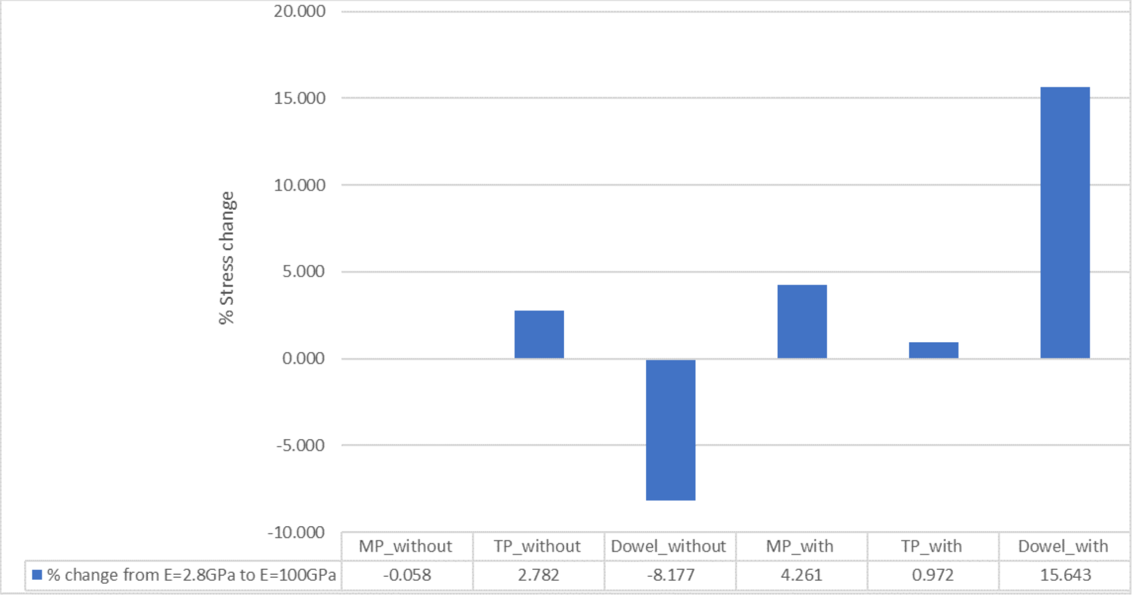

Figure 7.14: Percentage of stress change of each component for increasing bushings' stiffness.

According to Figures 7.13 and 7.14, the increase of bushings' stiffness does not cause any significant change on the maximum principal stresses developed on the individual components of the wedge connection. The highest difference is appeared in case of dowels, and more specifically when preload is developed; in this case a decrease of approximately 15.6% is noticed. However, even in this case the stress levels remain relatively low, so they do not have any negative impact in the fatigue life of the connection.

.

8

Conclusions & Recommendations

8.1. Conclusions

For the current selected location of the wedge connection, +4m above the MSL, it has been concluded that the driving loads for the fatigue life assessment of the connection are those resulted exclusively due to wind loads acting on the wind turbine structure. This is happened because the high-frequency wave loads (more cycles and higher probability of occurrence) do not cause any considerable damage on the wind turbine structure at that level, as their amplitude is lower than the height of the wedge connection's location (<4m).

Regarding now the damage calculation of the connection, the selection of the S-N curves that have been used was based on assumptions related to the only one test specimen. So based on this single point and assuming the same slope as the existing S-N curves, the ones related to the double plate shear bolted connections have been considered for the damage estimation, as they are very close and also below to the hypothetical resulted curve. Thus, according to these selected curves, it results that the wedge connection is not able to withstand the damage loads acting on the wind turbine structure in case where no preload is developed. More specifically, in case where no preload takes place, and considering that the performance of the bushings has not been taken into account, the most critical part of the connection in terms of fatigue is the dowel. However, in case of preload, the damage of the wedge connection has been completely eliminated, as the damage ratio in all parts of the wedge connection is lower than the acceptable limit, 1 (even in case where bushings are considered). So, in case of preloading, the fatigue life of the wedge connection has been increased for approximately 80% and is higher than the expected service life of the wind turbine structure.

In Table 8.1 and Figure 8.1, the final damage results for both the dowels and the flanges are presented.

	Wind Load		**Wave load**	
	Without Preload Damage [-]	**With Preload Damage** [-]	**Without Preload Damage** [-]	**With Preload Damage** [-]

Table 8.1: Damage of the wedge connection.

The estimated damage ratios that have been resulted for the fatigue assessment of the wedge connection, are based on the developed nominal stresses which do not take into account the areas with high stress concentration. As a result, this may lead to uncertainties regarding

Figure 8.1: Total Damage of the wedge connection (wind loading).

the estimated fatigue life of the connection. So, considering also the stress concentration effects, the areas from where the cracks may initiate can be estimated through the FEA. More specifically, regarding now the MP flange, despite the fact that the damage ratio is relatively low, due to its greater stiffness (absorbs most of the external load), it is the component where the highest stress concentration is noticed and this may lead to an unexpected failure of the connection. The fact that cracks appeared on these areas of MP flange has been verified by the last fatigue tests of the differentiated geometry of the connection. However, in order to reduce or eliminate the ”damage” at these areas and increase the fatigue life of the connection, the geometry around the hole of the MP should be redesigned by making it as smoother as possible (e.g. round hole).

8.2. Recommendations

For the purpose of this thesis, as it has already been referred, the location of the wedge connection has been chosen at 4 meters above the MSL. It would be noteworthy to check the damage and the fatigue life of the wedge connection at different levels, and especially below the MSL where the contribution of the wave loading is of great importance. Furthermore, regarding the loads, due to lack of information, the assumption that both the wind and waves come from the same direction has been made. Despite the fact that this assumption is conservative, as it leads to an overestimation of the acting loads on the turbine structure (and as a result in an over-design), in reality this never happens. Thus, it would be noteworthy to search for more information regarding the environmental data to increase the accuracy of the loads acting on the wind turbine structure.

Also, for an appropriate fatigue assessment, at least 15 specimens of the wedge connection should be tested in order to establish a new S-N curve for this type of connection. More specifically, according to DNV-GL-RP-C203 [10], at least three different stress ranges should be selected in the relevant S-N curve such that a representative slope of the S-N curve can be determined.

Regarding again the experiments that have been done until now, it should be noticed that they are based on a single segment of the wedge connection, which is not curved, as happened with the real one, and does not provide/simulate the whole stiffness of the ring. Thus, performing experiments on a complete ring of dowels will help to have a better view of the global behavior of the connection under several types of loading.

Last, for the current analysis, it has been assumed that there is a full contact between the MP and TP flanges, so there is actually no ”loss” of the preloading force as the vertical reaction derived due to applied pressure on the dowel is directly transferred between these two contact surfaces. However, in reality, fabrication imperfections may be presented on the contact areas between the flanges (not absolute flat geometry which creates gaps between them, like possible discontinuities related to manufacturing processes) and this may arise critical issues in terms of fatigue performance of the connection. More specifically, when gaps are presented, the preload force causes meridional stresses in the tower wall, because part of the developed preload is transferred into the tower and not into contact forces in between the flanges. This leads to either reduced or no compressive contact stresses in between the flanges in the middle of the gap and increased contact stresses at the end of the gap [33]. So, the fatigue damage ratio for the dowels in the middle of the gap is much increased (lower stresses developed during the first load step -> increase of stress range/difference between the two load steps -> higher damage ratio -> decrease of fatigue life).

A

Finite Differences Scheme

The beam is a structural element that is loaded mainly laterally with respect to its axis. Consequently, the substructure of an offshore wind turbine can be modeled as a beam.

As it is previously discussed, the beam is discretized with the help of the finite differences scheme. If the the beam is discretized in N nodes (so N-1 elements) and it has length L, the length of each element is l=L/(N-1).

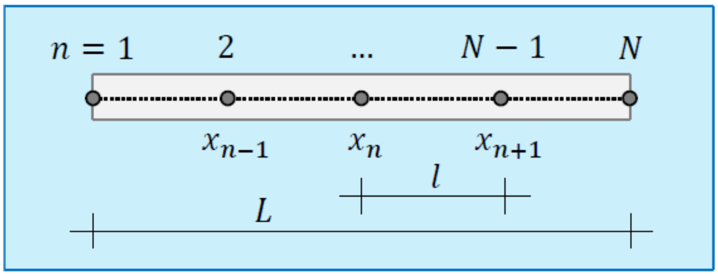

Figure A.1: Discretization of a beam [18]

The equation of the beam is given by the following expression:

$$EI \cdot w''''(x,t) + \rho \cdot A \cdot \ddot{w}(x,t) = 0 \tag{A.1}$$

With the use of the finite differences scheme the term w””(x_n) will be replaced by the displacements of the points around the specific point. Analytically the Taylor Series Expansion (TSE) will be evaluated at x_n and 2 points at the left side and 2 points on the right, because the order of this term is 4. The distance between the points is:

$$(x_{n+2} - x_n) = 2 \cdot l, (x_{n+1} - x_n) = l, (x_{n-1} - x_n) = -l, (x_{n-2} - x_n) = -2 \cdot l \tag{A.2}$$

The TSE for the five points are the following:

$$w(x_{n+2}) = w(x_n) + 2 \cdot l \cdot w'(x_n) + 4 \cdot \frac{l^2}{2} \cdot w''(x_n) + 8 \cdot \frac{l^3}{6} \cdot w'''(x_n) + 16 \cdot \frac{l^4}{24} \cdot w''''(x_n) \tag{A.3}$$

$$w(x_{n+1}) = w(x_n) + l \cdot w'(x_n) + \frac{l^2}{2} \cdot w''(x_n) + \frac{l^3}{6} \cdot w'''(x_n) + \frac{l^4}{24} \cdot w''''(x_n) \tag{A.4}$$

$$w(x_n) = w(x_n) \tag{A.5}$$

$$w(x_{n-1}) = w(x_n) - l \cdot w'(x_n) + \frac{l^2}{2} \cdot w''(x_n) - \frac{l^3}{6} \cdot w'''(x_n) + \frac{l^4}{24} \cdot w''''(x_n) \tag{A.6}$$

$$w(x_{n-2}) = w(x_n) - 2 \cdot l \cdot w'(x_n) + 4 \cdot \frac{l^2}{2} \cdot w''(x_n) - 8 \cdot \frac{l^3}{6} \cdot w'''(x_n) + 16 \cdot \frac{l^4}{24} \cdot w''''(x_n) \tag{A.7}$$

The next step is to find a way to sum these 5 evaluations in such a way that only the w””(x_n) remains:

$$\alpha \cdot w(x_{n-2}) + \beta \cdot w(x_{n-1}) + \gamma \cdot w(x_n) + \delta \cdot w(x_{n+1}) + \epsilon \cdot w(x_{n+2}) = w''''(x_n) + error \tag{A.8}$$

For the above expression there are five equations and five unknown coefficients, so solving the following system, the five unknowns can be easily determined.

$$\begin{bmatrix} 1 & 1 & 1 & 1 & 1 \\ 2l & l & 0 & -l & -2l \\ 2l^2 & \frac{l^2}{2} & 0 & \frac{l^2}{2} & 2l^2 \\ \frac{8l^3}{6} & \frac{l^3}{6} & 0 & -\frac{l^3}{6} & -\frac{8l^3}{6} \\ \frac{16l^4}{24} & \frac{l^4}{24} & 0 & \frac{l^4}{24} & \frac{16l^4}{24} \end{bmatrix} \cdot \begin{bmatrix} \alpha \\ \beta \\ \gamma \\ \delta \\ \epsilon \end{bmatrix} = \begin{bmatrix} 0 \\ 0 \\ 0 \\ 0 \\ 0 \end{bmatrix} \tag{A.9}$$

Since the five coefficients are now known, the term w””(x_n) can be calculated by the formula below:

$$w''''(x_n) = \frac{w(x_{n-2}) - 4 \cdot w(x_{n-1}) + 6 \cdot w(x_n) - 4 \cdot w(x_{n+1}) + w(x_{n+2})}{l^4} \tag{A.10}$$

For the evaluation of the TSE there is need for to points on the left of the forepart of the beam as well as two points on the right end of the beam. The boundary conditions should be applied. We have made the assumption that both the bottom and the top ends are free. Thus, assuming that we have a beam with 7 nodes:

$$w_1'' = 0 \rightarrow \frac{w_2 - 2w_1 + w_0}{l^2} = 0 \rightarrow w_0 = 2w_1 - w_2 \tag{A.11}$$

$$w_1''' = 0 \rightarrow \frac{-w_3 + 2w_2 - 2w_0 + w_{-1}}{2l^3} \rightarrow w_{-1} = 4w_1 - 4w_2 + w_3 \tag{A.12}$$

$$w_7'' = 0 \rightarrow 2w_8 = w_7 - w_6 \tag{A.13}$$

$$w_7''' = 0 \rightarrow w_9 = 4w_7 - 4w_6 + w_5 \tag{A.14}$$

Applying the above boundary conditions the final equation of motion for a beam with 7 nodes and two free ends is reached.

$$\rho \cdot A \cdot \begin{bmatrix} 1 & 0 & 0 & 0 & 0 & 0 & 0 \\ 0 & 1 & 0 & 0 & 0 & 0 & 0 \\ 0 & 0 & 1 & 0 & 0 & 0 & 0 \\ 0 & 0 & 0 & 1 & 0 & 0 & 0 \\ 0 & 0 & 0 & 0 & 1 & 0 & 0 \\ 0 & 0 & 0 & 0 & 0 & 1 & 0 \\ 0 & 0 & 0 & 0 & 0 & 0 & 1 \end{bmatrix} \cdot \begin{bmatrix} \ddot{w}_1 \\ \ddot{w}_2 \\ \ddot{w}_3 \\ \ddot{w}_4 \\ \ddot{w}_5 \\ \ddot{w}_6 \\ \ddot{w}_7 \end{bmatrix} + \frac{EI}{l^4} \cdot \begin{bmatrix} 2 & -4 & 2 & 0 & 0 & 0 & 0 \\ -2 & 5 & -4 & 1 & 0 & 0 & 0 \\ 1 & -4 & 6 & -4 & 1 & 0 & 0 \\ 0 & 1 & -4 & 6 & -4 & 1 & 0 \\ 0 & 0 & 1 & -4 & 6 & -4 & 1 \\ 0 & 0 & 0 & 1 & -4 & 5 & -2 \\ 0 & 0 & 0 & 0 & 2 & -4 & 2 \end{bmatrix} \cdot \begin{bmatrix} w_1 \\ w_2 \\ w_3 \\ w_4 \\ w_5 \\ w_6 \\ w_7 \end{bmatrix} = \begin{bmatrix} 0 \\ 0 \\ 0 \\ 0 \\ 0 \\ 0 \\ 0 \end{bmatrix} \tag{A.15}$$

In expression A.15, the first matrix corresponds to the mass matrix and the second one to the stiffness matrix.

Regarding the stiffness matrix, in these expressions the stiffness of the soil has not been added. It is separately calculated as it is described in Chapter 3 and finally by summing up the two matrices, the final stiffness matrix is derived.

For the real model and the calculation of mass matrix, one concentrated mass has been added on the top of the beam which represents the mass of the rotor-nacelle and another one has been added at the level of our interest, where the wedge connection is located. Actually the second mass is really small, does not affect the response of the system and it can be neglecting for the modal analysis.

Having the final Mass and Stiffness matrices, the natural frequencies can now be calculated:

$$\omega = \sqrt{\frac{K}{M}} \tag{A.16}$$

where K and M are the stiffness and mass matrices respectively.

B

Wind Time Series Generation and Thrust Force

A realistic method to generate wind time series is to use complex numbers for the Fourier coefficients, to express time series in real numbers [7]. For this matter N/2 coefficients a_n and N/2 coefficients b_n are generated to compose the Fourier coefficients vector c_n of length N as:

$$(c_n)_{0\ldots N-1} = [\frac{TU}{2\cdot\pi}; a_1 + i\cdot b_1; \ldots; a_{N/2-1} + i\cdot b_{N/2-1}; a_{N/2} + 0; a_{N/2-1} - i\cdot b_{N/2-1}; \ldots; a_1 - i\cdot b_1] \quad \text{(B.1)}$$

The generation of the random numbers a_n and b_n is such that the standard deviation is distributed equally among the real and the imaginary part (no systematic lag):

$$\sigma_{a_n}^2 = \sigma_{b_n}^2 = \frac{1}{2}\sigma_{X_n}^2 \quad \text{(B.2)}$$

C

Force Applied on Dowel due to Hydraulic Pressure

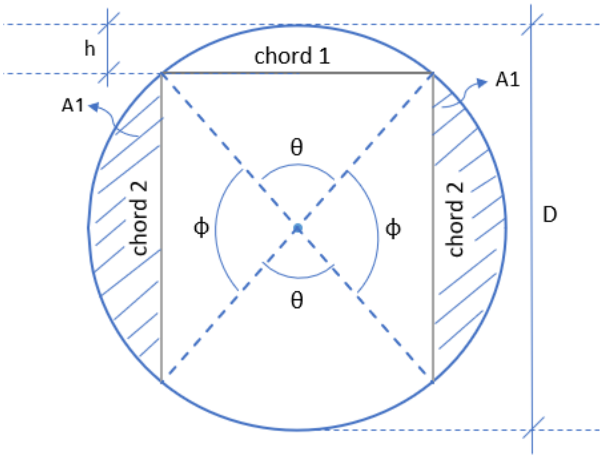

Figure C.1: Geometry of the dowel.

To convert the pressure applied on the back side of the dowel to equivalent axial force, the area of the cross section of the dowel should be first calculated.

It is given that:

$$chord_1 = 112mm \tag{C.1}$$

but, from the geometry of the dowel the length of this chord is given by the following expression:

$$chord_1 = Dsin\frac{\theta}{2} \tag{C.2}$$

Thus for D=140mm, through equations C.1 and C.2, the angle θ results:

$$\theta = 2 \cdot arcsin\frac{112}{140} = 106.260° \tag{C.3}$$

The angle ϕ and as a result the length of the $chord_2$ can be now calculated in the same way:

$$\phi = \frac{1}{2}(360° - 2 \cdot \theta) = 73.740° \tag{C.4}$$

and

$$chord_2 = D sin\frac{\phi}{2} = 84mm \tag{C.5}$$

$$h = \frac{1}{2}(D - chord_2) = 28mm \tag{C.6}$$

The area A_1 is derived by:

$$A_1 = \pi\left(\frac{D}{2}\right)^2 \frac{\phi}{360} - \frac{(D/2)^2}{2} sin\phi = 801.162mm^2 \tag{C.7}$$

Thus, the cross section area of the back side of the dowel is equal to:

$$A_{dowel} = \pi\frac{D^2}{4} - 2A_1 = 13791.480mm^2 \tag{C.8}$$

To convert the applied pressure on the dowel to force, the calculated area of the dowel is multiplied by the pressure. The resulting force, divided by four, is also applied as reaction force on each hole of the TP flange where the hydraulic actuators are located during the first step of installation (preloading).

D

Parametric study of preload

From the analytic FBD diagram presented in Chapter 6, the ratio between the developed vertical reaction force (preload) and the applied pressure/force on the back side of the dowel is given by the following expression:

$$\frac{F_{preload}}{F_{appliedpressure}} = \frac{1}{\mu_{bushings} + \mu_{MP} \cdot cos^2 a}$$

For the FEA, the values of the three parameters that influence the development of the preloading force are:

$\mu_{bushings}$	0.05
μ_{MP}	0.10
$angle\ a$	5°

In the next figures, the effect of each one of the three parameters on the preload has been tested by keeping constant the two of them in each case.

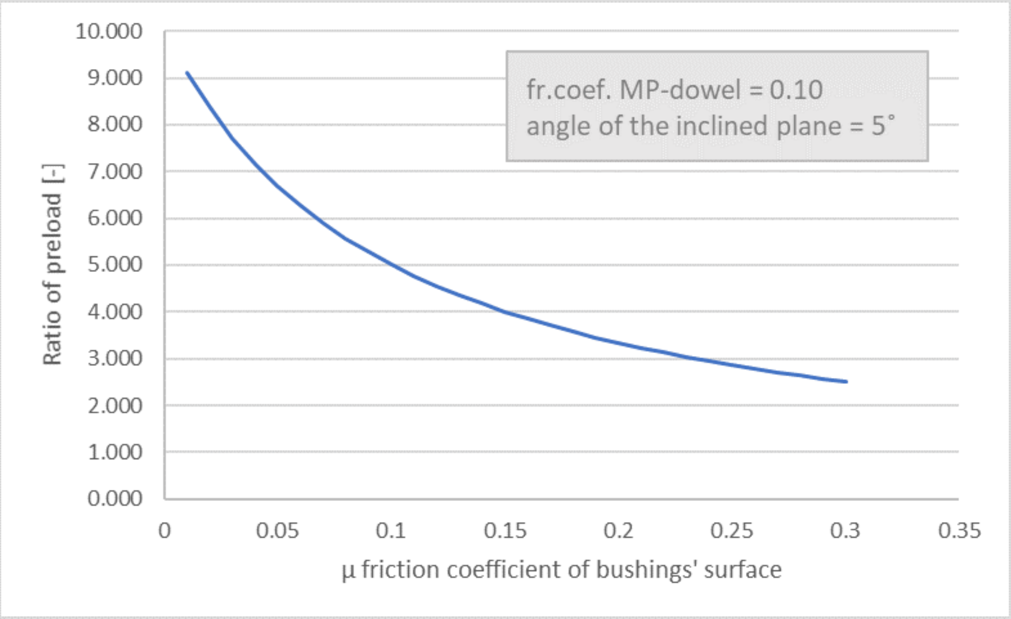

Figure D.1: Effect of friction coefficient of bushings' surface in the preloading ratio.

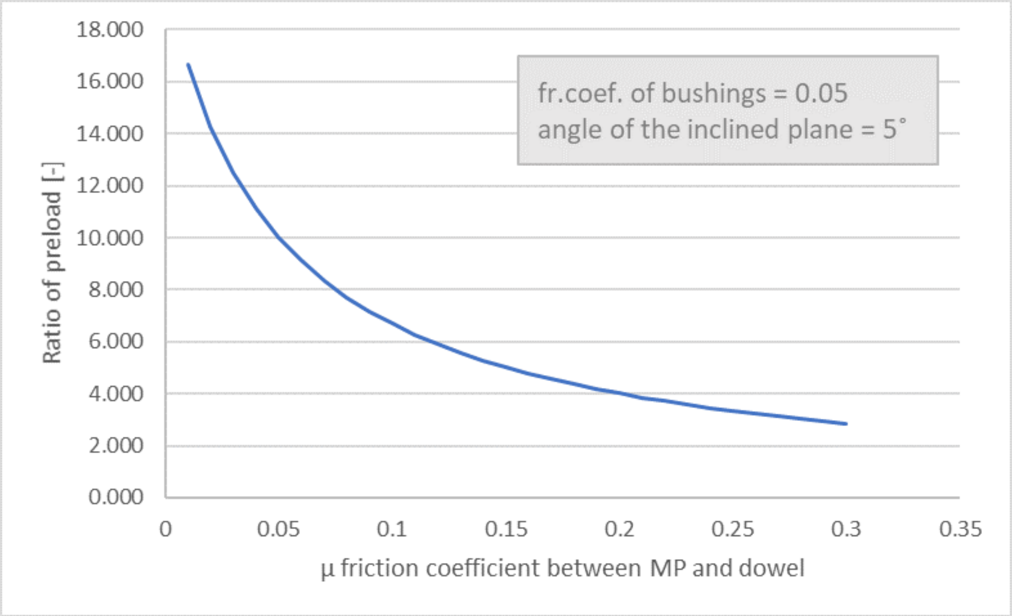

Figure D.2: Effect of friction coefficient between MP and dowel in the preloading ratio.

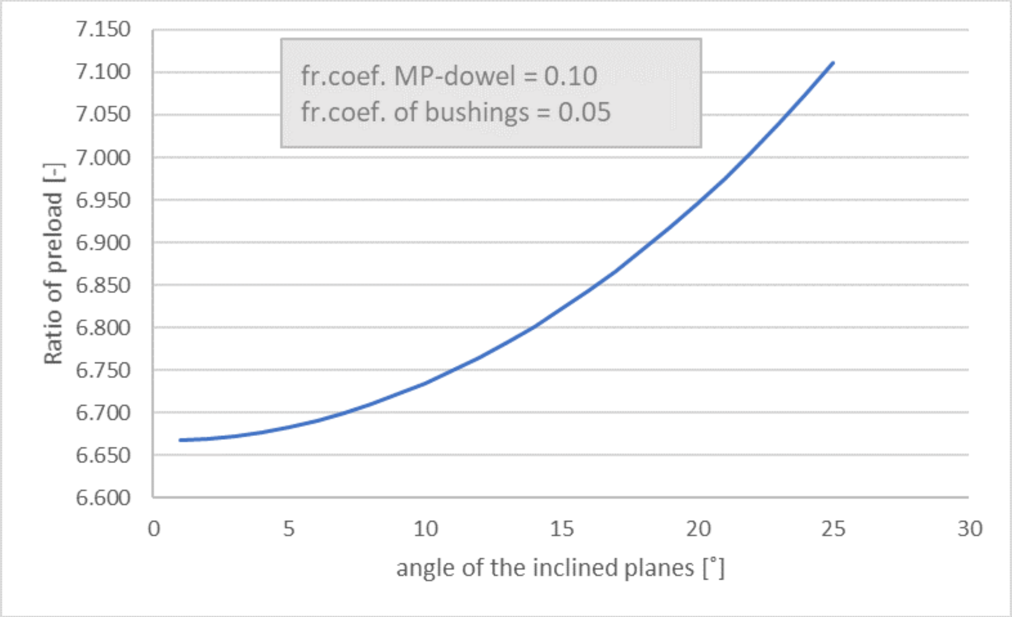

Figure D.3: Effect of the angle of the inclined planes in the preloading ratio.

.

E

Stress development in critical parts

Same as in case of dowel presented in Chapter 6, several points have been selected around the critical areas of both the MP and TP flanges and maximum principal stresses derived through the FEA have been exported for the maximum damage load for both the cases with and without preload.

Figure E.1: Maximum principal stress development around the hole of the MP flange

Figure E.2: Maximum principal stress development around the inner part of the hole of the TP flange

.

.

F

Wedge connection geometry

Figure F.1: Detail geometry

Figure F.2: Detail geometry

Bibliography

[1] Eurocode 3: Design of steel structures , part 1-9: Fatigue. *European Standards*, May 2005.

[2] Wystan Carswell, Sanjay Raja Arwade, Don J.DeGroot, Matthew A.Lackner. Soil-reliability of offshore wind turbine monopile foundation. *Wind Energy*, January 2014.

[3] Mary Carol Anderson. The hybrid monopile: Design of a novel connection for large offshore wind turbines in intermediate water depths. *TU Delft*, 2017.

[4] Ansys. Ansys mechanical structural nonlinearities: Introduction to contact. *Customer Training Material*, December 2010.

[5] Naess Arvid and Moan Torgeir. Stochastic dynamics of marine structures. *Cambridge University Press*, 2012.

[6] Md. Touhid Alam Ansary, Kalyan Kumar Singh, Mohammad Sikandar Azam. Fatigue damage analysis of fiber reinforced polymer composites. *Journal of Reinforced Plastics and Composites*. doi: 10.1177/0731684418754713.

[7] Emmanuel Branlard. Generation of time series from a spectrum: Generation of wind time series from the kaimal spectrum, generation of wave time series from the jonswap spectrum. February 2010.

[8] CRUX. Crux: Grout seals for special applications.

[9] Alain Nussbaumer, Luis Borges, Laurence Davaine. Fatigue design of steel and composite structures , 1st edition. *European Convention for Constructional Steelwork (ECCS)*, 2011.

[10] DNV-RP-C203. Fatigue design of offshore steel structures. April 2016.

[11] DNV-RP-C205. Environmental conditions and environmental loads. April 2007.

[12] Petros Dratsas. Prediction of fatigue crack growth behaviour of tubular joints used in offshore structures. *TU Delft*, March 2016.

[13] Shuqing Wang, Xiancang Song, Weichen Ding, Junfeg Du. Structural fatigue assessment of a fixed monopile platform. *Advances an Mechanical Engineering*, 2016. doi: 10.1177/1687814016679764.

[14] Dan Dubina. Advanced design of steel and composite structures: Introduction to fatigue.

[15] Laszlo Arany, Subhamoy Bhattacharya, John Macdonald, S.John Hogan. Simplified critical mudline bending moment spectra of offshore wind turbine support structures. *Wind Energy*, 2015.

[16] Gabriel Marsh, Colin Wingall, Philipp R.Thies, Nigel Barltrop, Atilla Incenik, Vengatesan Venugopal, Lars Johanning. Review and application of rainflow residue processing techniques for accurate fatigue damage estimation. *International Journal of Fatigue*, January 2016.

[17] Fabian Vorpabl, Holger Scharze, Tim Fischer, Marc Seidel, Jason Jonkman. Offshore wind turbine environment, loads, simulation and design. *WIREs Energy Environ*, September 2013. doi: 10.1002/wene.52.

[18] Antonio Jarquin Laguna, Chris Keijdener. Lectures of: Introduction to computational dynamics of offshore structures, oe44090. Academic year 2016-2017.

[19] Anastasios P.Vassilopoulos, Thomas Keller. Fatigue of fiber-reinforced composites. *Springer*, pages 31–33, January 2011. doi: 10.1007/978-1-84996-181-3.

[20] Martin Johannes Kuhn. Dynamics and design optimization of offshore wind energy conversion systems. *TU Delft*, June 2001.

[21] Inge Lotsberg, Andrzej Serednicki, Hakon Bertnes, Andreas Lervit. Design of grouted connections for monopile offshore structures- results from two joint industry projects. 2012. doi: 10.1002/stab201201598.

[22] R.C. MacCamy and R.A. Fuchs. Wave forces on piles: a diffraction theory. *Tech.Memo 69, US Army Corps of Engineers, Beach Erosion Board*.

[23] Vasileios Michalopoulos. Simplified fatigue assessment of offshore wind support structures accounting for variations in a farm. *TU Delft*, July 2015.

[24] Luuk Middelweerd. Sensitivity analysis of the first natural frequency of the offshore wind turbines in the eneco lunchterduinen wind farm. *TU Delft*, December 2017.

[25] M.Muskulus. Simplified rotor loads models and fatigue damage estimates for offshore wind turbines. *Department of Civil and Transport Engineering, Norwegian University of Science and Technology.*, 2015.

[26] Ioannis Nikiforakis. Determination of fatigue assessment of monopile-based offshore wind turbines through fidelity quantification. *TU Delft*, June 2017.

[27] OrcaFlex. Morison's equation. *www.orcina.com*.

[28] Metin Ozen. Ansys: Meshing workshop. *Ozen Engineering,INC*, November 2014.

[29] Milan Veljkovic , Marko Pavlovic. Lectures of fatigue , cie5126. *Technical University of Delft*, 2017.

[30] Kjell Inge Saevdal. Monopile foundations: Effect of scour protection on eigenfrequency of offshore wind turbines. *NTNU: Norwegian University of Science and Technology*, June 2017.

[31] Scarnet.ca. Ansys workbench user's guide.

[32] Marc Seidel. Wave induced fatigue loads, insights from frequency domain calculations. *Stahlbau 83*, 2014. doi: 10.1002/stab.2014101184.

[33] Marc Seidel. Tolerance requirements for flange connections of wind turbine support structures. *Stahlbau , 87:880887*, 2018. doi: 10.1002/stab.201810050.

[34] Peter Schaumann , Rasmus Eichstadt , Andre Staug. Advanced performance assessment methods for high strength bolts in ring flange connections. *Stahlbau 87*, 2018.

[35] Rafael Luque Sucrez. Influence of soil stiffness on the dynamic response of an offshore wind turbine. September 2015.

[36] Dimitrios Bilionis, Dimitrios Vamvatsikos. Fatigue analysis of an offshore wind turbine in mediterranean sea under a probabilistic framework. *VI International Conference on Computational Methods in Marine Engineering*, 2015.

[37] Dimitrios Bilionis, Dimitrios Vamvatsikos. Probabilistic fatigue life assessment of an offshore wind turbine. *5th ECCOmAS Thematic Conference on Computational Methods in Structural Dynamics and Earthquake Engineering*, May 2015.

[38] Joey Velarde. Design of monopile foundations to support the dtu 10mw offshore wind turbine. *TU Delft , NTNU*, June 2016.

[39] Prem Kumar Chaurasiga, Siraj Ahmed, Vilas Warudkar. Weibull distribution to determine wind power density using ground based dopples sodar instrument. *Alexandria Engineering Journal*, 2017.

[40] Domenico Lombardi, Subhamoy Bhattacharya, David Muir Wood. Dynamic soil–structure interaction of monopile supported wind turbines in cohesive soil. *ELSEVIER*, 2013.

[41] Amr Mohamed Metwally Ismaiel , Shigeo Yoshida. Study of turbulence intensity effect on the fatigue lifetime of wind turbines. *ENERGREEN*, March 2018.